AN ABSTRACT OF THE THESIS OF

Casey R. Tierney for the degree of Master of Science in Geology Presented on June 7, 2011.

Title: Timescales of Large Silicic Magma Systems: Implications from Accessory Minerals in Pleistocene Lavas of the Altiplano-Puna Volcanic Complex, Central Andes

Abstract approved:

_____

Shanaka L. de Silva

Constraining the development, evolution, and timescales of large silicic magma systems is important to understanding the development of granite batholiths, the relationships between volcanoes and their plutonic underpinnings, and the development of the continental crust.

The ignimbrite flare up that produced the Altiplano-Puna Volcanic Complex of the Central Andes is characterized by episodic volcanism over a ~11 Ma time-span that climaxed about 4 Ma. Since peak activity, the temporal and spatial record of volcanism suggests a waning of the system with only one other supervolcanic eruption at 2.6 Ma. The most recent phase of volcanism from the APVC comprises a series of late Pleistocene domes that share a general petrochemical resemblance to the ignimbrites. New U-Th/U-Pb data on zircons and high precision $^{40}Ar/^{39}Ar$ age determinations reveal that these effusive eruptions represent a temporally coherent magmatic episode.

The five largest domes (Chao, Chillahuita, Chanka, Chascon-Runtu Jarita, and Tocopuri) have a combined volume >40 km^3, and are distributed over a roughly elliptical area of almost 2000km^2 centered at 22°S 68°W. They are crystal rich (>50%) dacites to rhyolites. $^{40}Ar/^{39}Ar$ ages from biotite reveals eruption ages from 108±6 to 120±5 ka while more accurate sanidine for some of the domes reveal eruption ages from 87±4 to 97±2 ka. SIMS U-series crystallization ages from the rims of 215 zircon crystals from the domes show a similar age spectra from dome to dome, with common peaks in zircon ages at ~100ka and ~220ka. Furthermore, the ages reveal a fairly continuous spread of ages from near eruption to >300ka indicating that the residence time of this magma body was likely over a similar time interval. Ubiquitous andesitic inclusions evidence a vital role for recharge in sustaining and maybe eventual eruption of these magmas. Lastly, the interiors of crystals with rim U-Th secular equilibrium ages were re-analyzed and have yielded U-Pb ages of up to 3.5 Ma. The presence of these older interiors suggests that the source region of these magmas retained a record of an earlier history dating back to the last supervolcanic eruption in the region from the nearby Pastos Grandes caldera. This suggests that the thermal history of the system precluded complete resorption of antecrysts.

The volcanological, petrological, temporal and spatial coherence of this series of eruptions combined with the similar $^{40}Ar/^{39}Ar$ and zircon age spectra argue for a long-lived and unitary magma chamber revealing perhaps the waning of this major continental magma system.

Timescales of Large Silicic Magma Systems: Implications from Accessory Minerals in Pleistocene Lavas of the Altiplano-Puna Volcanic Complex, Central Andes

by

Casey R. Tierney

A THESIS

submitted to

Oregon State University

in partial fulfillment of
the requirements for the
degree of

Master of Science

Presented June 7, 2011

Commencement June 2011

Master of Science thesis of Casey R. Tierney presented on June 7, 2011

APPROVED:

Major Professor, representing Geology

Chair of the Department of Geosciences

Dean of the Graduate School

I understand that my thesis will become part of the permanent collection of Oregon State University libraries. My signature below authorizes release of my thesis to any reader upon request

---

Casey R. Tierney, Author

ACKNOWLEDGEMENTS

I would like to sincerely thank everyone who has assisted in making this research possible. First and foremost, I would like to express my appreciation to my advisor, Shan de Silva, for the opportunity to come to Oregon State University and participate in this exciting research. Shan's continued patience, guidance and encouragement were integral in the success of this project.

Thanks to Axel Schmitt for his guidance and humor in the field and to his seemingly countless hours of assistance and troubleshooting on the SIMS. Axel's insightful editing of various proposals, abstracts, posters and this thesis are also greatly appreciated.

To Anita Grunder, for agreeing to serve on my committee and for her enthusiastic teaching, valuable perspectives and vigorous editing of this thesis.

Completion of this research and the maintenance of my sanity would also not have been possible without my research mates, Dale Burns, Stephanie Grocke, Jason Kaiser, Bob Peckyno, Jamie Kern, Rodrigo Iriarte, Trish Gregg, Kevin Weldon and Toshio Miyazaki, who were always eager to offer help and support when needed.

My gratitude also goes to the various other VIPERS, graduate students, and acquaintances who served as great resources and excellent friends during my time in Corvallis.

Thanks to my family and friends back home in Iowa and elsewhere, especially my parents Catherine and Robert, and my brother Shane, without whom I would never have made it this far.

Finally, a special thanks goes to Erica for her endless emotional support and for forcing me to have a life outside of school during this process.

TABLE OF CONTENTS

Page

TABLE OF CONTENTS (Continued)

Page

TABLE OF CONTENTS (Continued)

Page

LIST OF FIGURES

Figure Page

LIST OF TABLES

Table Page

1.0 Introduction

Constraining and understanding the development, evolution, and timescales of large silicic magma systems is important to understanding the development of granite batholiths, the volcanic-plutonic connection, and the development of the continental crust. Previous studies addressing the development of large silicic systems (e.g de Silva, 1989; Lipman, 2007; de Silva and Gosnold, 2007; Salisbury et al., 2011) demonstrated that these systems are constructed episodically of spatiotemporally related, but individual volcanic/magmatic events. Given the demonstrated strong petrochemical kinship and overall similarity in dimensions and spacing between calderas and plutons (Bachmann et al., 2007), it can be inferred that the spatiotemporal record of volcanism is the surface record of the plutonic system at depth and furthermore that the plutonic/batholithic systems is also an amalgamation of related but individual and episodically emplaced plutons and magma batches (de Silva and Gosnold, 2007). However, the volcanic-plutonic connection, timescales and longevity of these individual systems remains obscure.

Attempting to answer remaining questions about the nature of these individual systems and bridge the volcanic-plutonic, recent work in large silicic systems has shown that micro-analytical petrological, geochemical, and geochronological analysis of accessory minerals, such as zircon, from juvenile volcanic products can lend a more in-depth perspective of the nature of the magmatic system from which they came. This can reveal characteristics such as magmatic source (e.g. Reid et al., 1997), magma residence time (e.g. Reid et al., 1997; Brown and Fletcher, 1999; Vazquez and Reid, 2002; Schmitt et al., 2003a), and magmatic conditions and maturity (e.g. Miller et al., 2007). To build on these studies and further the understanding of the evolution and development of large scale silicic systems and the individual systems that make them, the Altiplano-Puna Volcanic Complex has been chosen as a natural laboratory (Figure 1).

Over two decades of stratigraphic, volcanologic, petrologic and geochronologic work on the Altiplano-Puna Volcanic Complex (APVC), located in the Andes Mountains of South America, has established it as one of the best examples of a large-scale silicic system in the world (de Silva, 1989; Watts et al., 1999; Schmitt et al., 2001; Lindsay et al., 2001). Over the past 10 million years the APVC has experienced a volcanic flare-up during which episodic storage and eruption of large volumes of silicic magma occurred; likely due to extensive thermal maturation of the crust from an anomalous mantle heat input (Salisbury et al., 2011; de Silva et al., 2006a). The flare-up climaxed about 4 Ma, and since peak activity the temporal and spatial record of volcanism suggest a waning of the system with the most recent episode of volcanism comprising a series of late Pleistocene dacite to rhyolite lava domes that share a general petrochemical resemblance to the numerous large ignimbrites produced during the flare-up (Figure 2; de Silva et al, 1994; Watts et al., 1999; de Silva and Gosnold, 2007, Salisbury et al., 2011). These domes provide a great opportunity to probe the relatively poorly understood most recent stage of the APVC magmatic system, and address remaining questions about the timescales and evolution of not only the individual magma batch or batches that formed the domes, but also their relationship to the APVC system as a whole.

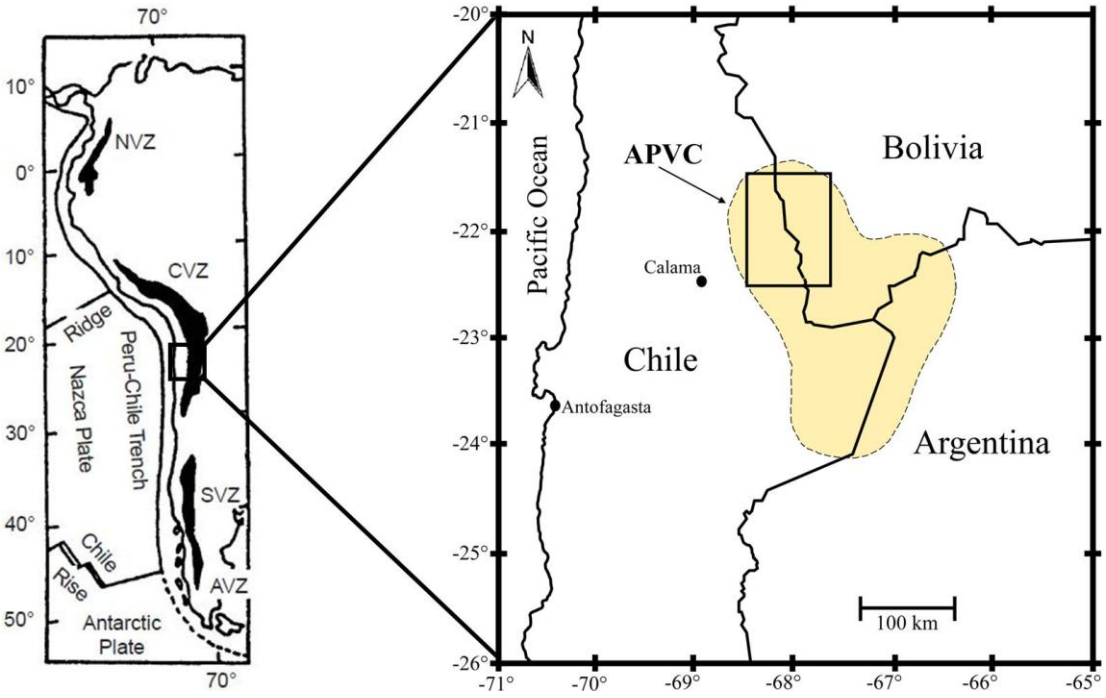

Figure 1. Map of Andean volcanic zones and APVC region of the CVZ. Box on APVC represents location of dome study area (Figure 2).

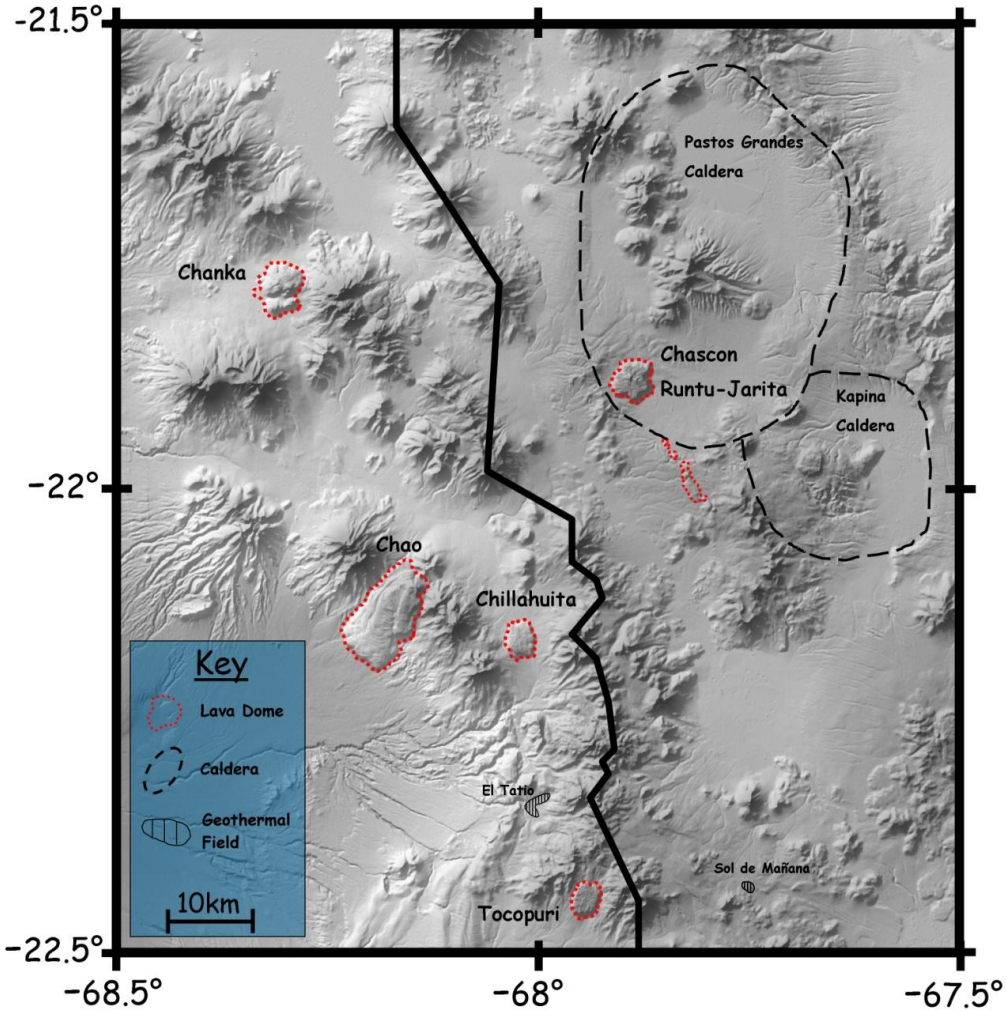

Figure 2. Map of the five major domes along with other regionally significant calderas and geothermal fields.

Table 1. Table of the domes and their coordinates.

	General Location	
Dome	**Latitude**	**Longitude**
Chao	22° 08' 07" S	68°15' 11" W
Chillahuita	22° 32' 11" S	68°01' 53" W
Tocopuri	22° 36' 21" S	67°57' 15" W
Chanka	21° 47' 09" S	68° 18' 37" W
Chascon-Runtu Jarita	21° 53' 02" S	67° 54' 18" W

1.1 Research Objectives

Previous work suggests that these dome eruptions represent the most recent episode of activity from the APVC and furthermore may have a shared source. With this in mind, the overall goal of this study was to employ a micro-analytical approach on the lavas of these domes to probe their magmatic history and answer a number of questions on the architecture, longevity, and thermal maturity of the magma source or sources that fed their eruptions.

1) Was the magma that fed these domes evacuated from distinct batches of magma or a larger shared source?

Previous work (de Silva et al., 1994; Watts et al., 1999) indicated that these domes share a petrochemical and morphological similarity, but the timing of the development of the magmatic system that fed the eruptions of these domes remained obscure and many questions lingered including if these eruptions tapped distinct batches of magma that formed relatively near the time of eruption, or if the eruptions potentially tapped a longer-lived shared source.

2) How long the magma was present in the crust before eruption (i.e. magmatic residence time)?

To further explore the history of the magmatic system feeding these dome eruptions, investigation of how long the magma was present in the upper-crust prior to eruption was needed. The primary question being: was the magma present for just several thousand years prior to eruption or had it been present for up to several hundred thousand years?

3) What does the eruption of these domes represent for the overall APVC system?

Previous studies have shown that the APVC has a waning trend of volcanic output since ~ 4 Ma (i.e. de Silva and Gosnold, 2007). While this overall trend could be argued as the strongest evidence for the waning of the APVC system, these domes provide direct opportunities to probe the relatively recent state of the APVC magmatic system, but also invoke the important question; do these effusive lava dome eruptions represent the last gasps of a waning APVC system, or do they perhaps represent the onset of a new cycle of volcanism?

Answering these three primary questions in addition to other questions that may be created from them will help to answer questions on the architecture, longevity, and thermal maturity of the magma source or sources that fed their eruption. Together this will lead to a better model of the magmatic source of these domes and their implications for the overall APVC system.

1.2 Geologic Background

1.2.1 Andes Overview

The Andean mountains are a continuous chain ranging nearly 8000 km along the western coast of South America (Figure 1) and are an excellent example of an ongoing convergent continental margin. Subduction along this margin has been occurring since the Late Triassic (James, 1971a), however the modern configuration of the Andean orogeny was initiated during the Late Oligocene when the Farallon plate was broken into the Cocos and Nazca plates (Sempere et al., 1990). As a result of changes in the along-strike geometry of the subducting plates, the magmatic character and evolution of the Andes is not consistent throughout the margin. Present and former subduction regimes can be divided into regions of shallow-dipping (<10°) and steeply-dipping (~30°C) zones. Areas of active volcanism are related to a relatively-steep subduction

zone. As a result of these differences in subduction geometry, modern day magmatism can be divided into three discrete segments (Figure 1; Gansser 1973). The Northern Volcanic Zone (NVZ) extends from 5°N to 2°S, the Central Volcanic Zone (CVZ) between 14° S and 28° S and the Southern Volcanic Zone (SVZ) from 30° S to 42°S.

The Central Volcanic Zone extends from 14°S to 28°S and crosses through southern Peru, Bolivia, and Northern Chile and Argentina. Differences exist between the CVZ from the other zones in that it is composed dominantly of dacite to rhyolite while the NVZ and SVZ are more commonly basaltic to andesitic in composition (Thorpe and Francis, 1979). Additionally, studies have shown that the CVZ is underlain by thick crust of up to 70 km and Paleozoic/Proterozoic in age while the NVZ and SVZ are Mesozoic in age and thinner at ~30km (James, 1979b; Coria et al., 1982).

1.2.2 Evolution of the Central Volcanic Zone

While the evolution of the CVZ before the Mesozoic is not well constrained, what is known is that CVZ has experienced a number of major cycles (Coira et al., 1982). The first of these cycles is the Precambrian "Pampean Cycle", which produced the basement rock of the region. These rocks have been dated at ~600 Ma and consist mainly of slates, phyllites and schists of greenschist facies which have been intruded by granitic to granodioritic magma bodies. In the Paleozoic the evolution can be described as a single orogenic event, the "Hercynic Cycle". This cycle was characterized by short periods of deformation separating alternating periods of sedimentary and volcanic periods. The cycle can be further divided into two distinct periods. The "Ocloyic Phase" occurred at the Ordovician-Silurian boundary and was dominated by the metamorphism and folding of Ordovician sediments occurring simultaneously with the emplacement granotoid plutons. This was followed by the "Chanic Phase" at the Upper Devonian-Lower Carboniferous boundary and is characterized by a large scale orogenic event across the southern and central Andes

that caused both folding as well as the emplacement of large calc-alkaline plutons in northern Chile and Argentina. The end of this cycle is represented by the cessation of large-scale sedimentation and the appearance of a magmatic belt in the Late Permian-Early Triassic. During the bulk of the Triassic the Andes in this area experienced little sedimentation and magmatism, and that which did occur was not caused by any major cycle.

In the early Jurassic the modern "Andean Cycle" began in response to the subduction of the Pacific Plate. The beginning of this cycle was marked by the formation of a volcanic arc with an associated back-arc basin forming to the west of the arc. Within this basin, a thick volcaniclastic sequence was deposited until the basin was closed during the Middle Cretaceous, likely as a result of the opening of the Atlantic and westward movement of the South American Plate (Coira et al., 1982). With the opening of the Atlantic and westward movement of the South American Plate in the Late Cretaceous, major deformational and mountain building events began with the change from an extensional to compressional regime (Sempere, 1997). In the Miocene major uplift occurred in the region and has carried on until the present (Gregory-Wodzicki, 2000). The crustal shortening and uplift lead to the formation of the Altiplano-Puna plateau, which now dominates the Central Andes. In addition to the tectonic changes since the late Cretaceous, major volcanism in the Central Andes has continued and stepped eastward through time to its modern state.

In its modern form the Central Andes exhibits many changes both along and across strike. Along strike in the central Andes it has been recognized by numerous authors (Coira et al., 1982, Jordan et al., 1983; Coira et al., 1993; Allmendinger, 1997) that the dominant control on volcanism is the dip of the subducting Nazca plates. In the CVZ (14° S to 28° S), the slab is steeply dipping (~30°) and thus this region exhibits a typical magmatic arc, however to the north and south of the CVZ the Nazca plate is shallow dipping and thus these regions experience limited volcanism. Perpendicular to strike, the Central Andes occur as two North-South trending sub-parallel mountain

belts that mimic the coast of South America. The western most of these belts, the Western Cordillera, represents the modern subduction related magmatic arc. The eastern mountain belt, the Eastern (or Oriental) Cordillera, is composed mainly of Paleozoic sediments that were folded and thrust during the Miocene. Very little volcanism occurs in the Eastern Cordillera relative to the Western Cordillera. Between these two mountain belts is the Altiplano-Puna Plateau and associated Altiplano-Puna Volcanic Complex (Jordan et al. 1983; Allmendinger 1997; Gregory-Wodzicki 2000)

1.2.3 Evolution of the Altiplano-Puna Plateau

The Altiplano-Puna Plateau, second to only Tibet in elevation and extent, has an average elevation of roughly 4 km and stretches for 1800 km along the Central Andes with a width of 350–400 km (Allmendinger, 1997). Shallowing of the subducting slab around 26 Ma and the subsequent changes in slab geometry lead to varying amounts of crustal shortening and thickening along the orogen which caused the uplift of the plateau from 25 to 14 Ma (Isacks, 1988; Allmendinger, 1997; Kay et al., 1999). During the Late Oligocene and into the Miocene steepening of the slab initiated, causing the onset of a broad zone of arc magmatism on the plateau during the middle Miocene. As the slab continued to steepen in the middle Miocene it increased the volume of the mantle wedge and the subsequent upwelling of hot mantle promoted melting of the well hydrated lithosphere and lower crust (Coira et al., 1993; Allmendinger et al., 1997; Kay et al., 1999). In addition to the steeping slab, delamination of the continental lithosphere likely occurred (Kay et al., 1999). The combination of a steepening slab and delamination lead to a large increase in mantle power input into an already thick and hydrated crust leading to subsequent large-scale melting and the eventual formation of the Altiplano-Puna Volcanic Complex.

1.2.4 The Altiplano-Puna Volcanic Complex

The Altiplano-Puna Volcanic Complex (APVC) is located at the southward transition of the Altiplano to the Puna, and forms a barren highland with an average elevation of around 4000 m with individual volcano summits of reaching nearly 6000 m (de Silva et al., 2006a,b). Centered near the political junction of Bolivia, Chile, and Argentina (Figure 1), the dominantly silicic volcanics from the complex cover ~70,000 km^2. The volcanic flare-up that now defines the region had its onset around 10 Ma and is responsible for over 30,000 km^3 of ignimbrites and lavas between 10 and 1 Ma (de Silva et al., 2006a). Many previous authors and studies have examined the 10 Ma history of ignimbrite deposits (i.e. de Silva, 1989; Salisbury et al., 2011) and better constraints on the size, origin and timing of these deposits have been developed. It has been recognized that the volcanic activity was focused from a number of major calderas in four major pulses of ignimbrite eruptions occurring at 10, 8, 6 and 4 Ma (Figure 3 and Figure 4; de Silva and Gosnold, 2007; de Silva et al., 2006a). The pulses show increasing intensity through time and then a large diminution after 4 Ma. Furthermore, the volcanic activity during the flare-up seems to have become more focused with time (Figure 4; de Silva and Gosnold, 2007). The spatiotemporal pattern lead de Silva and Gosnold (2007) to suggest that the plutonic roots of this system form a large upper-crustal batholith which was built episodically in pulses becoming more intense and focused in time. This intensity and focusing was in response to the mechanical evolution and thermal maturation of the crust which promoted larger bodies of magma in the upper crust with time (de Silva et al., 2006a). The pattern seen in the APVC mimics that of other large silicic magma systems (Figure 3).

However, while a general waning of the system has occurred since the 4 Ma and also the last ‘super-eruption’ in the APVC (the 2.6 Ma eruption of Pastos Grandes ignimbrite) the system has not expired completely. The presence of a very-low velocity layer beneath the APVC has been referred to the Altiplano-Puna Magma Body by some studies (Figure 4; Chmielowski et al., 1999; Zandt et al., 2003; Leidig and Zandt, 2003) and may represent an active body of partial melt. Volcanically, the

most recent (non-arc related) activity is represented by a number of late Pleistocene domes. Additionally, other forms of activity also persist, such as continuing deformation at Uturuncu (Sparks et al., 2008) and ongoing activity at El Tatio and Sol de Manana geothermal fields (de Silva et al., 1994).

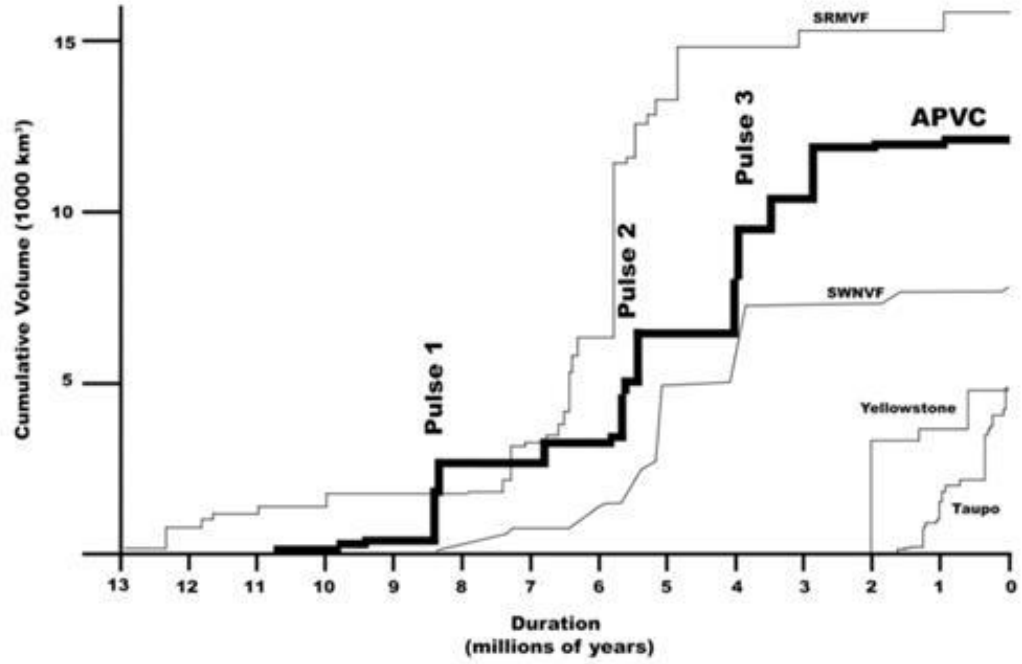

Figure 3. Graph of APVC cumulative volume vs. time. Bold line shows cumulative volume of APVC eruptions through time, note the three eruptive pulses and overall system waning since 4 Ma. (figure from Salisbury et al., 2011)

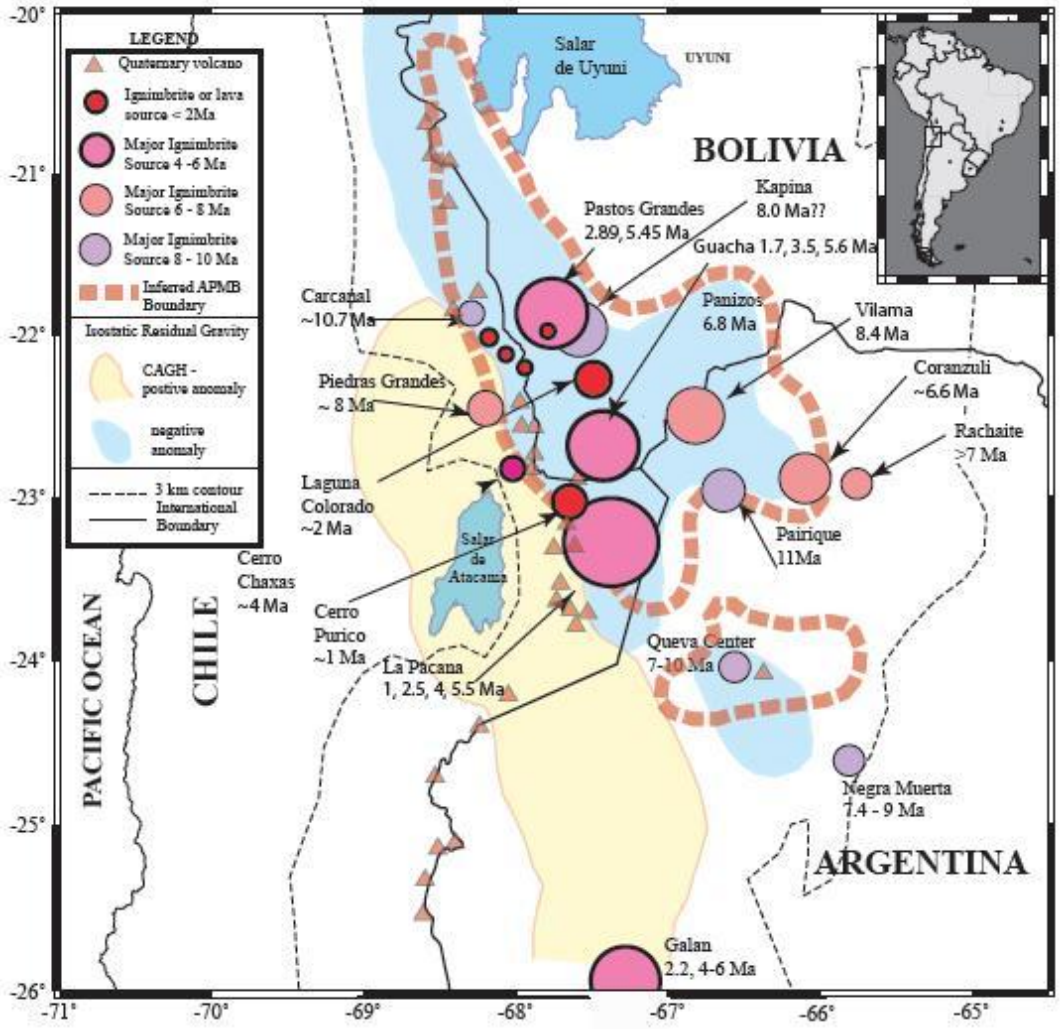

Figure 4. Map showing the spatiotemporal and size distribution of major ignimbrite eruptions within the APVC. Also shown are the approximate boundaries of the APMB (Figure modified from de Silva 2006a)

1.2.5 Late Pleistocene Domes of the APVC

Chao, Chillahuita, Chanka, Chascon-Runtu Jarita, and Tocopuri are the largest of the late Pleistocene domes. Previous authors (i.e. de Silva et al., 1994; Watts et al., 1999) studying these domes in more detail have noted the strong similarity between the domes and their similarity to the APVC ignimbrites, thus inferring that they are likely a continuation of the APVC system. All of the domes are morphologically youthful

and previous dates placed the age of the domes from 1.4 Ma to 100 Ka. They are dacitic to rhyolitic and crystal rich (>50%) and have other strong similarities. Additionally, all of the domes exhibit andesitic enclaves to varying degrees. Together they total a combined volume of >40 km^3, and are distributed over a roughly elliptical area of over 2000 km^2 centered at nearly 22°S 68°W (Figure 2). The majority of the domes exhibit the typical 'torta' shape seen in many APVC lava domes, with steep sides and a flat top.

Chao (also known as Cerro Chao) is located at roughly 22°08'07"S and 68°15'11"W between the composite cones of Paniri and Leon (Figure 2). It was erupted in three phases, the first being a minor explosive phase totaling ~1 km^3 of erupted products. The second and third phases were much larger and dominantly effusive (de Silva et al., 1994). All together, the Chao products constitute a 14 km long coulee total over 26 km^3 in volume, making it the largest known Quaternary silicic lava body in the world. The erupted products are crystal-rich, high-K dacites and rhyodacites and there is little evidence for pre-eruptive zoning in the magma body. Given the presence of ovoid mafic enclaves in the second and third phase, de Silva et al. (1994) hypothesized that the eruption of Chao was driven by intrusion of fresh, hot andesitic magma into a crystallizing and largely homogenous body of dacitic magma. Furthermore, it was suggested that the large volume of Chao is a function of both the steep local slope of up to 20° and also the large volume of available magma.

Chillahuita (also known as Cerro Chillahuita) is located at 22°32'11"S and 68°01'53"W (Figure 2). It appears to be the product of a single extrusive event with no evidence for explosive activity. It is a circular body of the typical "torta" shape with an area of about 11 km^2 and a volume of around 4 km^3. It was erupted onto a slope of 3°-4° and thus flowed slightly down slope to the north and east from its vent, located at the southern side of the lava (de Silva et al., 1994).

Tocopuri (also known as Cerro Tocopuri or sometimes as La Torta) is located at 22°36'21"S and 68°57'15"W between Volcan Michina to the east and Volcan Tatio to

the west (Figure 2). Similar to Chillahuita, it appears to be the product of a single eruptive event with no explosive component. It is a circular body of the typical "torta" shape with an area of about 11 km^2 and a volume of around 4 km^3. However, unlike Chillahuita its was erupted onto flat ground (de Silva et al., 1994)

Chanka (also known as Cerro Chanka or sometimes as Pabellon) is located north of Chao at 21°47'09"S and 68°18'37"W on the western flank of Volcan Azufre (Figure 2). Chanka has a slightly differing morphology than Chillahuita or Tocopuri in that while it is also a steep sided dome it consists instead of three lobes, each with a diameter of 1.5 km.

Chascon (also known as Cerro Chascon) located east of Chao and Chillahuita at 21°53'02"S and 67°54'18"W is the largest dome in the Chascon-Runtu Jarita (CRJ) complex located within the Pastos Grandes Caldera (Figure 5), although it is not thought to be related to the formation of the caldera or the Pastos Grandes system (de Silva et al., 1994). Chascon displays the typical "torta" from with an erupted volume of around 5km^3. A comprehensive study of the complex was conducted by Watts et al. (1999). Unlike the other domes, the CRJ complex displays abundant evidence of magma mixing between the silicic and andesitic components. Two groups of domes are defined chemically and geographically. A northern group, including Chascon, is dominantly rhyodacitic in composition with relatively little andesitic magma. The second group is the southern domes, and comprises a linear chain of six small domes of <1 km^3 total volume. These southern domes are composites of dacite and rhyolite lavas with some mafic enclaves. Similar to Chao, Watts et al. (1999) suggests that eruption of both the northern and southern groups was triggered by mafic recharge.

Figure 5. Picture of Chascon. (Provided by J. Kaiser)

2.0 Purpose and Scope

While it is clear that these five domes are similar and represent the youngest phase of volcanism in the APVC the chronology of the domes was not well constrained from previous studies. de Silva et al. (1994) had suggested they could potentially overlap in time with the youngest major ignimbrite in the region (Tatio Ignimbrite at 0.703 ± 0.01 Ma; Salisbury et al., 2011), initiating a motivation to address the potential link. Initial zircon work showed not only that the previous K-Ar and Ar/Ar ages for most of the domes were poor, but furthermore hinted at a coherent history. These initial findings lead to the overall goal of the study to address the magmatic timescales and also lead to a few hypotheses.

2.1 Hypotheses

Hypothesis 1: The magma that fed these domes was evacuated from a larger shared regional source.

To address this hypothesis the first step was to more rigorously demonstrate the similarity of the domes and their lavas to each other. Following this establishment, accurate eruption age coupled with U-Series and U-Pb isotopic dating on a large number (~50) of zircon crystals found within each of the five major domes would be obtained. Using both the distribution and pattern of the zircon crystallization age population from each dome (e.g. Reid et al., 1997), in addition to zircon trace element analysis, we would able to infer whether the magmas were sourced from a shared or distinct magmatic body. If the zircon age distribution from multiple domes showed a similar pattern or shared spikes in crystallization then we can argue that the magma either shared a source or shared a very similar magmatic history.

Hypothesis 2: The residence time of the magmas was extended and well over 100 kyr

Zircon crystallizes in a magma once saturation conditions are met, and in silicic magma chambers this saturation is common during evolution or pre-eruptive history (Harrison and Watson, 1983). The age of this crystallization can be dated through U-Th or U-Pb methods and while dating the age of the crystal is significant in and of itself, it is also significant in the fact that it indicates that magma was present at that point in time. The implication for residence time is that if zircon crystallization ages range continuously from eruption to a given point, it represents that magma was present continuously over that interval of time (i.e. magma residence time). However, an inherent drawback of this technique arises when magma is present but has not reached zircon saturation conditions, and hence zircon will not exist to indicate that the magma was present at the time. Thus, the residence time of magmas derived through this technique must be inferred to be a minimum value, as it is likely that the magma was present for some time prior to reaching zircon saturation.

Additionally, any estimate of eruption time may only be inferred to date as far back as zircon was being *continuously* crystallized. If presented an episodic array of start-and-stop zircon crystallization it could not be discerned if magma was present between crystallization intervals or if magma was only present during those periods when crystallization was taking place.

Considering that the value is a minimum, the expectations for this study are to find continuous spectra of zircon ages that span from eruption to a few 100 ka and thus a minimum residence time of well over 100 ka.

Hypothesis 3: Despite the eruption of these domes our data support previous findings suggesting that the APVC is overall a waning system.

To explore this hypothesis one line of evidence that needs to be examined is inspecting the textural maturity of lavas as this can give details about their source and

its thermal state. Additionally, the age range of zircon found in these lavas could reveal information regarding the thermal state of their source. If the source of these lavas was heated past the point of zircon saturation, older zircon antecrysts and xenocrysts would not survive and would not be found in these domes. However, they are found, and their presence in the lavas suggests that thermal rejuvenation and associated temperature rise was insufficient to cause complete resorbtion of the antecrysts, this suggests that the system may still be waning despite this injection of a more mafic magma.

2.2 Methods

A number of methods were used during the course of this study in attempting to answer the primary questions. A short summary of the employed methods employed follows, however more detail on specific methods can be found in the both the background and result chapters.

Sample Collection

Samples from a number of domes, including the five from this study, were collected to gain an array of spatiotemporal data and avoid focusing the data on narrow geographical locations or age groups. Samples were typically taken from the primary lava present. Clean rocks were collected; altered or weathered surfaces were avoided. These samples supplement an already extensive collection obtained from past studies.

Mineral Separation

Separation of minerals for analyses, including Zircon, Sanidine, Biotite, and Fe-Ti oxides was conducted via physical (crushing), magnetic, acid, and heavy liquid techniques at Oregon State University.

Thin Section Petrography

Thin section petrography can be used to gain an understanding of mineralogical and textural relationships in the lavas. Mineral abundances were measured using a 500 count grid on a petrographical microscope at Oregon State University.

Whole Rock Major and Trace Element Geochemistry

Whole rock X-Ray Fluorescence (XRF) and inductively coupled plasma mass spectrometry (ICP-MS) provide accurate estimates of whole-rock major and trace elements. Analyses were conducted at Washington State University.

Fe-Ti Oxide Thermometry

Analysis via Electron Microprobe (EMPA) of equilibrium Fe-Ti oxides found in the lavas allow for the estimation of the magmatic conditions just prior to eruption. Measurements were conducted at Oregon State University.

$^{40}Ar/^{39}Ar$ Dating on Biotite

$^{40}Ar/^{39}Ar$ on Biotite or Sanidine dating allows for the accurate estimation of the eruption age of silicic volcanic products. Analyses were conducted at the University of Wisconsin, Madison.

U-Th and U-Pb Dating on Zircon

U-Th or U-Pb analysis on zircons via Secondary Ionization Mass Spectrometry (SIMS) provides the crystallization age of the zircon and can be used to gain an understanding of the magmatic history. Analyses were conducted at the University of California, Los Angeles.

Table 2. Table of research goals, objectives, hypotheses and methods.

Goals	Objectives	Hypotheses	Methods
Constrain the timeframes and evolution of the plutonic/magmatic system	Determine if eruptions tap distinct patches of magma or if the eruptions tap a regional source.	The magma that fed these domes was evacuated from a larger regional source.	Use distribution and pattern of the zircon crystallization ages obtained through U-Th and U-Pb dating to look for shared history.
	Constrain the timing of the development of the magmatic system by identifying the residence time of the magma.	The residence time for these magmas was extended and well over 100kyr.	Ar/Ar eruption dating in conjunction with U-Th dating of zircon populations to establish a continuous range of dates that can indicate magma residence time from each dome (~50 zircon samples each)
Address if these domes represent rejuvenation of the APVC system.	Determine if the eruption of these domes represent thermal rejuvenation of the system or are just a variation from the overall trend.	Despite the eruption of these domes our data supports previous studies and findings suggesting that the APVC is overall a waning system.	Textural analysis of the lavas from the domes. U-Th and U-Pb dating of zircon to reveal the presence of older zircon antecrysts and xenocrysts.

3.0 Background

3.1 Large Silicic Magma Systems

Large silicic volcanic fields (LSVF) are collections of spatially and temporally related calderas and are regions of extensive silicic volcanism (dominantly >65% SiO2) which cover vast geographical areas (10,000s of km^2) with enormous volumes (1,000s to 10,000s km^3) of ignimbrites and lavas (Bachmann et al., 2007). The primary components of these fields are the regionally extensive ignimbrite sheets. Well known examples of such systems include the Southern Rocky Mountain Volcanic field (SRMVF), Long Valley, Toba, Yellowstone, and the Altiplano-Puna Volcanic Complex (APVC) (Bachmann et al., 2007). These systems are sometimes associated with "ignimbrite flare-ups" which are extreme episodes of volcanism dominated by ignimbrite eruptions with volumes that often exceed 1000 km^3 (Bachmann et al., 2007; de Silva et al., 2006a) and occur over in pulses over timescales of ~10 Ma. The volcanic flare-ups are thought to be the surface manifestation of catastrophic transient increase in mantle power input into the crust (Best and Christiansen, 1991; de Silva et al., 2006a). Given the large volumes of volcanic products from these ignimbrite flare-ups it has been thought that they are associated with voluminous plutonic activity (i.e. Hildreth 1981; Lipman, 1984; Bachmann et al., 2007). Ducea (2001) demonstrated the link between flare-up and cordilleran batholith formation for the Sierra Nevada Batholith. This finding supported the idea that the ignimbrite flare-ups were the result and surface manifestation of batholith formation in the crust (de Silva et al., 2006a).

Exploring this link further, de Silva and Gosnold (2007), examined the spatiotemporal pattern of the APVC flare-up and demonstrated that the development of the complex and batholith below occurred episodically. Additionally, the work demonstrated a three stage development for flare-ups. The first stage being an early stage of small volume eruptions and low magma production with a large spatial distribution, while the second stage is a "catastrophic" stage of enormous eruptions and large magma production with a focusing of eruption centers. The final stage characterized as a

waning stage with small eruptions and low magma production. This pattern is thought to be the result of the thermal and mechanical maturation of the crust due to overall elevated thermal input and elevated geotherm due to advection within the crust (de Silva et al., 2006a).

The patterns associated with ignimbrite flare-ups have implications for the formation of the associated batholith and the overall formation of the continental crust. Having established the incremental development of the batholithic systems, questions remain as to the architecture, development, and timescales of the individual plutonic bodies and their spatiotemporal link to associated volcanic products.

3.2 Longevities of individual systems

Considering that large silicic systems are built incrementally by related but spatiotemporally distinct plutonic bodies, the evolution and longevities of these individual systems has long been sought. A number of different methods have been used to explore these timescales, specifically the eruption of these systems and longevity of their magmas in the upper crust.

Numerous methods exist for determining the eruption age of silicic material, however by far the most common are K-Ar and $^{40}Ar/^{39}Ar$ dating. K-Ar is based on the measurement of the radioactive decay of ^{40}K to ^{40}Ca and ^{40}Ar, which occurs over a half-life of 1.248×10^{9} yr. Using this constant decay, the ratio of ^{40}K to ^{40}Ar can be used as a chronometer. Additionally, due to the high diffusivity of Ar at temperatures greater than 150°C, the ‘isotopic clock’ starts upon cooling past this temperature, and in most cases cooling past 150°C does not occur until eruption (McDougall and Harrison, 1988), thus making the system effective at dating eruptions.

Over the last few decades, the dating of $^{40}Ar/^{39}Ar$ in sanidine or biotite has become a very important tool in geology, as it is regarded as being ‘cleaner’ and more accurate that K-Ar dating. The primary difference in the $^{40}Ar/^{39}Ar$ technique being that ^{39}Ar has

a very short half-life and is thus not naturally present in the rock. It must, therefore, be created by irradiating the sample. The abundances of multiple K and Ar isotopes are measured, which eventually yield a $^{40}K/^{39}Ar$ ratio that is proportional to the $^{40}Ar/^{40}K$ ratio in the sample and therefore proportional to age (McDougall and Harrison, 1988). The short half-life of ^{39}Ar guarantees that limited to none was present in the sample prior to analysis. Any ^{39}Ar present can be assumed to have been created during irradiation, allowing for a cleaner indicator of the potassium content.

Similar to sanidine, biotite has also been frequently used to gather eruption age data. However, due to extraneous ^{40}Ar in biotite found in APVC lavas of very similar make-up, it has been shown that the age data may be erroneously older when compared to the more accurate date given by sanidine (Hora et al., 2010).

These age eruption dating techniques have been crucial in obtaining accurate chronology of the products of many large silicic volcanic systems including Yellowstone (Obradovich, 1992), the Southern Rocky Mountain Volcanic Field (Lipman et al., 1970; Lipman, 2007; Bachmann et al., 2007b) and the APVC (de Silva, 1989, Salisbury et al., 2011). This accurate chronology, in unison with accurate mapping, helped lead to the recognition that these large systems were emplaced over extended timescales (10s of Ma) and that their emplacement was episodic and composed of an amalgamation of related yet individual systems (Lipman, 2007, de Silva and Gosnold, 2007).

In addition to the chronology of the eruptive products, the longevity of the magma in the upper crust prior to eruption has also been investigated and attempted by a number of techniques. However, similar to eruption dating, focus has been placed on a few primary methods.

Over the last half-century, Rb-Sr dating has been important in uncovering timescales of magmatic processes. Given that ^{87}Rb decays to ^{87}Sr over a half-life of $4.8x10^{10}$ yrs,

the ratio of stable ^{87}Sr to ^{86}Sr can be used to determine fractionation timescales. $^{87}Sr/^{86}Sr$ isotope variation between glasses and phenocrysts phases can place constraints on the timescales of the differentiation process in silicic magmas (Christensen and DePaolo, 1993). When the ratio is higher in phenocrysts than the associated melts, it indicates that the ratio in the magma was increasing at a rate that was too fast for diffusive equilibrium between the crystal and liquid to keep maintain itself (Christensen and DePaolo, 1993). Given known rates of diffusion and the time required to re-equilibrate with the melts for these phenocrysts, one can constrain the amount of time since the event that caused the disequilibrium prior to eruption. Unlike U-Pb and U-Th this method does not date crystallization for the phenocrysts but rather dates the amount of time elapsed since an event that added Sr to the system. Examples of such events could be fractionation, assimilation, or mixing. It does still provide a means to determine timescales of this event and relative timescales of magma residence time. This technique has been applied widely to large silicic systems including Long Valley (Halliday et al., 1989; Christensen and DePaolo, 1993; Davies et al., 1994), the Southern Rocky Mountain Volcanic Field (Knesel et al., 1999; Charlier et al., 2007) and the APVC (Schmitt et al., 2001) and has been instrumental in determining the timescales of fractionation, assimilation or mixing. However, while these studies hinted at long timescales of residence in the upper crust (Hawkesworth et al., 2004) they were not ideal for addressing this subject and many questions remained. Thus while Rb and Sr isotopic systems are still applied for purposes of uncovering timescales, most modern studies investigating timescales, particularly magma residence, have focused on U-Th and U-Pb in zircon.

3.3 Zircon as a probe for large silicic magma systems

While many minerals, both common and accessory, have been used to explore the timescales of magmatism through various geochemical and isotopic methods, one of the best and most commonly used is zircon. In zircon, U is concentrated preferentially

over Th during zircon crystallization (Reid et al., 1997; Mahood and Hildreth, 1983) and, due to slow rates of diffusion for zircon, limited U or Th is lost or gained post-crystallization (Watson, 1996). Given that the saturation conditions for zircon are typically reached in silicic magma chambers (Watson and Harrison, 1983) crystallization of zircon in these systems is common. These characteristics make zircon useful in two common isotopic dating methods: U-Th and U-Pb. ^{238}U decays to ^{206}Pb through a series of shorter lived nuclides including ^{230}Th. For U-Th dating, given that the half-life of the ^{230}Th daughter is known (~75kyr for ^{230}Th), it can be used as a geochronometer based on magnitude of U-Th disequilibrium (Reid et al, 1997; Heumann et al., 2002a; Reid et al., 2003). However, the short half-life of the isotope also restricts the useful application of this method to zircons younger than ~350 ka. Therefore, to fill this gap and date older crystals, U-Pb dating can be used obtain accurate ages as old as ~4.4 billion years (Harrison et al., 2005). U-Pb dating is possible due to the existence of two simultaneous uranium-lead decay systems (^{238}U to ^{206}Pb and ^{235}U to ^{207}Pb) which both have extended half-lives (4.47 billion years and 704 million years, respectively).

In summary, U-Th or U-Pb dating of zircon populations can provide the time of crystallization for a particular crystal. Furthermore, when a multitude of grains are dated from a sample, the populations and distribution can help determine relative magma source and when coupled with eruption age can also determine magma residence (Figure 6).

Traditionally, U-Pb dates had been interpreted as the crystallization age of plutons because analytical uncertainties were large enough to encompass the expected life of the pluton (Miller et al., 2007). However with advances in analytical accuracy, the advent of in-situ SIMS analysis, and the continued development of U-Th analysis for younger zircons, many studies have successfully used U-Th and U-Pb dating on zircon, often combined with ^{40}Ar/^{39}Ar dating, as a tracer to address the development and evolution of large silicic systems (e.g. Reid et al., 1997; Brown and Fletcher,

1999; Vazquez and Reid, 2002; Schmitt et al., 2003b; Miller and Wooden, 2004; Walker et al., 2010). These studies have demonstrated the validity and usefulness of zircon in addressing a host of questions regarding the development of these systems, including, tracking assimilation of previous crustal material (both of previous but related plutonics or entirely unrelated basement protoliths) through the presence of antecrystic or xenocrystic zircon. Additionally, these studies have consistently shown that zircon begin to crystallize 10s to 100s of ka prior to eruption, attesting to long residence in the crust (Simon et al., 2008).

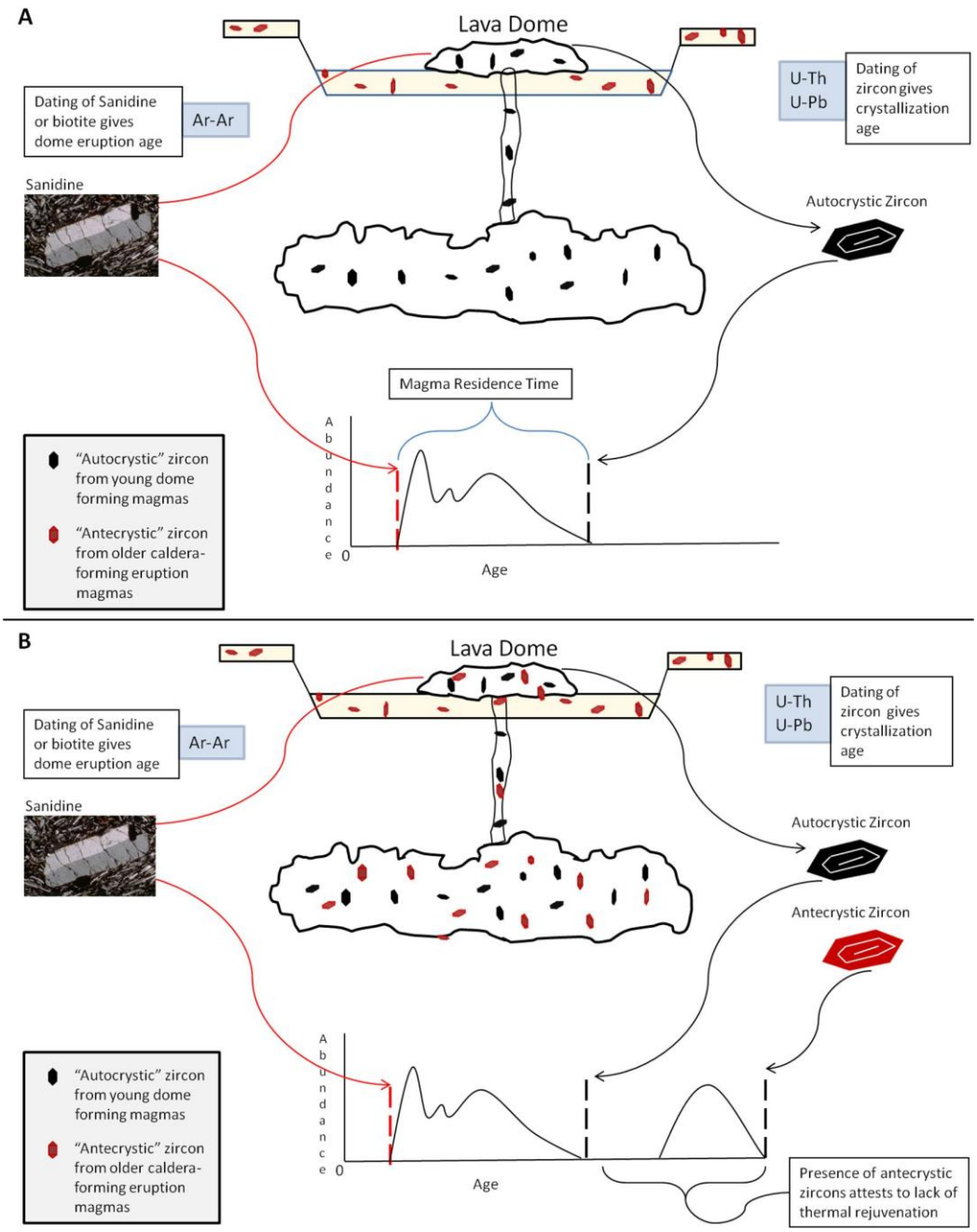

Figure 6. Conceptual figure with two methods by which dating of sanidine (or biotite) and zircon can be used to infer the history of magmatic conditions. A (Top) shows that the magmas that formed the lava domes do not contain zircon antecrysts, indicating thermal rejuvenation. A also shows how magma residence time in determined from zircon and sanidine dating. B (Bottom) shows that the magmas that formed the lava dome contain antecrysts; formed from the magma that fed the earlier caldera-forming eruption.

4.0 Field and Sample Observations

In addition to previous samples and studies from these domes, field work and sample collection was conducted on the Chilean side of the APVC during November of 2009. Since the field session was multi-focus and relatively compact, the primary goal for field session was to serve as an introduction to the field area and allow for additional sample collection to supplement the already significant knowledge base which existed for the domes. Observations were made and samples collected at four of the five primary domes of this study, with the exception of Chascon-Runtu Jarita, due to it being located in Bolivia and where a detailed study had already be conducted by Watts et al., (1999). In all cases, when samples were collected, care was taken to ensure that the samples were taken from the most representative, unaltered, and clean portion of the lava. Any noticeable differences within the lava were documented and samples were collected of all lava varieties.

Chanka (Figure 7) forms on the northwestern flanks of Volcan Azufre, a potentially active arc-related composite cone (de Silva and Francis, 1991). It differs from the other domes in that it is composed of three separate lava lobes, however it exhibits the same steep-sides nature with a small zone of talus and fallen blocks of lava at its base. Samples were collected along the northwestern flank of the dome of the primary silicic lava (09001CT) and of the mafic enclaves that make up a few percent of the lava (09002CT).

The primary silicic lava (09001CT, Figure 8) is crystal rich (up to 45% crystals) monotonous, leucocratic and porphyritic with the presence of large phenocrysts of feldspar, quartz, biotite and hornblende. The crystals are randomly distributed within a poorly but pervasively microvesicular groundmass which gives the lava a somewhat friable texture. No flow banding or obvious signs of mixing were seen. The mafic enclaves (Sample 09002CT, Figure 9) are moderately crystal rich (up to 30% crystals), melanocratic, and porphyritic with phenocrysts of hornblende, plagioclase and pyroxene with occasional quartz phenocrysts along the edges. Much of the large

quartz and some plagioclase look as if they were plucked from the silicic lava based on their proximity to the silicic lava, relative paucity in the mafic lava, and strongly sieved texture.

Chao (Figure 7) was erupted between two older and closely spaced arc-related composite cones, Paniri and Leon. Ogives on the surface of the dome indicate flow-direction down the slope created between the two composite cones. This flow has given the dome a slightly different morphological look than the other domes, however it still exhibits the characteristic steep-slopes with an apron of talus and lava blocks. Two observation and sample collection stops were made for Chao, the first of these was along the south side of phase two and the second along the south side of phase (i.e. de Silva et al., 1994). In total, four samples were collected from Chao. 09003CT (Figure 8) is a sample of the silicic lava and is crystal rich (up to 55% crystals), largely monotonous, leucocratic and porphyritic with large and obvious phenocrysts of feldspar, quartz, biotite and amphibole. The crystals are randomly distributed within a poorly but pervasively microvesicular groundmass which again gives the lava a somewhat friable texture. Additionally, some areas of the silicic lava appeared to be slightly more crystal rich (up to 60% crystals), though no other obvious differences were noted; 09005CT (Figure 8) is a sample of this lava.

No flow banding or obvious signs of mixing were seen, however mafic enclaves make up a few percent of the overall lava in phase two and range to 15 cm in size. 09004CT (Figure 9) is a sample of this mafic component, and similar to those found in Chanka, the sample is moderately crystal rich (up to 30% crystals), melanocratic, and porphyritic with phenocrysts of hornblende, plagioclase, and pyroxene with occasional quartz phenocrysts along the edges.

Lastly, on the flanks of phase one, a sample of the pyroclastic flow pumice (see stratigraphic column in de Silva et al., (1994)) was taken (09006CT, Figure 8). The sample is similar in crystallinity and appearance to the primary silicic lava, however, it displays much more vescularity. The pumices range up to about 50 cm in diameter.

Chillahuita (Figure 7) appears to flow slightly down a shallow slope, however it still exhibits the typical “torta” shape seen in so many APVC lava domes. It has a relatively flat top with steep-slopes and a small talus apron along its flanks. Sample 09009CT (Figure 8) was collected on the western flank of the dome and similar to the primary lavas of both Chanka and Chao, the silicic lava and is crystal rich (up to 50% crystals), largely monotonous, leucocratic and porphyritic with large and obvious phenocrysts of feldspar, quartz, biotite and amphibole. The crystals are randomly distributed within a poorly but pervasively microvesicular groundmass giving the lava a friable texture. Chillahuita also displays some mafic enclaves, however, they are smaller than and not as abundant as in Chanka or Chao. No samples of these enclaves were collected.

Tocopuri (Figure 7) was erupted near Volcan Michina, south of the Tatio geothermal field. However, unlike Chao or Chillahuita, it was erupted on relatively flat ground and thus displays the typical “torta” morphology with a flat top and steep-slopes with a small talus apron. Two samples were collected from the eastern flanks of the dome. 09011CT (Figure 8) is a sample of the primary silicic lava and is similar to the rest of the domes in that it is crystal rich (up to 60% crystals), largely monotonous, leucocratic and porphyritic with large and obvious phenocrysts of feldspar, quartz, biotite and amphibole. The crystals are distributed within a glassy and poorly, but pervasively, microvesicular groundmass. 09012CT (Figure 8) is also a sample of the silicic lava, however, it displays a darker groundmass and overall appearance than the other sample, proving it to be prudent to sample. Lastly, similar to Chillahuita, while displaying some small mafic enclaves, they are not as abundant as in Chanka or Chao therefore no samples of these enclaves were collected.

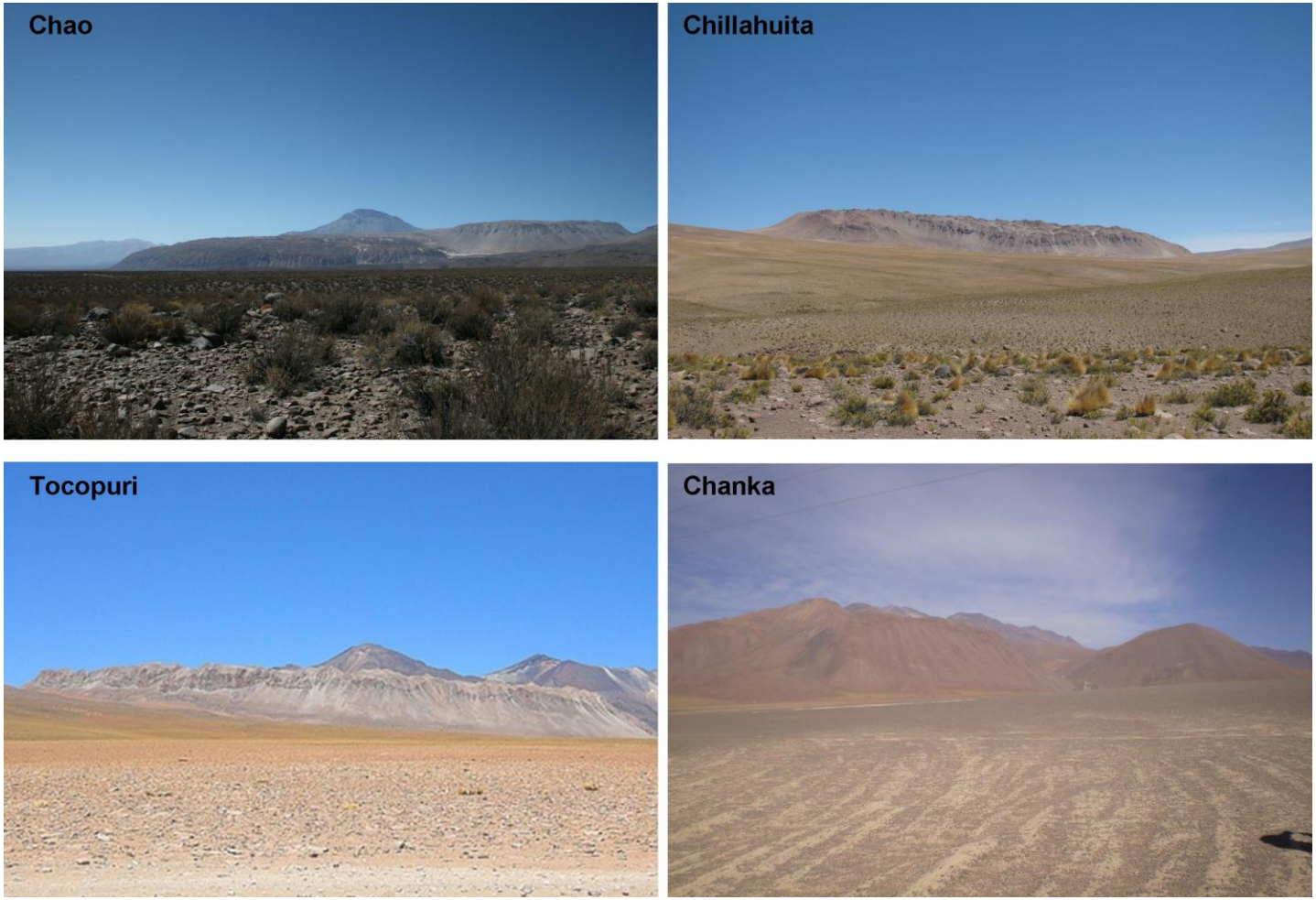

Figure 7. Pictures of Chao, Chillahuita and Chanka domes. Pictures taken during 2009 field season. Tocopuri picture source: Dropus. *Cerro La Torta*. Web. 9 Jun 2011. <http://www.panoramio.com/photo/18402460>.

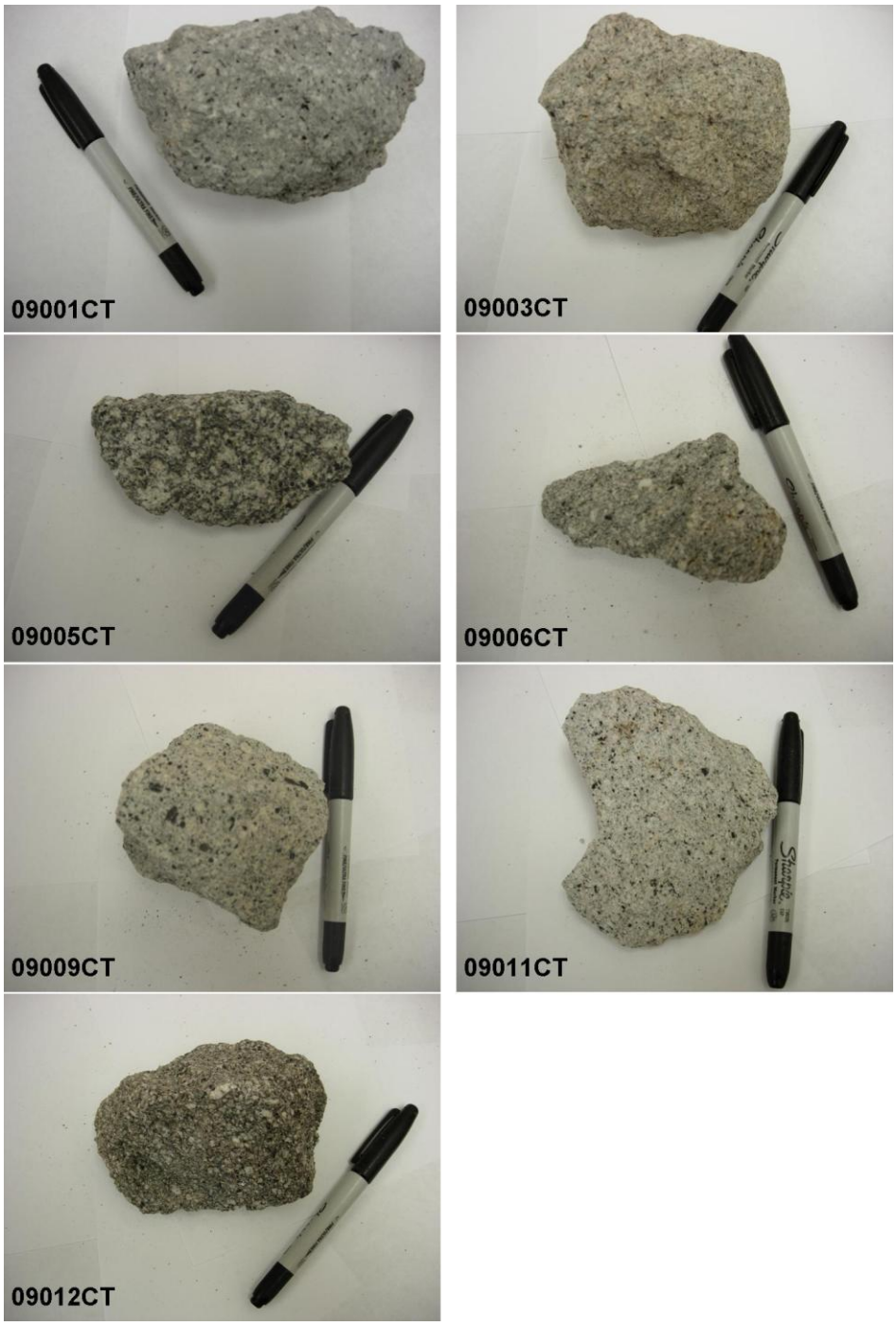

Figure 8. Pictures of silicic samples. *09001CT*: Chanka silicic lava. *09003CT*: Chao silicic lava. *09005CT*: Chao crystal rich silicic lava. *09006CT*: Chao pyroclastic. *09009CT*: Chillahuita silicic lava. *09011CT*: Tocopuri silicic lava. *09012CT*: Tocopuri Silicic Lava with darker groundmass. Sharpie used for scale is 13.7cm long.

Figure 9. Pictures of mafic enclaves from Chilean domes. *09002CT:* Chanka mafic enclave. *09004CT*: Chao mafic enclave. Sharpie used for scale is 13.7cm long.

Table 3. Table of sample type and location.

Dome	Sample	Description	Latitude	Longitude
Chanka	09001CT	Silicic Lava	S21°45.041'	W68°19.163'
	09002CT	Mafic Enclave	S21°45.041'	W68°19.163'
Chao	09003CT	Silicic Lava	S22°11.188'	W68°10.956'
	09004CT	Mafic Enclave	S22°11.188'	W68°10.956'
	09005CT	Silicic Lava	S22°11.226'	W68°10.950'
	09006CT	Pyroclastic	S22°11.705'	W68°11.588'
Chillahuita	09009CT	Silicic Lava	S22°08.356'	W68°01.766'
Tocopuri	09011CT	Silicic Lava	S22°27.563'	W67°58.547'
	09012CT	Silicic Lava	S22°27.563'	W67°58.547'

4.1 Summary

A total of nine samples were collected from the four Chilean domes, with seven of these samples comprising silicic lava and two being mafic enclaves. Overall the domes and the samples show striking similarities with few noticeable differences. Except where steep local topography dominates, (i.e. Chao), the domes exhibit a youthful

‘torta’ shape. The silicic lavas from all of the domes are crystal-rich and share the same phenocryst assemblage. These silicic lavas exhibit poor, but pervasive vescularity, with the exception of the Chao pyroclastics. All domes contain small and ovoid mafic inclusions to a few percent. These mafic enclaves also share similarities from dome to dome, including overall appearance, crystal content and phenocrysts assemblage.

Subtle differences exist between the domes and samples including slight morphological differences, changes in vescularity, and the slight variance in the amount of mafic material. Overall, the similarity greatly outweighs the differences within the domes, allowing use of our field observations to support previous studies (de Silva et al., 1994; Watts et al., 1999) in considering these domes as a group.

5.0 Petrology and Geochemistry

To supplement the previous reconnaissance studies at the four Chilean domes, accurate and up-to-date petrology and geochemistry are essential to give background and context to the domes of this study. It is needed to compare the domes to each other and to the APVC system as a whole, as well as highlight both similarities and differences that may be important in their formation and magmatic evolution.

Here data and observations from previous studies are combined with new petrography, whole rock geochemistry, geothermometery and barometry to provide the basic magma dynamic framework for these domes.

5.1 Thin Section Petrography

5.1.1 Previous work

de Silva et. al. (1994) conducted a detailed study of Chao, giving petrographical descriptions of thin sections from each eruptive phase. The typical phenocryst population of the silicic lava was plagioclase > biotite > hornblende > quartz >> sphene > sanidine > Fe-Ti Oxides, with apatite and zircon as the most common accessory phases. Phenocryst content ranged from 25 vol % in the pumice to >50 vol % in the lava. The matrix of the lavas was described as a colorless high-silica glass, which in some samples included microlites of the primary phenocrysts which make up to 50% of the matrix. This high phenocryst content and partially crystallized groundmass gives Chao a high overall crystal content (>60%). The andesitic enclaves were also analyzed and described as sparsely porphyritic, containing a few large phenocrysts of plagioclase, hypersthene, quartz, biotite and hornblende. These phenocrysts are set in a groundmass of randomly oriented hornblende, plagioclase, and hypersthene surrounded by a ‘small proportion of glassy mesostasis’.

Table 4. Modal phenocryst data for samples from Chao (from de Silva el. al., 1994).

	Pyroclastics		Pum. Cone	Chao I		Chao II		Chao III	
	84063	88069C	88080	88073	84024	88068A	88068C	88081	88067
Rock Type	dense juvenile	pumice	pumice	lava	lava	lava	vesicular lava	lava	lava
Glass/Matrix*	60	65	60	55	50	47	57	57	55
Phenocrysts									
Plagioclase	18	17	17	19	21	22	21	18	21
Quartz	6	5	8	8	10	6	6	7	6
Biotite	7	7	5	9	7	9	7	8	7
Hornblende	4	2	8	5	7	10	6	7	7
Fe-Ti Oxide	1	2	1	1	2	1	1	1	2
Sanidine	2	1	1	2	-	3	2	1	-
Sphene	2	1	-	2	2	2	tr	1	T
Apatite¥	T	T	T	T	T	T	T	T	1
Zircon¥	T	T	T	T	T	T	T	T	T
Allanite¥	T	T	T	-	-	T	-	-	T
%Phenocryts	40	35	40	45	50	53	43	43	45

All data are volume percent on the basis of 1000 points counted. Abundances for vesicular samples are calculated on a vesicle-free basis. T is trace and dash is not detected.

*Glass/matrix is treated as noncrystalline material in this data set

¥These minerals were detected only as discrete microphenocrysts or as inclusions

Watts et al., (1999) studied the Chascon-Runtu Jarita complex, giving detailed petrographical descriptions of both the Chascon and Runtu Jarita parts of the complex. The general phenocryst assemblage seen in the silicic lava of these domes is similar to that noted by de Silva et al. (1994) for Chao; plagioclase > quartz > biotite > hornblende > sanidine >> Sphene > Fe-Ti Oxides with Apatite as an accessory phase. Phenocrysts represent 44 to 48 vol% of the lavas. In the Chascon group lavas, the plagioclase is typically seriate textured exhibiting undulose extinction and is generally homogenous with a small range in composition. The quartz and sanidine show corroded rims with the quartz showing embayments and the sanidine appearing fractured. Biotite has shows reaction rims, and generally aligned with the flow texture of the groundmass. Hornblende is commonly associated with biotite clusters and sometimes shows alteration however is rarely completely altered. Sphene and Fe-Ti oxides are also present. The groundmass is rhyolite, displaying poor but pervasive

vesiculation. The groundmass of the lavas have a microlite-rich nature (up to 75%), with the microlites consisting of abundant plagioclase and minor biotite lathes in a vesicular glass.

Watts et al. (1999) reported that the Runtu Jarita domes have similar silicic lavas to Chascon, but the mafic lavas of this complex were studied in more detail, specifically from Dome C. The mafic lava has less overall phenocrysts and contains plagioclase > hornblende > hypersthene >> biotite, quartz and sanidine. The plagioclase is seriate and comes in two populations, one fresh and euhedral the other large and subhedral. Microphenocrysts of augite, hypersthene and hornblende are commonly associated with clusters of plagioclase. The groundmass is rhyodacite glass with plagioclase microlites. Xenocrysts of quartz are found in some places. Areas of banding between mafic and primary silicic lavas indicate mixing, however, the boundaries are sharp. Minerals were observed that were likely plucked from the silicic lava into the more mafic member, attesting to a one-way movement of crystals.

Table 5. Modal phenocryst data for samples from Chascon-Runtu Jarita (from Watts el. al., 1999).

	Chascon Group				Runtu Jarita Group			
	CCO1 Chascon - Dome K	CC04 Chascon - Dome K	CC30 Dome G	CC33 Dome H	CC12 Dome C	CC10 C - Mafic Flowfront	CC14 C - Mafic Flow	CC28 E - Mafic Flow
Glass/Matrix	54	55	52	56	53	72	71	72
Phenocrysts								
Plagioclase	21	25	27	27	25	18	17	16
Quartz	12	7	8	6	10	-	2	3
Biotite	10	7	8	7	7	-	1	2
Sanidine	2	4	2	2	4	-	1	1
Hornblende	1	2	2	2	2	4	3	3
Hypersthene	-	-	1	-	-	4	3	2
Sphene	T	T	T	T	T	-	-	T
FeTi Oxide	T	T	T	T	T	-	-	-
Apatite	-	-	T	-	T	-	-	-
% Phenocrysts	46	45	48	44	48	28	29	28

All data are volume percent on the basis of 500 points counted

5.1.2 Results

19 samples were collected during the 2009 Chile Field Season, and nine of the samples relate directly to four domes of this study, excluding only Chascon. Thin sections were created for each of these samples, which included the silicic lava from each dome, mafic enclaves from Chao and Chanka, and any additional samples worth collecting (i.e. vesicular lavas or pumice). The thin sections were used both for the petrography of the samples as well as EMPA Fe-Ti oxide analysis.

Samples were sent to Vancouver Petrographics where standard thickness, un-polished thin sections were created. Mineralogy and phase textures of the thin sections were then examined at Oregon State University using a petrographic microscope. Groundmass and mineral abundances were obtained using a 500 count grid with abundances for vesicular samples calculated on a vesicle-free basis (Table 6). Representative pictures were then taken of each thin section using a Nikon digital camera (DXM1200).

Table 6. Modal phenocryst data for samples for domes from this study.

	Chao				Chillahuita	Tocopuri		Chanka	
	09003CT	09004CT	09005CT	09006CT	09009CT	09011CT	09012CT	09001CT	09002CT
	Primary Lava	Mafic Enclave	Crystal Rich	Pyro-clastic	Primary Lava	Primary Lava	Primary Lava	Primary Lava	Mafic Enclave
Glass/Matrix	52	74	50	51	53	52	53	56	73
Phenocrysts									
Plagioclase	24	15	25	19	23	25	24	21	16
Quartz	5	2	7	5	6	7	7	5	2
Biotite	10	1	10	7	10	9	10	9	2
Hornblende	7	4	6	5	6	5	4	7	4
Fe-Ti Oxide	1	T	1	1	1	1	1	2	-
Sanidine	1	-	1	1	1	1	1	T	-
Sphene	T	-	1	1	1	1	T	T	-
Apatite	T	-	T	T	T	T	T	T	-
Hypersthene	-	4	-	-	-	-	-	-	3
%Phenocrysts	48	26	50	39	47	48	47	44	27

All data are volume percent on the basis of 500 points counted

Silicic Lavas

The dominant silicic lava from the domes (09001CT, 09003CT, 09009CT, 09011CT) all display similar characteristics. The general phase assemblage seen consistently between the silicic lavas from each dome is plagioclase at 21% to 25% followed by biotite, hornblende and quartz in varying abundances but generally ranging between 4% and 10%, followed by sanidine, sphene, Fe-Ti oxides at generally 1%, and lastly zircon and apatite seen rarely as accessory phases. The plagioclase phenocrysts are often large and display abundant sieving, while the quartz and sanidine display corroded rims and embayment textures (Figure 10). Biotite and hornblende commonly have reaction rims and often occur as laths which can be grouped together. The crystallinities of these lavas are very high, ranging from 44 to 48 vol% phenocrysts. The groundmass is poorly but pervasively vesicular colorless glass and often contains microlites, mostly of plagioclase (Figure 10B). The microlites push the crystallinity of the lavas even higher to upwards of 55-60%

Occasional differences were observed in the silicic lavas which mirror the differences seen in hand sample. Chao sample 09005CT has a slightly higher crystal content at 50 vol% phenocrysts, but all other characteristics are the same as the more dominant silicic lava (Figure 10C). Additionally, the Chao pyroclastic sample (09006CT) has more abundant vesiculation, but is similar to the dominant Chao silicic lavas in all other facets. Lastly, Tocopuri sample 09012CT has a slightly darker groundmass than in the more dominant silicic lava from Tocopuri (09011CT).

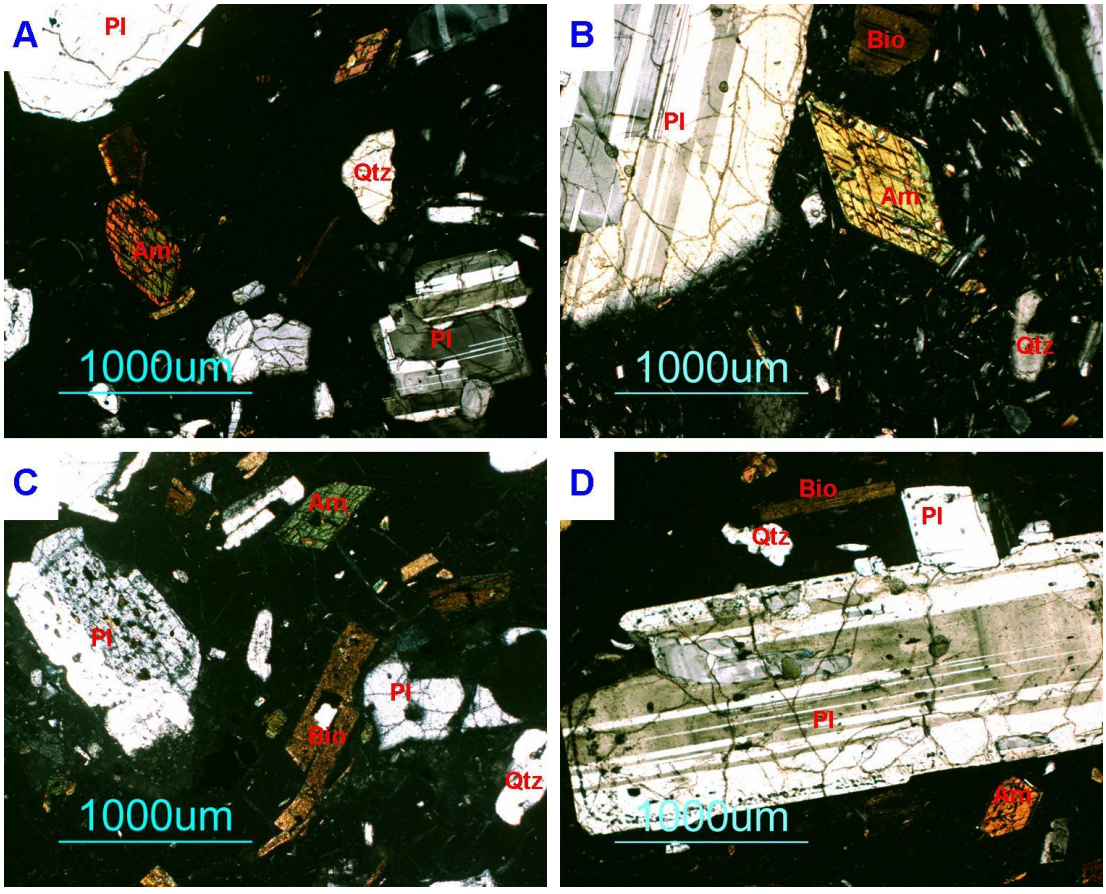

Figure 10. Pictomicrographs of notable characteristics from silicic lava samples. A) Representative sample of silicic lavas, note the large plagioclase and amphibole crystals along with the highly embayed quartz. B) Silicic lava with microlitic groundmass. C) Crystal-rich silicic lava from Chao. D) Large, euhedral and sieved plagioclase. Labels: plagioclase (Pl), amphibole (Am), biotite (Bio), quartz (Q).

Mafic Enclaves

Petrography from two thin sections of mafic enclaves, 09002CT from Chanka and 09004CT from Chao. share the phase assemblage of plagioclase at 15 to 16%, followed by hornblende (4%) and hypersthene (3 to 4%), followed lastly by quartz (2%) and biotite (1 to 2%) with trace amounts of Fe-Ti oxides. The majority of the large phenocrysts within the mafic enclaves show extensive signs of disequilibrium with the surrounding matrix (Figure 11A), plagioclase has abundant sieve textures, quartz has large embayments, and biotite, hornblende and hypersthene have reaction rims. Where the boundary between silicic and mafic magmas can be seen in thin section, it is generally sharp, however slightly more phenocrysts can be found near this boundary, attesting to potential plucking from the silicic magma (Figure 11B). The crystallinity ranges from 26 to 27%. The groundmass is less vesicular than the silicic lava, but is dominated by microlites which push the overall crystallinity of the enclaves to near that of the silicic lava (Figure 10).

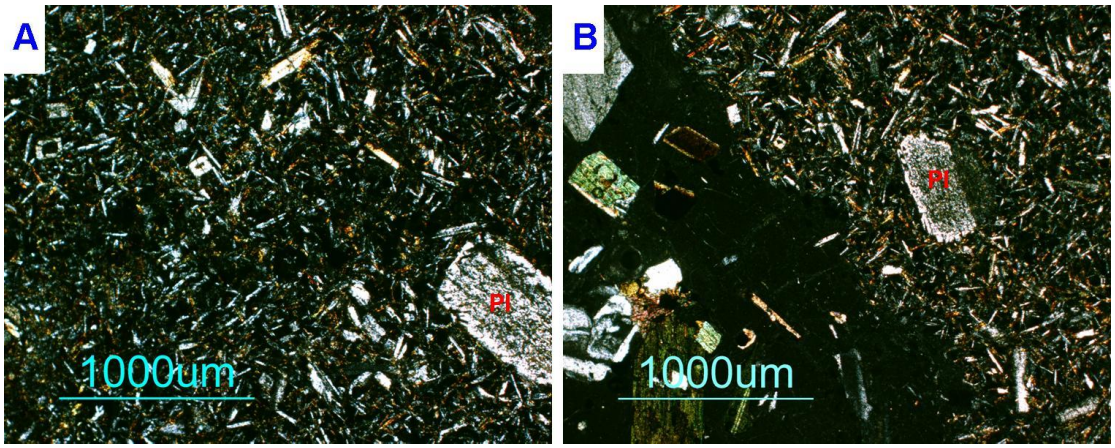

Figure 11. Pictomicrographs of notable characteristics from mafic enclaves. A) Representative mafic enclave, note the dominantly microlitic groundmass and the presence of a much larger but highly sieved and corroded plagioclase. B) Boundary between mafic and silicic lava types. Note the sharp boundary and the presence of the

plagioclase near this boundary. Labels: Plagioclase (Pl), Amphibole (Am), Biotite (Bio), Quartz (Q).

5.1.3 Summary

Overall, the dominant silicic lavas from these domes share a crystal rich nature, ranging from 44 to 50 vol% phenocrysts, while taking microlitic groundmass into account would push these crystallinities even higher. Relatively little modal variation exists between both the silicic lavas from the four domes analyzed for this study and also the Chascon-Runtu Jarita complex. However, variation does occur in special cases such as pyroclastic samples and mafic enclaves. The mafic enclaves analyzed from Chao and Chanka are very similar in nature, both displaying large phenocrysts which are probably plucked from the silicic magma into the less viscous mafic magma (i.e. Watts et al., 1999) and a dominantly microlite-rich groundmass, which contains occasionally hypersthene.

These results, and those from the previous studies, indicate that the magmas that fed these domes are similar from dome to dome, both mineralogically and texturally. Furthermore, the textures and crystal rich nature of these lavas indicate their overall advanced textural maturity and complex thermal history.

5.2 Whole Rock Chemistry

5.2.1 Previous Work

Whole rock X-Ray Fluorescence (XRF) and inductively coupled plasma mass spectrometry (ICP-MS) provide accurate estimates of whole-rock major and trace elements. Previous XRF whole-rock major and trace element data exists for all five primary domes from previous studies (e.g. de Silva et al., 1994; Watts et al., 1999).

de Silva et al. (1994) studied Chao and its three eruptive phases, noting that the primary silicic magma was calc-alkaline, high-K dacite, with little variation through the three phases in both major and trace elements. All trace elements in the silicic lava show restricted range in concentration, including U, Th and Pb. The andesite inclusions are more mafic and have lower Rb, Th, and Nb, with higher Cr, Sr, Y, and Zr. A single sample from the Chao 1 phase was found to be LREE enriched, with a Ce/Yb of 48, and $^{87}Sr/^{86}Sr$ ratio of 0.70805, and a $^{143}Nd/^{144}Nd$ ratio of 0.512247. de Silva et al. (1994) also compared Chao with the other four primary domes of this study, stating that these bodies are closely similar in composition to Chao, both in major and trace element concentrations. All the domes are LREE enriched with similar Ce/Yb and La/Sm. $^{87}Sr/^{86}Sr$ varies little from 0.70801 to 0.70805. The study noted that the lavas from the domes closely resemble those of the older ignimbrites and associated silicic lavas, but differ from the silicic lavas erupted from composite cones in the CVZ; with the exception of Chanka which the study states shares characteristics of the cones.

Watts et al. (1999) focused on the Chascon-Runtu Jarita dome complex, studying both the silicic and the mafic lavas found there. The study noted major differences between the silicic and mafic components, but a general similarity within each type. The silicic lavas were described as calc-alkaline, high-K rhyodacites and rhyolites, while the mafic lava was of andesitic composition. Trace elements show significant changes from silicic mafic magmas, with Rb and Th decreasing and Sr increasing. The study stated the trace elements show that the two groups of lavas were different systems with different histories, though mixing between the groups had likely occurred.

Representative data of silicic lavas from the previous studies are summarized in Table 7 and Table 8 while data of mafic enclaves is presented in Table 9.

Table 7. Previous XRF major and trace element data for Chao, Chillahuita, Tocopuri and Chanka. Data from de Silva et al. (1994).

	Chao						Chillahuita	Tocopuri	Chanka
	88073	88068A	88068C	88069	88067	88081	84054	84064	88072
	Chao I	Chao II	Chao II	Chao II	Chao III	Chao III			
SiO_2	69.77	67.71	69.08	68.07	68.10	67.80	68.79	71.46	65.09
TiO_2	0.52	0.52	0.46	0.49	0.50	0.54	0.49	0.37	0.54
Al_2O_3	14.12	15.48	15.27	15.57	15.33	15.29	15.46	14.96	15.01
Fe_2O_3	3.63	3.63	3.06	3.44	3.54	3.80	3.07	2.05	3.95
MnO	0.06	0.06	0.06	0.06	0.06	0.06	0.06	0.05	0.07
MgO	1.68	1.72	1.39	1.58	1.68	1.83	1.54	0.99	1.85
CaO	3.23	3.70	3.40	3.67	3.61	3.61	3.42	2.64	3.55
Na_2O	3.09	3.24	3.19	3.23	3.28	3.08	3.42	3.34	3.34
K_2O	3.78	3.75	3.94	3.76	3.75	3.78	3.66	4.08	3.69
P_2O_5	0.12	0.13	0.15	0.12	0.14	0.21	0.10	0.06	0.07
Rb	162	166	170	162	168	168	168	181	181
Sr	282	318	323	327	317	319	325	284	359
Ba	593	615	638	605	606	640	600	668	712
Y	15	17	13	16	16	16	16	14	15
Zr	146	141	139	147	143	148	128	104	151
Nb	12	12	11	13	12	12	12	11	13
Th	29	28	28	29	29	29	27	26	31
La	28	37	35	36	36	37	31	31	35
Ce	61	69	64	63	61	64	52	51	63
Sc	11	10	7	11	10	9	7	5	10
Zn	67	64	58	63	62	65	57	37	64
U	14	13	12	13	13	13	11	8	13
Co	58	49	56	92	54	33	11	10	65
Pb	26	24	24	25	24	25	26	29	19
Cu	12	13	20	17	14	9	14	10	22
Mn	450	476	427	454	471	483			
V	73	78	59	72	74	82	70	45	81
Ni	11	11	11	11	12	13	24	19	13
Cr	41	42	32	43	42	47	43	38	35

Table 8. Previous XRF major and trace element data for Chascon-Runtu Jarita. Data from Watts et al. (1999).

	Chascon - Runtu Jarita						
	Chascon CC19	Dome A CCO5	Dome B CCO9	Dome J CC23	Dome E CC27	Dome G CC30	Dome H CC33
SiO_2	70.54	64.56	74.02	73.51	76.01	69.11	68.78
TiO_2	0.45	0.64	0.27	0.28	0.16	0.51	0.54
Al_2O_3	15.29	15.83	13.25	14.12	12.90	15.54	15.75
Fe_2O_3	2.98	4.57	2.05	1.79	1.20	3.32	3.53
MnO	0.05	0.07	0.06	0.05	0.04	0.05	0.06
MgO	1.13	1.85	0.65	0.81	0.27	1.26	1.38
CaO	2.85	4.37	1.86	1.74	1.28	3.09	3.16
Na_2O	3.36	3.36	3.53	3.59	3.18	3.49	3.18
K_2O	4.48	3.56	4.48	4.89	4.90	4.33	4.25
P_2O_5	0.11	0.14	0.05	0.05	0.02	0.12	0.14
Rb	255	414	359	239	326	251	244
Sr	268	115	160	187	78	279	255
Ba	609	181	257	684	156	578	627
Y	14	44	38	20	28	16	17
Zr	151	108	116	150	96	165	156
Nb	15	29	25	16	20	16	16
Th	30	28	27	28	40	30	29
La	32	18	24	45	20	37	39
Ce	58	39	47	74	44	63	73
Sc							
Zn	57	38	40	49	31	59	54
U	13	23	21	10	20	13	10
Co							
Pb	31	40	36	30	37	28	30
Cu	4	0	1	1	0	3	4
Mn	530	642	625	559	448	573	560
V	59	27	42	18	7	61	47
Ni	2	2	2	1	2	2	2
Cr	12	7	4	5	9	14	6

Table 9. Previous XRF major and trace element data of andesitic enclaves from Chao and Chascon. Data from de Silva et al. (1994) and Watts et al. (1999).

	Chao	Chascon Runtu-Jarita		
	Chao II 88068B	Dome C CC10	Dome C CC14	Dome F CC31
SiO_2	60.31	64.13	64.32	63.20
TiO_2	0.87	0.74	0.72	0.72
Al_2O_3	17.30	16.80	16.53	16.54
Fe_2O_3	6.14	5.23	5.17	5.00
MnO	0.09	0.07	0.07	0.07
MgO	3.76	2.15	2.11	1.99
CaO	5.83	4.75	4.82	4.68
Na_2O	3.09	3.44	3.47	3.45
K_2O	2.39	3.51	3.54	3.46
P_2O_5	0.23	0.17	0.17	0.17
Rb	78	179	182	176
Sr	493	387	387	397
Ba	678	635	608	657
Y	20	21	23	21
Zr	185	185	182	192
Nb	11	14	14	14
Th	12	16	18	16
La	31	38	39	37
Ce	59	75	68	80
Sc	17			
Zn	95	72	74	74
U	4	6	6	6
Co	91			
Pb	16	22	22	22
Cu	11	6	6	8
Mn	670	752	754	753
V	16	117	119	125
Ni	18	2	3	1
Cr	100	10	10	11

5.2.2 This Study

XRF for this study was conducted at Washington State University, using the standard single bead low-dilution fusion technique, detailed in Johnson et al. (1999). 100g of each

sample was crushed and powdered using a jaw crusher and tungsten-carbide puck-mill. For XRF analyses, 3.5 g of powdered sample was added to 7 g of 'spectromelt' [dilithium tetraborate ($Li_2B_4O_7$)] powder; extreme care was taken to ensure correct weights to within 0.005g of target. The powders were shaken extensively to ensure homogeneity and static electricity was removed using a neutralizing strip. The powder was then carefully dumped into a clean graphite crucible. Crucibles were placed in a 1000°C muffle furnace for roughly 50 minutes to fuse material in beads, and then allowed to cool. Once cooled, the beads were removed, cleaned, and then re-powdered using the tungsten-carbide puck mill. The resulting powder was then once again placed in crucibles and put in the furnace for another 50 min to fuse the material into beads. Once cooled, the beads were engraved with the relevant sample number and polished. Finally, the beads were analyzed on the ThermoARL Advant'XP+ sequential X-ray fluorescence spectrometer for 10 major elements and 21 trace elements. The unknown sample is compared to the results from nine USGS standard samples: PCC-1, BCR-1, BIR-1, DNC-1, W-2, AGV-1, GSP-1, G-2, and STM -1 along with two beads of pure quartz used as blanks for all elements except Si.

ICP-MS for this study was also conducted at Washington State University. ICP-MS sample prep differed slightly from that of XRF in that equal 2g amounts of sample and spectromelt were mixed and only fused into beads once. These beads were then re-powdered and left as such, rather than fusing them a second time. The powder was then transferred to the WSU staff for acid dissolution using the Knaack et al. (1994) method. Finally, the powders were analyzed using the Agilent 7700 ICP-MS, measuring for 27 trace elements.

XRF and ICP-MS analysis were conducted on all of the collected samples from four of the five primary domes (excluding Chascon); this includes silicic lava, mafic enclaves and any other additional samples. These data are summarized in Table 10 and Table 11.

Table 10. New XRF major and trace element for Chao, Chillahuita, Tocopuri and Chanka conducted for this study at Washington State University GeoAnalytical Laboratory. Major element analyses normalized to 100 % volatile-free composition

	Chanka		Chao			Chillahuita	Tocopuri	
	Primary	Mafic	Primary Lava	Crystal Rich Lava	Pyroclastic Deposit	Primary Lava	Primary Lava (L)	Primary Lava (D)
	09001CT	09002CT	09003CT	09005CT	09006CT	09009CT	09011CT	09012CT
SiO_2	66.61	60.91	68.29	68.61	67.55	68.82	71.96	71.74
TiO_2	0.54	0.86	0.47	0.49	0.49	0.47	0.36	0.36
Al_2O_3	15.96	16.48	15.70	15.27	15.81	15.24	14.50	14.62
FeO*	3.74	5.74	3.19	3.23	3.35	3.09	2.18	2.21
MnO	0.07	0.09	0.06	0.06	0.06	0.06	0.05	0.05
MgO	1.86	3.59	1.53	1.60	1.71	1.56	0.94	0.96
CaO	3.82	6.04	3.52	3.39	3.84	3.43	2.54	2.61
Na_2O	3.69	3.71	3.38	3.41	3.45	3.40	3.30	3.35
K_2O	3.56	2.37	3.74	3.81	3.61	3.82	4.09	4.02
P_2O_5	0.15	0.22	0.12	0.12	0.13	0.12	0.08	0.08
Rb	166	73	164	173	158	167	179	175
Sr	402	560	331	317	348	326	280	292
Ba	693	751	586	595	581	615	661	663
Y	15	17	14	15	15	15	13	12
Zr	154	160	141	149	138	147	119	124
Nb	12	9	10	11	11	10	11	10
Th	30	8	30	30	28	29	27	27
La	33	28	34	36	36	35	33	33
Ce	60	50	60	65	65	63	57	64
Sc	9	15	8	8	9	8	5	6
Zn	66	94	64	66	66	64	46	48
U	11	4	12	9	9	12	9	9
Co								
Pb	20	12	25	26	25	25	29	29
Cu	18	17	11	7	23	7	5	4
Mn								
V	86	140	74	75	78	71	48	49
Ni	4	14	5	6	8	6	3	4
Cr	35	91	29	35	40	34	15	14

Table 11. New ICP-MS trace element data for Chao, Chillahuita, Tocopuri and Chanka conducted for this study at Washington State University GeoAnalytical Laboratory..

	Chanka		Chao			Chillahuita	Tocopuri	
	Primary	Mafic	Primary Lava	Crystal Rich Lava	Pyroclastic Deposit	Primary Lava	Primary Lava (L)	Primary Lava (D)
	09001CT	09002CT	09003CT	09005CT	09006CT	09009CT	09011CT	09012CT
La	33.21	27.38	34.57	34.32	35.12	34.33	33.49	35.16
Ce	62.17	54.77	65.27	64.70	65.69	63.16	60.85	62.63
Pr	6.82	6.65	7.15	7.08	7.12	7.16	6.67	6.78
Nd	23.73	25.63	24.62	24.26	24.44	24.87	22.25	22.39
Sm	4.37	5.24	4.48	4.41	4.45	4.48	3.90	3.75
Eu	0.93	1.26	0.91	0.91	0.91	0.89	0.76	0.76
Gd	3.46	4.37	3.43	3.42	3.43	3.39	2.91	2.79
Tb	0.51	0.62	0.50	0.51	0.51	0.50	0.44	0.41
Dy	2.89	3.43	2.78	2.82	2.84	2.76	2.44	2.33
Ho	0.55	0.63	0.52	0.54	0.54	0.53	0.48	0.44
Er	1.46	1.59	1.40	1.43	1.44	1.41	1.28	1.18
Tm	0.22	0.23	0.21	0.22	0.22	0.21	0.19	0.18
Yb	1.38	1.34	1.37	1.39	1.39	1.36	1.24	1.19
Lu	0.20	0.19	0.21	0.21	0.21	0.22	0.21	0.19
Ba	694.44	755.02	599.42	604.23	586.38	616.39	670.90	671.27
Th	29.49	8.83	29.72	29.83	27.98	29.67	27.67	26.92
Nb	11.00	8.79	10.48	10.67	10.17	10.33	10.03	9.78
Yb	14.76	16.38	14.65	14.74	14.95	14.13	12.86	12.20
Hf	4.36	4.20	4.53	4.32	4.25	4.30	3.79	3.56
Ta	1.33	0.68	1.39	1.40	1.28	1.34	1.39	1.32
U	9.45	2.65	10.90	11.04	9.83	10.64	8.87	8.45
Pb	18.90	11.84	26.10	25.55	24.33	26.06	27.93	27.52
Rb	161.11	70.76	161.96	170.91	156.95	162.79	177.28	173.01
Cs	12.60	3.25	13.97	14.56	12.75	13.91	11.68	11.27
Sr	405.40	563.66	335.71	320.55	353.89	321.59	278.51	289.59
Sc	8.77	14.42	7.05	7.31	7.71	7.15	5.13	4.98
Zr	145.37	154.91	140.94	138.60	136.63	134.70	117.78	109.34

Chanka is the least silicic dome with 66.6% SiO_2 and Tocopuri as the most silicic with 71.7% SiO2. Chao and Chillahuita are nearly identical at 68.3% and 68.8% SiO_2, respectively. Of the major oxides, K_2O parallels the SiO_2 trend while TiO_2, Al_2O_3, FeO*, MnO, MgO, CaO, Na_2O_3, and P_2O_5 show the inverse of the SiO_2 trend with Chanka having the highest values and Tocopuri the lowest. Additionally, a mafic

enclave from Chanka was analyzed and found to be of andesitic composition at 60.9% SiO_2.

With the exception of the Chanka mafic enclave, all the lavas plot as high-K and dacites to rhyolites (Figure 13). Furthermore, all plot in the calc-alkaline field on an AFM diagram, according to both Kuno (1968) and Irvine and Baragar (1971) classifications (Figure 12).

Within the silicic lava, trace element concentrations vary little. The silicic and mafic lavas from the domes are all LREE enriched (Figure 14), with Ce/Yb rations of 45 to 52, while the mafic enclaves are slightly more enriched in HREE. Variation diagrams (Figure 15) show that the silicic lava from these domes form a consistent group, while the mafic enclaves share a general grouping. The trends revealed in four of the diagrams (Sr, Ba, Y, and Zr) suggest that mixing between silicic and mafic is responsible for a large part of the variations seen in these trace elements. However, Th and U show an apparent change in trend, possibly reflecting the onset of zircon or allanite crystallization and attesting that some fractional crystallization may also be affecting the magmas.

Additional to the domes, fields for APVC and CVZ arc volcanics are shown in the diagrams. These fields show a general overlap, and in most cases, andesites from the domes and APVC overlap with CVZ arc. However, a plot of Sr/Y vs Y (Figure 16) helps to illustrate the differences between the composition and evolution of andesites and dacites from the APVC vs. the CVZ arc.

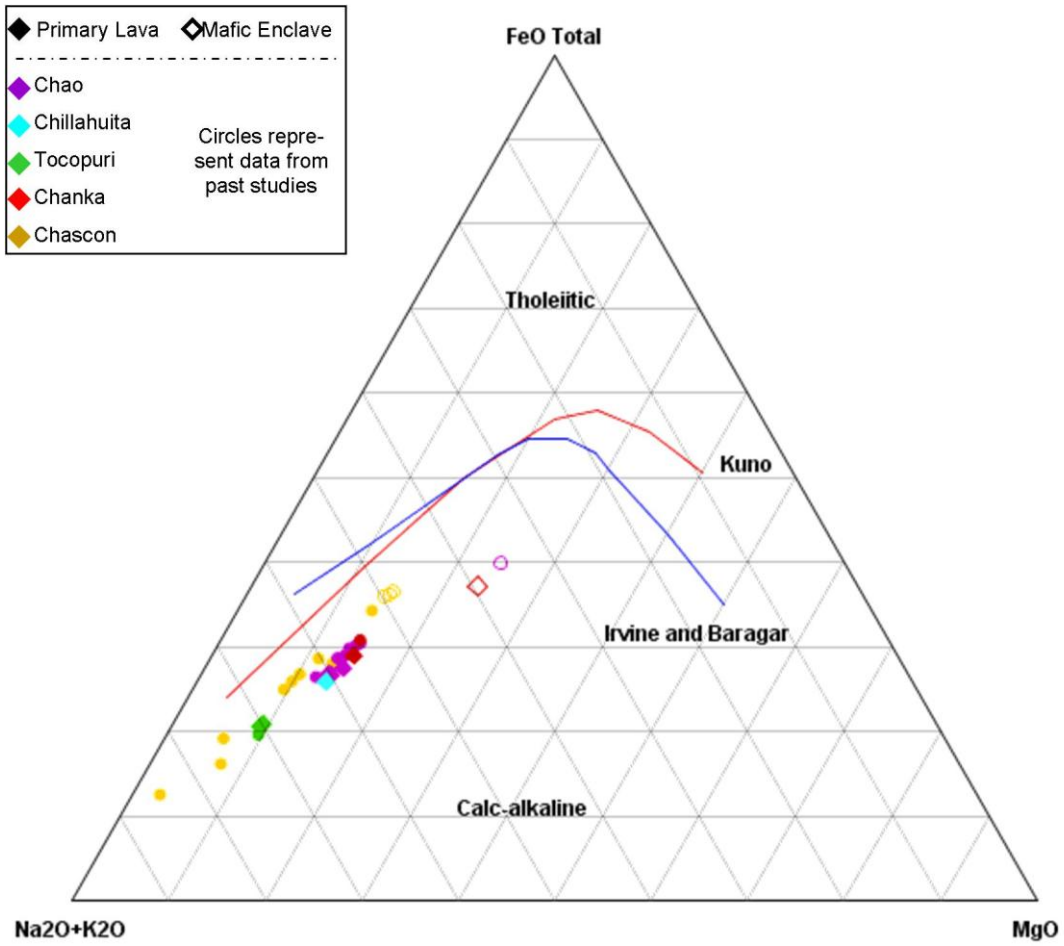

Figure 12. AFM diagram for the five primary domes. . Diamonds are data from this study while circles are from past studies. Solid symbol represents silicic lava where as open symbol represents mafic enclaves. Lines represent the upper limit of the Calc-Alkaline series defined by Kuno (1968) and Irvine and Baragar (1971).

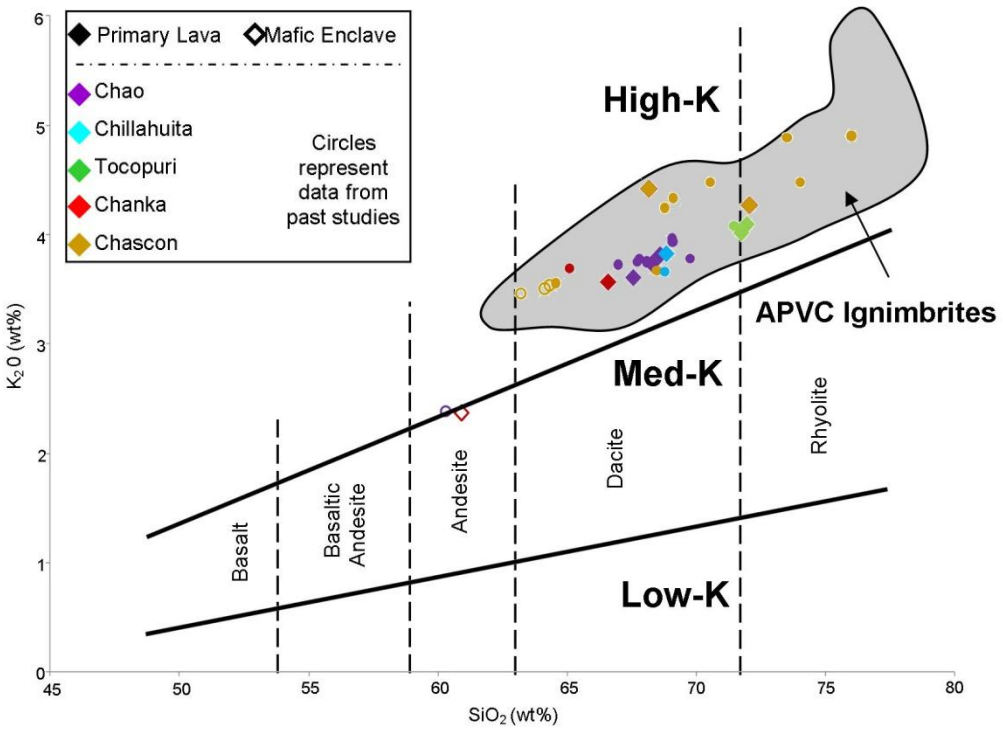

Figure 13. SiO_2 vs. K_2O diagram (Peccerillo and Taylor, 1976) of XRF data for five primary domes. Colored diamonds are data from this study (including Chascon data from de Silva et al., 1994); circles are from past studies. Solid symbol represents silicic lava where as open symbol represent mafic enclaves. Compositions of APVC ignimbrites are shown by gray field modified from de Silva and Gosnold (2007).

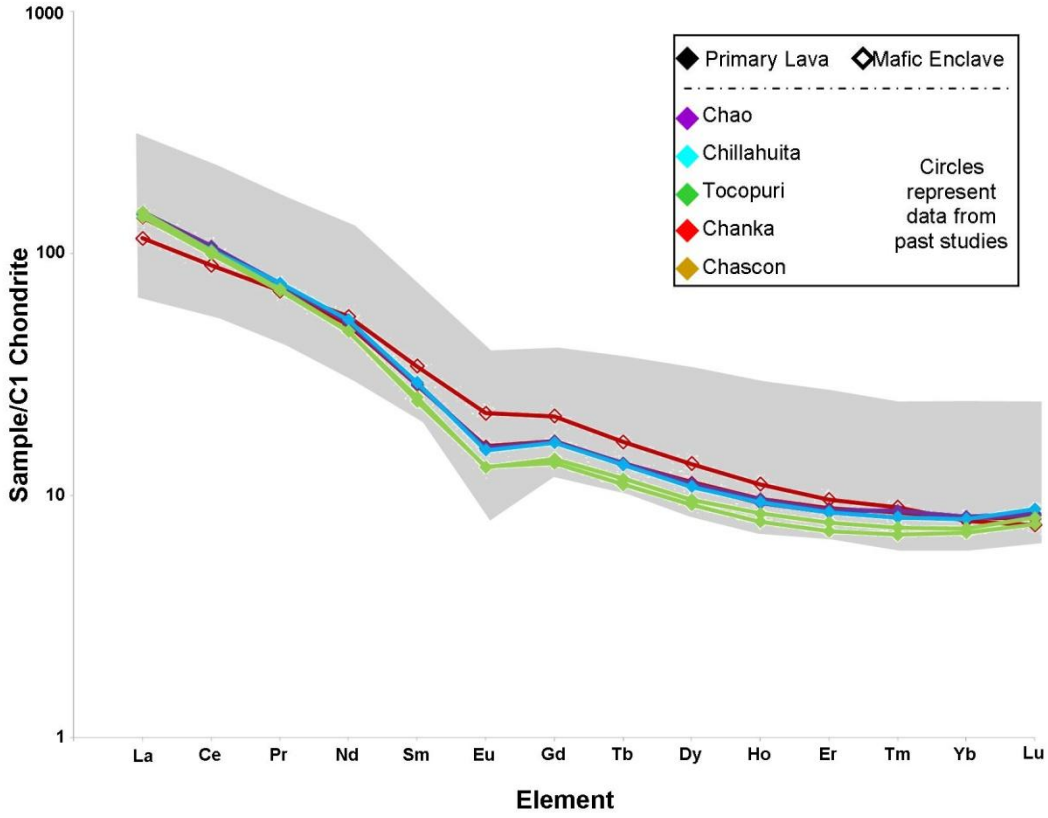

Figure 14. C1 chondrite (Sun and McDonough, 1989) normalized spider diagram of REE from domes of this study, including the Chanka mafic enclave. Symbols and colors for domes as in Figure 12. APVC REE are represented by the gray field. Many of the REE patterns from the domes are overlapping. The Chanka mafic enclave plots as the highest of all the dome lavas on the diagram.

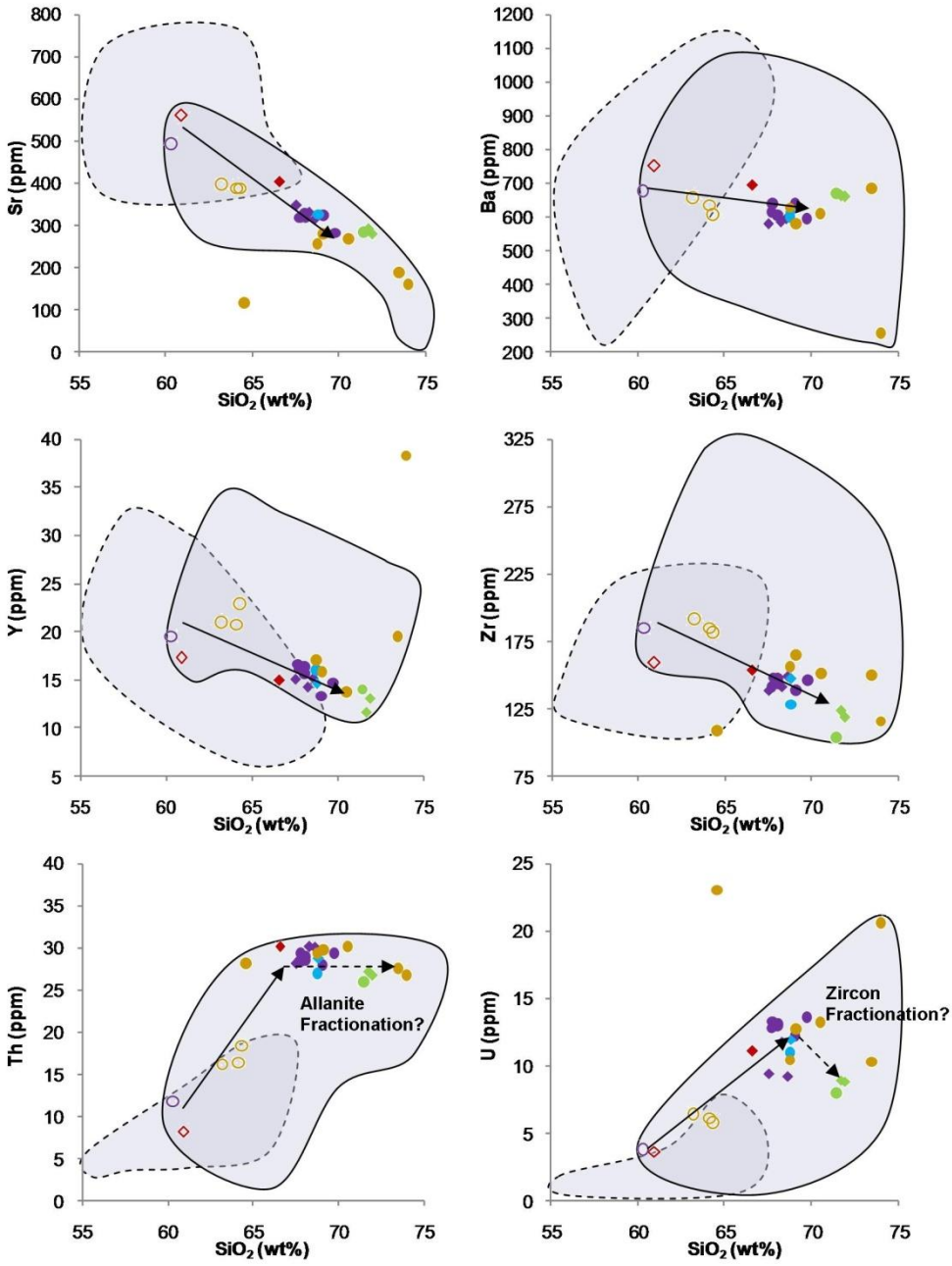

Figure 15. Trace element variation diagrams of primary silicic and mafic lavas from all five domes of this study. Key as in Figure 14. Data from this study, de Silva et al. (1994) and Watts et al. (1999). Gray, solid bordered field represents APVC concentrations while the gray dashed border field represents CVZ stratovolcanoes. Solid arrow represents inferred mixing path between silicic and mafic components. Dashed arrow represent potential trace element fractionation,

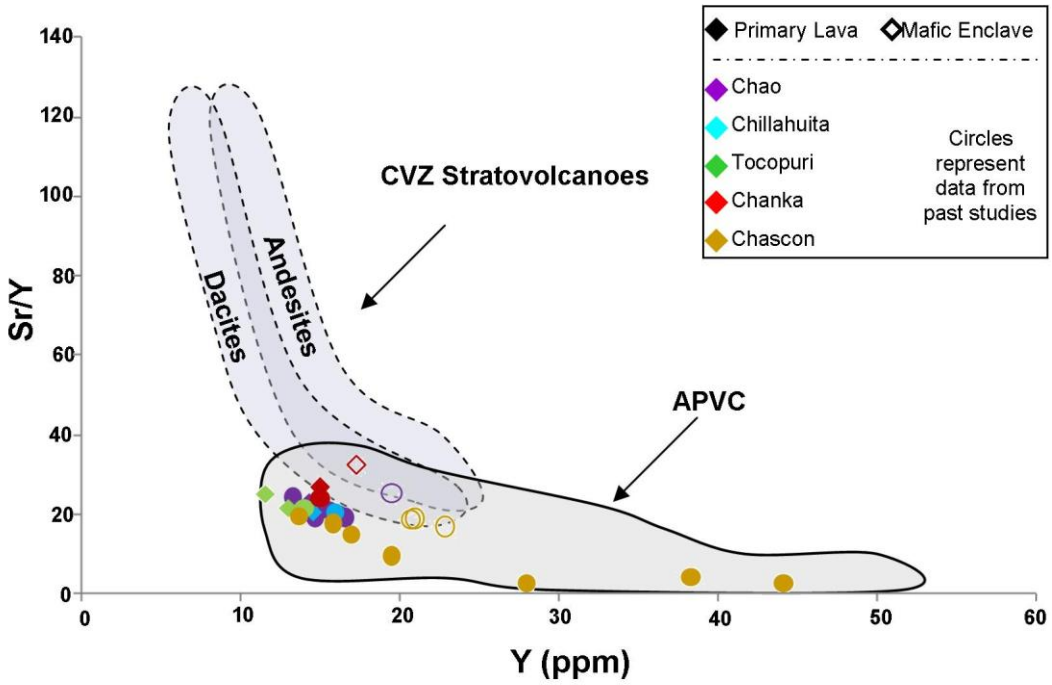

Figure 16. Sr/Y vs Y diagram illustrating that differences, while subtle, do exist between lavas from APVC and lavas from the CVZ stratovolcanoes. Domes from this study are shown represented as in Figure 12. APVC is represented by the solid-boundary field while arc stratovolcanoes are represented the dashed boundary field.

5.2.3 Summary

The whole-rock XRF and ICP-MS data on the four domes analyzed for this study are largely consistent with data on the domes from past studies (e.g. de Silva et al., 1994; Watts et al., 1999), showing a similar range in nearly all major and trace elements. Additionally, while Chascon lavas were not analyzed during the present study, XRF and ICP-MS data from the other four domes are consistent with has been found previously for Chascon (Watts et al., 1999; de Silva et al., 1994). Data on mafic enclave lavas is also consistent with previous studies as the Chanka mafic enclave data from this study are very near previously analyzed mafic enclaves from both Chao and Chascon.

The whole-rock major element data on the five domes, both from this study and past, show a close similarity between the domes, with all dome lavas plotting as high-K dacites to rhyodacites (Figure 13). Furthermore, the major element data from these domes are also consistent with past APVC ignimbrites and lavas as a whole. To illustrate this point, data from APVC ignimbrite are shown in the gray field on Figure 13. The major element data on silicic lavas from domes of this study, in addition to past studies (de Silva et al., 1994; Watts et al., 1999), all plots within this APVC ignimbrite field. This correlation in whole-rock major element chemistry between the domes and the ignimbrites supports that the magmas that eventually formed the domes are of nearly the same composition as the ignimbrites which define the region.

The trace element data on the silicic domes shows that they are all LREE enriched with Ce/Yb ratios restricted from 45 to 52 and have minimal variation in the other trace elements. These data support findings and suggestions from previous studies (e.g. de Silva et al., 1994; Watts et al., 1999) that the five primary domes of this study are strikingly similar to each other in chemical characteristics. Furthermore, similar to major elements, previous trace element data from APVC ignimbrites shows a broad similarity to the results from these domes, as the domes fall within the overall APVC trace element range (Figure 14). Trace element variation diagrams show that the silicic and mafic lavas are grouped and some mixing has occurred between these groups. Furthermore, the plot of Sr/Y vs Y helps illustrate further the difference between arc and APVC magmas and additionally the mafic injection that occurs in these domes is likely of APVC origin.

5.3 Geothermometry and Geobarometry

5.3.1 Previous work

de Silva et al. (1994) conducted Fe-Ti oxide temperature analysis on Chao (Table 12). The temperatures from Chao, calculated by two different models, indicated little

variation in temperatures and oxygen fugacity throughout the magma at ~840°C and 10^{-11}, respectively. In addition to Fe-Ti oxide analysis, de Silva (unpublished data) also examined amphibole crystal rims and cores present within Chao lavas, these data were analyzed further by this study to serve as a barometer of the lavas (Table 16).

Table 12. Representative magnetite and ilmenite compositions with respective temperature and log fO_2 estimates for Chao from de Silva et al. (1994)

	Phase 1		Phase 2		Phase 3	
	Mag	Ilm	Mag	Ilm	Mag	Ilm
SiO_2	0.06	0.02	0.00	0.00	0.00	0.00
TiO_2	4.30	34.19	4.88	35.72	4.56	34.67
Al_2O_3	1.11	0.23	1.56	0.41	1.40	0.14
FeO	84.47	60.81	85.35	58.01	85.89	57.52
MnO	0.54	0.41	0.56	0.85	0.52	0.71
MgO	0.60	0.58	0.69	1.29	0.86	1.37
CaO	0.10	0.15	0.07	0.05	0.04	0.04
NaO	0.12					
Subtotal	91.30	96.39	93.11	96.33	93.27	94.42
FeO*	32.78	29.32	33.84	28.96	33.38	28.07
Fe_2O_3*	57.44	35.00	57.25	32.28	58.35	32.73
Total	97.06	99.90	98.85	99.56	99.12	97.70
log (Mg/Mn)	0.29	0.40	0.34	0.43	0.46	0.52
X(usp)^	0.13		0.15		0.14	
X(ilm)^		0.66		0.68		0.67
T°C¶	826		832		827	
log fO_2	-11.2		-11.2		-11.3	

* Calculated assuming charge-balanced stoichiometric formula
^ Calculated following Stormer (1983)
¶ Calculated following Anderson and Lindsley (1985)

Watts et al. (1999) conducted Fe-Ti oxide temperature analysis on Chascon-Runtu Jarita silicic and mafic lavas (Table 13). Using the model developed by Anderson and Lindsley (1988) temperatures for the silicic magmas ranged from 630°C to 680°C and log fO_2 for these magmas ranged from -16.17 to 16.80. For the mafic magmas, the

temperatures ranged from 926°C to 964°C and the log fO_2 for these magmas ranged from -9.8 to -10.3. Additionally, a co-existing pair of Fe-Ti oxides included within a sanidine xenocryst found in the mafic lava gave a temperature of 680°C and a log fO_2 of -15.8. In addition to Fe-Ti oxides, Watts et al. (1999) also conducted EMPA analysis of various other mineral phases in the CRJ lavas including amphibole. These amphibole data were used by this study to serve as a barometer and are presented in Table 17.

Table 13. Representative magnetite and ilmenite compositions with respective temperature and log fO_2 estimates for Chascon-Runtu Jarita silicic and mafic lavas from Watts et al. (1999).

	Mafic Lava				Silicic Lava					
	CC13	CC13	CC06	CC06	CC14	CC14	CC14	CC14	CC04	CC04
	Mag	Ilm	Mag	Ilm	Mag	Ilm	Mag	Ilm	Mag	Ilm
SiO_2	0.06	0.02	0.06	0.04	0.10	0.03	0.04	0.02	0.34	0.00
TiO_2	10.80	36.85	10.12	38.01	10.07	38.64	4.30	47.54	4.12	47.36
Al_2O_3	1.30	0.55	3.58	0.55	3.67	0.44	1.07	0.08	1.17	0.02
FeO*	38.76	27.86	44.21	32.54	35.95	29.42	33.03	37.95	31.68	37.83
Fe_2O_3*	46.35	30.22	36.66	21.65	45.63	26.32	58.30	8.54	53.82	7.74
MnO	0.44	0.34	0.34	0.39	0.42	0.39	1.29	3.41	0.60	3.26
MgO	1.20	2.65	2.80	2.42	2.85	2.80	0.27	0.77	0.55	0.81
CaO	0.03	0.00	0.01	0.03	0.01	0.02	0.00	0.01	0.12	0.01
Total	98.93	98.22	97.61	96.61	98.71	98.08	98.29	98.31	92.39	97.04
log(Mg/Mn)	0.69	1.14	0.91	0.82	1.08	1.10	-0.44	-0.40	0.21	-0.36
X(usp)^	0.32		0.31		0.31		0.13		0.13	
X(ilm)^		0.69		0.72		0.73		0.91		0.92
T°C¶	956		964		926		683		677	
log fO_2	-9.8		-9.9		-10.3		-15.8		-16.2	

* Calculated assuming charge-based stoichiometric formula

^ Calculated following Stormer (1983)

¶ Calculated using Andersen and Lindsley (1988)

5.3.2 Determining Intensive Parameters

EPMA analysis of the composition of Fe-Ti oxides found in each dome allow for the estimation of the magmatic conditions just prior to eruption. Previous studies have investigated these conditions on Chao and Chascon-Runtu Jarita.

Electron microprobe analyses (EMPA) of Fe-Ti oxides were performed at Oregon State University using a CAMECA SX-100 microprobe. The instrument is equipped with one energy dispersive spectrometer (EDS) and five wavelength dispersive spectrometers (WDS). Magnetite and ilmenite were analyzed using 15 keV accelerating voltage and a 30 nA current with a 1μm beam diameter. Element standards, with peak counting times in parentheses, include Si and Ca in KAUG-Kakanui augite (10 s), Al in GAHN-gahnite (20 s), Mg and Cr in CROM-chromite (10 s and 20 s), Ti in ILMN-ilmenite (10 s), Fe in MAGT-magnetite (10 s), V in VANA-vanadanite (20 s), and Mn in PYMN (20 s). Data reduction was performed using a stoichiometric PAP correction model from Pouchou and Pichoir (1985).

Thin sections of the dominant silicic lava were polished and analyzed for Chao, Chillahuita, Tocopuri, and Chanka. Given the paucity of ilmenite relative to magnetite in these lavas, mounts of 0.25 Amp magnetic crystal separates were also created for all five domes, allowing for a higher concentration of Fe-Ti Oxides (specifically ilmenite) than in the thin sections. Within the thin sections, touching magnetite-ilmenite pairs were desired and were found to be relatively abundant within Chao and Chillahuita, but were limited or nonexistent in Tocopuri and Chanka. Unpaired crystals were analyzed when the pairs were exhausted or could not be found. Included crystals or pairs were avoided whenever possible, with the excepting of one such pair in Chanka. Within the mounts, despite the use of the 0.25 Amp separates, ilmenite was found to

be nearly as sparse as in the thin sections and was severely limited in the Tocopuri and Chascon mounts.

After the completion of EMPA analysis the compositions of unpaired oxides were compared with paired oxides to ensure coherence and analyses beyond the range defined by paired oxides were eliminated.

Equilibrium compositions all magnetite-ilmenite pairs were checked using the criteria of Bacon and Hirschmann (1988) Following these checks, the pairs that were in equilibrium were used in models by Anderson and Lindsley (1988) and Ghiorso and Evans (2008) to estimates the temperature and oxygen fugacity (fO_2) of each lava. Paired Fe-Ti oxides were run against each other, and then all unpaired magnetite and ilmenite from a given thin section or mount were run against each other. The pairs were furthermore used as "standards" to check that the unpaired results were reasonable.

5.3.3 Fe-Ti Oxide Geothermometry Results

Representative microprobe analyses of magnetite and ilmenite from each dome are listed in Table 14 while Table 15 represents a summary of the Fe-Ti Oxide analyses and temperature/oxygen fugacity results.

20 to 25 analyses were conducted on thin sections of the four Chilean domes. In Chao and Chillahuita these analyses are split evenly between magnetite and ilmenite. However, in Tocopuri and Chanka, where a relative paucity of ilmenite exists, only about five ilmenite analyses were conducted. Pairs were sought due to a higher likelihood they would be in equilibrium and 5-7 pairs were found in Chao and Chillahuita, while Chanka and Tocopuri had none.

Mounts were created from all of the domes and 10 to 25 analyses were taken. The ratio of magnetite to ilmenite mirrored that of the thin sections for the four Chilean domes while Chascon displayed a relative lack in ilmenite.

In both the thin sections and mounts the vast majority of the analyzed crystals were glass hosted. When all magnetite and ilmenite combinations were checked for equilibrium via the Hirschmann and Bacon (1988) method, the amount from each dome in equilibrium varied. In Chao, Chillahuita and Chanka, 45-60 combinations were found to be in equilibrium, while in Tocopuri and Chascon <10 passing combinations were found.

Combing the results from both the thin section and sample mount, under the Ghiorso and Evans (2010) model, the temperature ranges seen in all of the domes were roughly concordant and overall ranged from 699 to 903 with the average from each dome ranging from 750°C to 792°C. Oxygen fugacities ($\log_{10}fO_2$ relative to NNO) ranged from 0.82 to 1.57 with the average from the domes range from 1.29 to 1.46. Examining the data further reveals high standard deviations for the temperature and oxygen fugacity for nearly every dome. These relatively high standard deviations are the result of distinct temperature populations for each dome. For example, Chillahuita has one population which ranges from 702°C to 751°C and another population with ranges from 851°C to 903°C. This two temperature population pattern is seen consistently throughout the domes and, in general, the lower temperature population is in the lower to mid 700s and higher is in the mid 800s.

The amount of magnetite-ilmenite combinations in disequilibrium and the multiple temperature populations from the Fe-Ti oxides indicate that mixing between silicic and mafic magmas may be taking place and the Fe-Ti oxides that show higher temperatures have mixed into a lower temperature silicic magma which is represented by the lower temperature population.

The results from the Anderson and Lindsley (1988) model parallel the results from the Ghiorso and Evans (2010), however, A&L 1988 results were found to give uniformly higher temperatures. The average temperature difference between the two models was around 65°C, with discrepancies as large as 90°C. Given that Ghiorso and Evans

(2008) is the newest and presumably most accurate model, it is taken that the temperature value from Anderson and Lindsley (1988) represents a maximum.

Table 14. Representative Fe–Ti oxide compositions and calculations of equilibration temperatures.

Dome	Chao		Chillahuita		Tocopuri		Chanka		Chascon	
Sample	09003CT		09009CT		09011CT		09001CT		JFKBOL10-001	
	Mag	Ilm	Mag	Ilm	Mag	Ilm	Mag	Ilm	Mag	Ilm
SiO2	0.07	0.03	0.00	0.00	0.03	0.06	0.07	0.07	0.05	0.04
TiO2	4.82	35.24	4.89	35.82	5.39	36.64	5.22	37.38	6.19	35.69
Al2O3	1.53	0.19	1.47	0.19	1.11	0.22	1.74	0.26	1.21	0.24
V2O3	0.52	0.39	0.61	0.31	0.48	0.30	0.49	0.25	0.40	0.44
Cr2O3	0.20	0.07	0.22	0.06	0.19	0.04	0.09	0.04	0.11	0.04
FeO	83.37	58.50	83.37	57.92	83.60	55.18	82.89	57.33	83.16	55.91
MnO	0.57	0.56	0.55	0.54	0.65	1.04	0.46	0.59	0.60	0.46
MgO	0.92	1.40	0.93	1.52	0.80	1.31	1.22	1.81	0.40	0.62
CaO	0.02	0.07	0.01	0.03	0.03	0.16	0.09	0.01	-0.01	0.02
NiO	0.08	0.00	0.06	0.02	0.00	0.00	0.03	0.02	0.03	0.00
Subtotal	92.10	96.41	92.11	96.41	92.24	94.90	92.30	97.78	92.14	93.47
Calculated assuming charge balanced stoichiometric formula (Stormer, 1983)										
FeO	33.10	28.69	33.08	28.94	33.75	29.68	33.23	29.85	35.06	30.56
Fe2O3	55.86	33.14	55.88	32.21	55.40	28.34	55.18	30.54	53.46	28.18
Total	97.69	99.73	97.71	99.64	97.79	97.74	97.83	100.84	97.50	96.29
log (Mg/Mn)	0.45	0.64	0.47	0.69	0.33	0.35	0.67	0.73	0.06	0.37
X(usp)										
X(ilm)	0.15		0.15		0.16		0.16		0.19	
		0.67		0.68		0.71		0.70		0.71
Calculated following Anderson and Lindsley (1988)										
T°C	835		834		835		836		850	
log *fO2*	-11.18		-11.22		-11.33		-11.27		-11.18	
Calculated following Ghiorso and Evans (2008)										
T °C (Fe-Ti exchange)	752		755		767		771		793	
$\log_{10} f_{O2}$ (relative to NNO)	1.51		1.50		1.38		1.47		1.27	

Table 15. Summary of Fe-Ti oxide temperature/oxygen fugacity results for each domes using Ghiorso and Evans (2010) and Anderson and Lindsley (1988) models.

	Chao		Chillahuita		Tocopuri		Chanka		Chascon
	Thin Section	Sample Mount	Thin Section	Sample Mount	Thin Section	Sample Mount	Thin Section	Sample Mount	Sample Mount
Analyses (mag/ilm)	25 (13/12)	25 (12/13)	25 (12/13)	25 (13/12)	20 (15/5)	10 (7/3)	20 (15/5)	10 (7/3)	12 (9/3)
Pairs	5	-	7	-	0	-	2	-	-
Combinations in Equilibrium	16	32	10	44	4	1	42	21	9
Ghiorso and Evans (2010)									
Temperature (°C)									
Range	748-793	699-843	714-836	702-903	732-769	872	761-837	735-847	735-843
Average	771	778	768	762	750	-	785	777	792
STDV	20	46	35	69	21	-	23	36	43
Oxygen Fugacity ($log_{10}fO_2$ (relative to NNO))									
Range	1.41-1.52	1.03-1.53	1.27-1.54	0.82-1.57	1.38-1.48	1.29	1.25-1.49	1.13-1.51	1.14-1.46
Average	1.46	1.37	1.42	1.36	1.43	-	1.41	1.39	1.29
STDV	0.05	0.13	0.1	0.2	0.06	-	0.06	0.11	0.14
Anderson and Lindsley (1988)									
Temperature (°C)									
Range	834-856	793-871	800-872	793-908	820-838	908	829-866	810-871	825-878
Average	844	840	831	830	828	-	841	834	852
STDV	10	25	21	38	9	-	10	17	20
Oxygen Fugacity (log $f(O_2)$)									
Range (negative)	11.2-10.9	12.1-10.7	12.0-10.8	12.3-10.4	11.5-11.3	-10.1	11.4-10.9	11.8-10.9	11-4-10.8
Average	-11.1	-11.2	-11.4	-11.5	11.4	-	-11.2	-11.4	-11.1
STDV	0.12	0.46	0.4	0.63	0.11	-	0.12	0.27	0.23

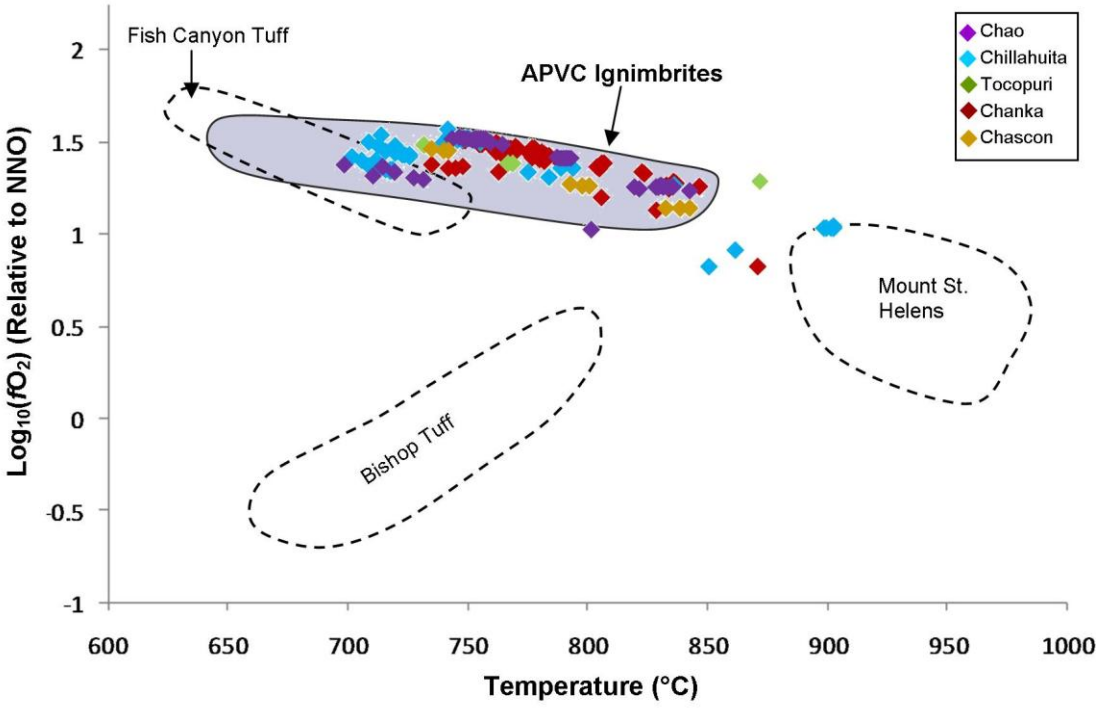

Figure 17. Temperature vs oxygen fugacity. Temperatures and oxygen fugacity based on Ghiroso and Evans (2008). Colored diamonds represent data from this study while data from APVC ignimbrites and lavas are shown by gray field. Other prominent silicic systems are shown by dashed fields. Figure modified from Dietterich and de Silva (2010) with additional data coming from Evans and Scaillet (1997).

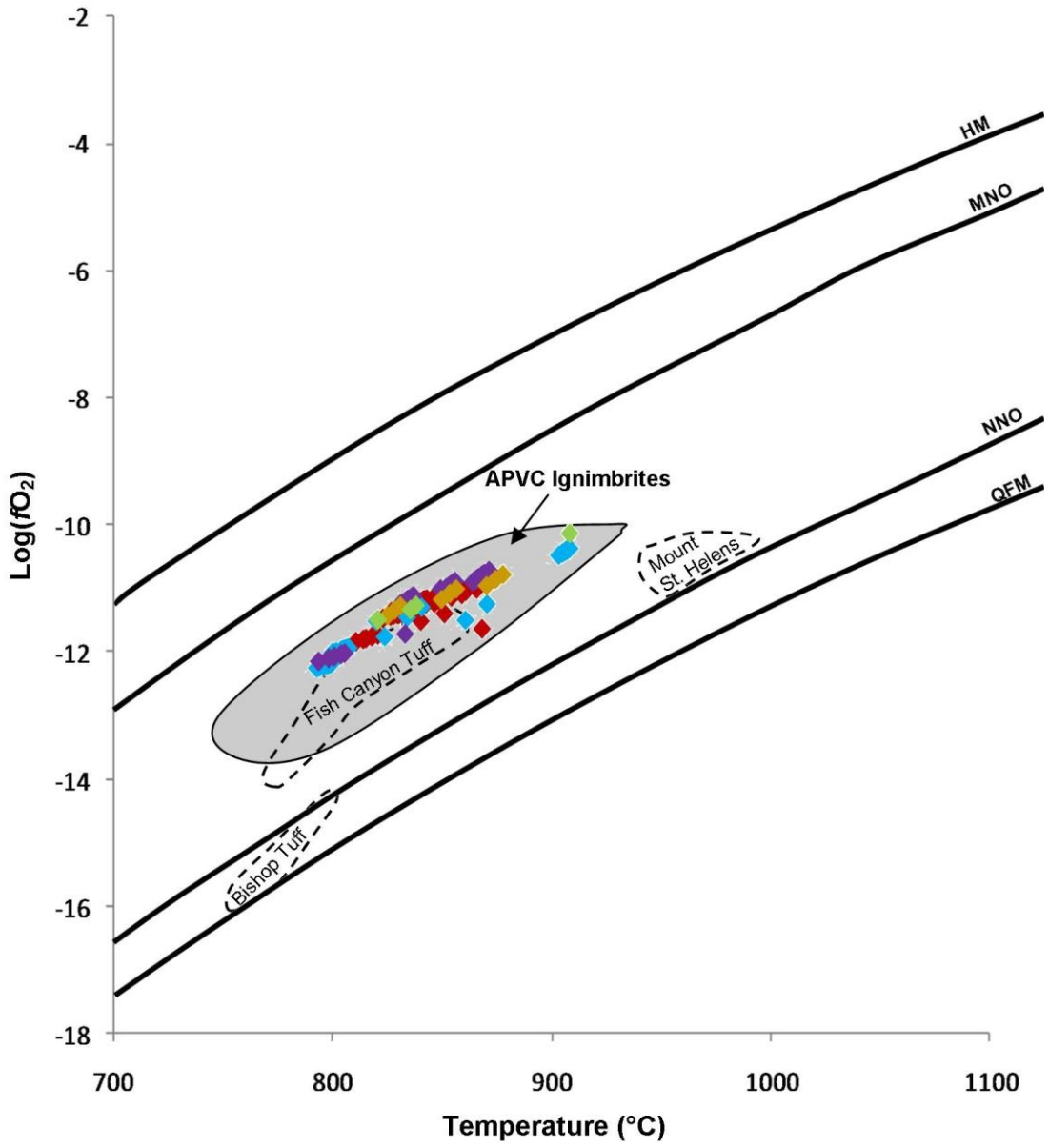

Figure 18. Temperature vs oxygen Fugacity. Temperatures and oxygen fugacity based on Anderson and Lindsley (1988). Colored diamonds represent data from this study while data from APVC ignimbrites and lavas are shown by gray field (de Silva, 1987). Other prominent silicic systems are shown by dashed fields. Buffer curves are represented by solid lines: HM, hematite-magnetite; MNO, MnO-Mn_3O_4; NNO, Ni-NiO; QFM, quartz-fayalite-magnetite.

5.3.4 Amphibole Geobarometry Results

In addition to Fe-Ti oxide thermometry, amphibole data from previous studies were used to calculate certain physical-chemical conditions of the magma prior to eruption. Pressure, temperature oxygen fugacity, and H_2O content was calculated for Chao and Chascon-Runtu Jarita using these amphibole data and the Ridolfi et al. (2010) model.

The results are summarized in Table 16 and Table 17. For Chao, the temperature calculated from the amphibole ranged from 810°C to 869°C in the amphibole rims and 820°C to 911°C in the amphibole cores. While pressure ranged from 107 to 185 MPa in the rims and 132 to 291 in the cores. For Chascon, temperatures from amphiboles from Chascon-Runtu Jarita ranged from 823°C to 878°C in the silicic lavas and 827°C to 951°C in the mafic lavas. Pressures ranged from 134 to 224 MPa in the silicic lavas and 142 to 312 MPa.

Table 16. Chao amphibole data from de Silva (unpublished) with physical-chemical conditions calculated using Ridolfi et al., (2010).

	Crystal Rims								Crystal Cores			
	Chao 1	Chao 1	Chao 1	Chao 1	Chao 4	Chao 4	Chao 4	Chao 4	Chao 4	Chao 4	Chao 4	Chao 4
SiO_2	46.54	46.78	45.79	46.70	46.59	44.30	44.77	45.34	46.18	42.69	42.28	45.11
TiO_2	1.33	1.15	1.31	1.20	1.61	1.88	1.53	1.17	1.46	2.51	2.37	1.53
Al_2O_3	7.15	7.00	7.79	6.87	7.33	9.02	8.91	7.81	7.70	10.77	10.71	7.77
Cr_2O_3												
FeO	13.95	13.47	14.77	13.42	14.68	13.03	14.40	14.59	14.18	15.76	15.86	14.99
MnO	0.41	0.39	0.33	0.36	0.38	0.30	0.35	0.39	0.35	0.38	0.35	0.47
MgO	13.74	13.78	12.83	14.09	12.92	13.60	12.48	12.82	13.11	11.47	11.13	12.50
CaO	11.97	11.82	12.04	11.88	11.43	11.14	11.40	11.44	11.41	10.52	11.35	11.39
Na_2O	1.49	1.47	1.55	1.46	1.23	1.55	1.38	1.22	1.23	1.81	1.78	1.25
K_2O	0.72	0.72	0.83	0.66	0.78	0.67	0.87	0.83	0.78	0.93	0.90	0.79
Physical-Chemical Conditions												
T (°C)	**825**	**815**	**837**	**818**	**810**	**869**	**853**	**827**	**820**	**898**	**911**	**829**
uncertainty (σ_{est})	22	22	22	22	22	22	22	22	22	22	22	22
P (MPa)	**114**	**111**	**136**	**107**	**120**	**185**	**182**	**139**	**132**	**286**	**291**	**137**
uncertainty (Max error)	13	12	15	12	13	20	20	15	15	71	32	15
continental depth (km)	4.3	4.2	5.1	4.0	4.5	7.0	6.9	5.2	5.0	10.8	11.0	5.2
ΔNNO	**1.2**	**1.3**	**0.9**	**1.4**	**1.0**	**1.1**	**0.8**	**1.1**	**1.1**	**0.3**	**0.1**	**0.9**
logfO_2	**-12.1**	**-12.3**	**-12.2**	**-12.1**	**-12.6**	**-11.3**	**-11.9**	**-12.2**	**-12.3**	**-11.6**	**-11.5**	**-12.3**
uncertainty (σ_{est})	0.4	0.4	0.4	0.4	0.4	0.4	0.4	0.4	0.4	0.4	0.4	0.4
H_2O_{melt} (wt.%)	**4.2**	**4.3**	**4.6**	**4.2**	**4.8**	**5.2**	**5.5**	**4.9**	**5.0**	**5.8**	**6.0**	**4.9**
uncertainty*	0.4	0.4	0.4	0.4	0.4	0.4	0.4	0.4	0.4	0.9	0.9	0.4

Table 17. Chason–Runtu Jarita silicic and mafic lava amphibole data from Watts (1995) with physical-chemical values calculated using Ridolfi et al., (2010).

	Silicic Lavas								Mafic Lavas			
	Chascon CC01	Chascon CC01	Chascon CC04	Chascon CC04	Dome G CC30	Dome G CC30	Dome H CC33	Dome H CC33	Dome F CC31	Dome F CC31	Dome C CC14	Dome C CC14
SiO_2	44.92	46.4	45.46	45.16	44.99	45.72	43.26	46.02	44.61	45.87	42.35	45.59
TiO_2	1.23	0.98	1.38	1.16	1.16	0.97	1.84	1.07	1.43	1.58	3.16	1.11
Al_2O_3	8.63	7.82	8.09	7.98	8.35	7.82	9.67	8	8.31	8.73	11.19	7.92
Cr_2O_3												
FeO	16.64	15.93	15.06	15.45	15.96	15.68	16.48	15.92	15.5	13.12	12.10	15.36
MnO	0.64	0.57	0.59	0.54	0.42	0.46	0.56	0.52	0.49	0.39	0.14	0.56
MgO	11.89	12.34	12.26	12.37	12.66	13.02	11.02	12.15	12.16	13.51	13.64	12.18
CaO	11.97	12.07	11.67	11.67	12	11.63	11.35	12.04	11.57	11.59	11.61	11.81
Na_2O	1.36	1.28	1.29	1.33	1.35	1.19	1.52	1.31	1.35	1.48	1.98	1.20
K_2O	1.1	0.92	0.92	0.96	0.98	0.96	1.34	0.94	0.82	0.73	0.85	0.91
Physical-Chemical Conditions												
T (°C)	**852**	**823**	**834**	**835**	**851**	**828**	**878**	**829**	**844**	**851**	**951**	**827**
uncertainty (σ_{est})	22	22	22	22	22	22	22	22	22	22	22	22
P (MPa)	**166**	**134**	**148**	**144**	**154**	**134**	**224**	**142**	**158**	**168**	**312**	**142**
uncertainty (Max error)	18	15	16	16	17	15	25	16	17	18	34	16
continental depth (km)	6.3	5.1	5.6	5.4	5.8	5.1	8.5	5.4	6.0	6.3	11.8	5.4
ΔNNO	**0.7**	**0.9**	**0.8**	**0.9**	**1.0**	**1.2**	**0.3**	**0.8**	**0.8**	**1.1**	**0.6**	**0.9**
logfO_2	**-12.1**	**-12.5**	**-12.3**	**-12.2**	**-11.8**	**-12.0**	**-12.0**	**-12.5**	**-12.1**	**-11.7**	**-10.4**	**-12.4**
uncertainty (σ_{est})	0.4	0.4	0.4	0.4	0.4	0.4	0.4	0.4	0.4	0.4	0.4	0.4
H_2O_{melt} (wt.%)	**4.7**	**5.0**	**5.1**	**4.7**	**4.5**	**4.4**	**4.7**	**5.0**	**5.2**	**5.4**	**5.1**	**5.2**
uncertainty*	0.4	0.4	0.4	0.4	0.4	0.4	0.7	0.4	0.4	0.4	0.8	0.4

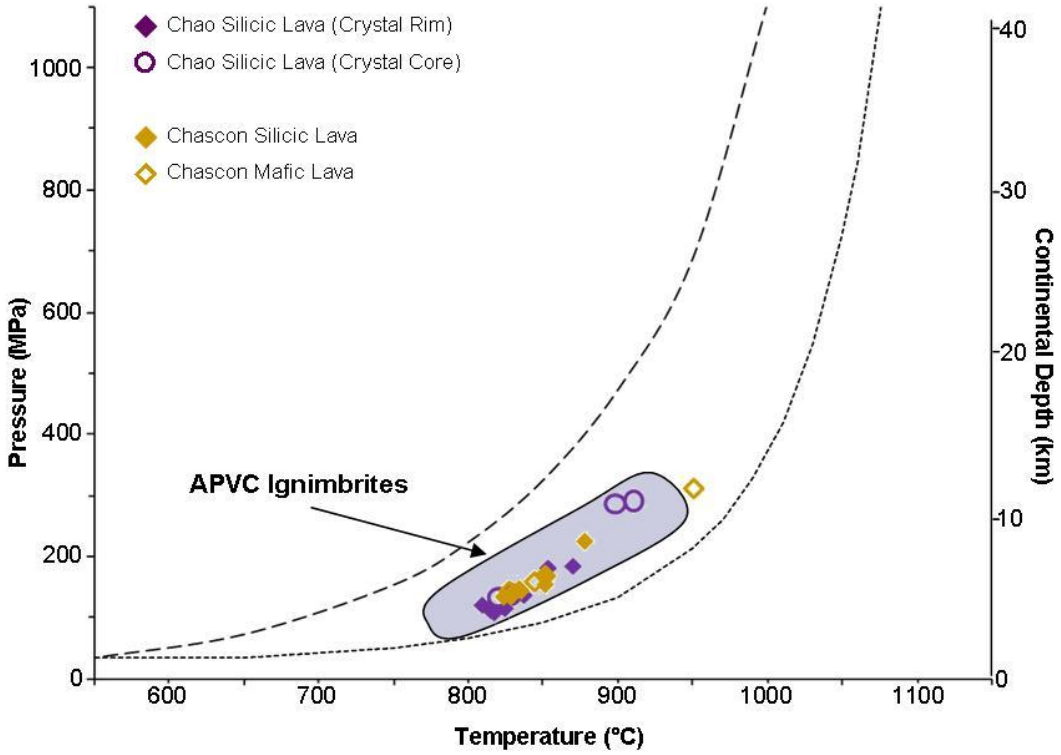

Figure 19. Amphibole pressure vs. temperature plot of Chao and Chascon Lavas Range of APVC ignimbrites displayed by gray field. Amphibole data for Chao and Chascon from de Silva (unpublished) and Watts (1995), respectively. Data for APVC from Abot (2010). Plot created from Ridolfi et al. (2010). Black dotted line represents the maximum thermal stability and the black dashed line represents the upper limit of consistent amphiboles (Ridolfi et al., 2010).

5.3.5 Summary

Temperature and oxygen fugacity values provided by touching magnetite-ilmenite pairs plot very near to the values from non-touching magnetite-ilmenite combinations checked for equilibrium by the Bacon and Hirschmann (1988) method, showing that these non-touching combinations are in fact representative of the magma conditions. In the domes where pairs create outlier temperatures or more than one temperature/oxygen fugacity population, these are found to be related to one or more magnetite or ilmenite crystals with slightly differing compositions from the average, though still in equilibrium.

Overall, using the data from this study with the Ghiroso and Evans (2008) model, the temperatures from all of the domes range from 699°C to 903°C and ΔNNO values of 0.89 to 1.57. Using the Anderson and Lindsley (1988) model, the temperatures range from 793°C to 908°C and log fO_2 ranges from -12.3 to ~-10.1. The amphibole temperature data, obtained through the Ridolfi et al. (2010) model, range from 810°C to 878°C and thus agree more closely with the Anderson and Lindsley (1988) temperatures than those of Ghiorso and Evans (2008).

The past data from Chao agrees with what we have found in this study, with an average temperature and log fO_2 from the Anderson and Lindsley model of ~840°C and ~-11.3, respectively. However, the Watts et al. (1999) data from Chascon-Runtu Jarita, modeled with the Anderson and Lindsley (1988) model, give temperatures and oxygen fugacities much lower than our data show for Chascon or any of the other domes, using the same Anderson and Lindsley (1988) model. While these data do not agree with the exact temperatures and oxygen fugacity, we have found for this study, it does however illustrate that the mafic magmas from Chascon-Runtu Jarita have much higher temperatures and oxygen fugacities than those found in the silicic magmas. Though none of the mafic magmas from the domes were analyzed for temperatures via Fe-Ti oxide in this study, it is assumed that this relationship seen in the Watts et al. (1999) data between pairs from mafic (hotter) and silicic (cooler) magmas exist in the other domes as well. The potential mixing of the mafic magma, and its magnetite and ilmenite crystals, with the silicic magma could explain why some pairs show higher temperatures and oxygen fugacity values. These pairs may have first existed in the mafic magma and then only shortly before eruptions were included into the silicic magma.

APVC ignimbrite and lava data was also gathered from de Silva (1987) and plotted as fields on Figure 17 and Figure 18. The vast majority of temperature and oxygen fugacity data obtained for this study plot well within the overall APVC field. Also shown in the figures is the comparison of the APVC data to those of a few other well

known silicic systems where it is shown that the field of APVC plots very similarly to that of the Fish Canyon Tuff.

Amphibole barometry calculated for Chao and Chascon-Runtu Jarita show very similar pressures for the primary silicic magmas of the domes with Chao ranging from 107 to 185 MPa and Chascon-Runtu Jarita from 134 to 224. These give very similar ranges in continental crust depths, 4 to 7 km depth for Chao and 5.1 to 8.5 km in Chascon-Runtu Jarita. Amphiboles from mafic magmas of Chascon-Runtu and the more mafic cores of Chao amphiboles plot at higher pressures and thus deeper in the crust. Graphical comparison of these data and the data from APVC ignimbrites (from Abot, 2010) are plotted in a pressure vs. temperature plot (Figure 19). The data from these domes fall well within the field given by the APVC ignimbrites, with the exception of one amphibole from Chascon-Runtu Jarita mafic lavas.

The similarity of the temperature and pressure data from these domes once again suggest the similarity of the magma that formed these domes to each other and also to APVC ignimbrites.

5.4 Chapter Summary

The combination of new and previous data and results on the petrography, chemical composition, and magmatic conditions support previous recognition (i.e de Silva et al., 1994) that these five domes are very similar to each other. They all share a crystal rich nature (>50%) with a similar phenocryst assemblage in both the silicic and mafic lavas. Compositionally, the primary silicic magma is high-K dacite to rhyolite with similar ranges in trace elements, and nearly all show abundant mafic enclaves of andesite. Additionally, the temperatures, log fO_2/ΔNNO and pressures from each dome share similar ranges to the other domes for any model used. Furthermore, not only are the domes similar to each other, they are also similar to the APVC system as

a whole in crystal rich nature, similar chemical composition and temperature/oxygen fugacity/pressure.

The crystal rich nature and phenocryst characteristics and assemblage indicate that the magma which fed these dome eruptions was very texturally mature. This crystal rich nature and textural maturity could indicate that the magma body from which these lavas originated was, or was within, a large body of crystal mush. This textural maturity comes despite some higher magmatic temperatures (>900°C) and attests to the presence of a complex thermal and crystallization history; which is understandable given the magnitude of previous magmatic and volcanic activity within the region of these domes.

In addition to temperatures, the pressures given by amphibole in the silicic lavas suggest that the magmas that formed at least two of the domes erupted from an upper crustal source located at 4 to 8 km depth. The amphiboles from the mafic magmas suggest a much deeper source.

The presence and magmatic characteristics of mafic enclaves in these domes indicate ongoing injection of hotter mafic magma into the system from depth and may have had a number of effects on the system including but not limited to mixing, thermal heating, and potentially triggering the eventual eruption.

6.0 Geochronology

In attempting to address the three primary research objectives of this study (determining the magmatic source, determining the magma residence, and exploring what these domes represent for the overall APVC system), all require accurate and up-to date geochronology of the eruption age and magmatic system.

Here data and observations from previous studies are combined with new $^{40}Ar/^{39}Ar$ dating on biotite and U-Th and U-Pb dating on zircon to provide not only the eruption age of the domes, but also trace the timescales of magmatic system prior to eruption.

Samples used for geochronological analysis come from a number of sources. First, samples from all five domes were collected during previous field seasons by Shan de Silva; these samples were used primarily for eruption age dating and preliminary zircon separations. Second, during the 2009 Chile field session, nine samples were collected relating directly to this study. Four of these nine samples, one from each Chilean dome, were used primarily for zircon separations. Lastly, one additional sample from Chascon was collected by Jason Kaiser in 2010 to supplement zircon separations. These samples were separated for sanidine, biotite and zircon using a variety of techniques and then analyzed for $^{40}Ar/^{39}Ar$ on biotite and sanidine, and U-Th and U-Pb on zircon.

6.1 Sample Prep and Mineral Separations

To separate for the zircon, sample rocks were physically broken down to smaller size fractions using a steel hammer and plate, jaw crusher, or disk mill. The sample was then sieved to separate for three different size portions, >0.71mm, 0.71 to 0.2mm, and <0.2mm. Given that the zircon from these lavas are nearly always in the <0.2mm size fraction, the larger size fractions were crushed further to obtain a sufficient amount of the <0.2mm material. This material was then collected in a container and repeatedly

washed with water to decant and remove the clay0-sized particles. The remaining sample was then dried.

After the sample had dried, it was spread out on a clean sheet of paper and the highly magnetic minerals were removed by repeatedly passing a large hand magnet over the sample. After the hand magnet, the samples were moved to a Frantz magnetic separator where the magnetic portion of the samples was removed in 0.25, 0.75, and 1.25 Amp. steps.

The remaining non-magnetic sample was then placed in a separatory funnel of Methylene iodide (specific gravity of 3.32) and after a thorough stirring, dense minerals were given time to sink. After a few minutes to allow settling, an initial decant was preformed, allowing the lower most portion of the funnel, containing the minerals denser than the MI, to fall into filter paper. Once the liquid MI had filtered through the remaining dense sample was washed with acetone to remove any MI residue.

Following the MI procedure, the remaining dense separate was placed in a small Teflon beaker with a few drops of dilute (10-15%) hydrofluoric acid. This acid bath removed any glass from the sample or zircon crystals. The sample was then rinsed with water and allowed to dry. Once dry, all identifiable large and euhedral zircon were picked and placed in a glass vial for storage and later analysis. During the course of the separations all substantial separates (physical, magnetic, etc) were retained for potential future use.

The methods used for separations of biotite (and attempted for sanidine) are similar and follow closely to the methods described in Salisbury et al. (2011). Staining method using sodium cobaltnitrite was attempted following modifications of the method outlined by (Hynek et al., 2011). However, this method was unsuccessful in yielding any sanidine.

6.2 $^{40}Ar/^{39}Ar$

6.2.1 Previous Work

$^{40}Ar/^{39}Ar$ dating allows for estimation of the eruption age of volcanic products. The accuracy of the age depends on the mineral phase being used, however, it is typically conducted on biotite and, more preferentially, on sanidine. Recent studies on APVC volcanics (e.g. Hora et al., 2010) suggest that biotite will give erroneously older ages and is not as precise or dependable as sanidine. That being noted, Dunne (1998) estimated eruption ages of the Chascon-Runtu Jarita dome complex using both $^{40}Ar/^{39}Ar$ on biotite and sanidine. Dunne's work placed the ages of the complex from 190 ± 50 ka to 124 ± 4 ka with biotite and 97 ± 2 ka to 87 ± 4 ka with sanidine (Table 18).

No $^{40}Ar/^{39}Ar$ on sanidine has previously been conducted on any of the other domes, however single crystal laser fusion (SCLF) $^{40}Ar/^{39}Ar$ on biotite has been conducted for Chao by de Silva et al., (1994). Though it was noted by the author that the individual crystals of biotite from each sample yielded anomalously old ages which may have been the result of several causes including xenocrystic contamination, excess Ar or K leaching. As a result the age of Chao is not well constrained.

Additional to $^{40}Ar/^{39}Ar$ dating, K-Ar dating on biotite has been conducted on Chao, Chanka and Tocopuri. However, it should be noted that these dates tend to date much older and it is likely the $^{40}Ar/^{39}Ar$ dates are far more representative of the actual eruption age, as dating techniques and precision has improved since these initial dates. K-Ar dating of three biotite separates from Chao by de Silva et al. (1994) suggests an average age of 423±100 ka, however given the results of the SCLF $^{40}Ar/^{39}Ar$ dating on biotite from the same study, it is noted that true age of Chao is likely less than the K-Ar age, the amount of which being unknown. Additional to Chao, K-Ar by previous studies was conducted on Chanka and Tocopuri. Chanka was dated by Roobol et al.

(1974), who placed the age of the dome at 1.5 Ma. K-Ar dating on Tocopuri by Lahsen (1984) placed the age of that dome at <1 Ma. All previous dates are summarized in Table 18.

No previous dating on Chillahuita is known, but given similarity to the other domes, previous authors included it in with the other domes as a young dome of the APVC (i.e. de Silva et al., 1994).

Table 18. Eruption ages of domes from previous studies.

	$^{40}Ar/^{39}Ar$				K-Ar	
	Sanidine		Biotite		Biotite	
Dome	Age (ka)	(2σ +/-)	Age (ka)	(2σ +/-)	Age (ka)	(2σ +/-)
Ages from Dunne (1998)						
Chascon-Runtu Jarita (Cerro Guichi)	87	4	190	50		
Chascon-Runtu Jarita (Dome C)	88	4	124	9		
Chascon-Runtu Jarita (Dome F)	97	2	170	20		
Ages from de Silva et al, (1994)						
Chao (Sample 985)			387	120	310	263
			157	108		
			212	80		
			14	87		
			-672	97		
			-396	116		
Chao (Sample 986)			931	1131	533	254
			186	225		
			-328	263		
			-141	100		
			-176	86		
			-560	64		
Chao (Sample 987)			189	105	470	135
			4216	312		
			-430	126		
			780	191		
			3233	669		
Ages from Lahsen (1984)						
Tocopuri					<1000	
Ages from Roobol et. al., (1974)						
Chanka					1500	100

6.2.2 Results

As no $^{40}Ar/^{39}Ar$ on sanidine dating had been conducted on any of the five primary domes, with the exception of Chascon, one goal of this study was to obtain accurate eruption ages from conducting $^{40}Ar/^{39}Ar$ on sanidine for all of the other domes. However, sanidine could not be found in the lavas from the domes and therefore the use of biotite was employed as a replacement for the sanidine for this study. The samples used for dating were sent to the lab prior to the November 2009 field session, and thus samples collected by Shan de Silva in previous field seasons were used.

Rock samples were sent to the Rare Gas Geochronology Lab at the University of Wisconsin, Madison where biotite was separated by first crushing the rock then picking euhedral biotite crystals. Biotite crystals were then cleaned ultrasonically in dilute (5%) nitric acid for one minute to remove any glass. Once separated the sanidine and biotite crystals were placed in Al foil packets which were then placed in into wells in Al disks interspersed with 28.34 Ma sanidine standard from the Taylor Creek rhyolite (Renne et al., 1998). The Al disks were then loaded and irradiated for three hours in the TRIGA research reactor at Oregon State University. Once irradiated the crystal samples were returned to UWisconsin where biotite was analyzed via Single-Crystal laser-fusion (SCLF). During this process, biotite was treated with a 0.1 Watt clean-up using a defocused laser beam to release loosely bound, atmospherically absorbed, argon. Following this clean-up, the biotite was fused for 75 s and then followed by gas clean-up on two SAES GP50 getters for 600 s. Isotopic analysis and data reduction followed the procedures of Smith et al. (2003).

Summary reverse isochrons and age spectra on Figure 20, full analytical results are presented in Appendix C. Chao yields an age of 111.2 ± 7.5 ka, obtained through the $^{40}Ar/^{39}Ar$ age spectra on the dome, with a Mean Square of Weighted Deviates (MSWD) of 0.84. The $^{40}Ar/^{39}Ar$ age spectra from Chillahuita yields and age of 107.8 ± 6.4 ka with an MSWD of 1.13. The Tocopuri $^{40}Ar/^{39}Ar$ age spectra yields and age of

110.3 ± 3.4 ka with and MSWD of 1.08. Finally, the $^{40}Ar/^{39}Ar$ age spectra from Chanka yields an age of 119.8 ± 5.4 ka with a MSWD of 0.44. See Table 19 for a summary of ages and Figure 20 for age spectra and reverse isocrons for these domes. The resulting eruption age data places the eruption of these domes within 12.0 ± 11.8 kyr of each other.

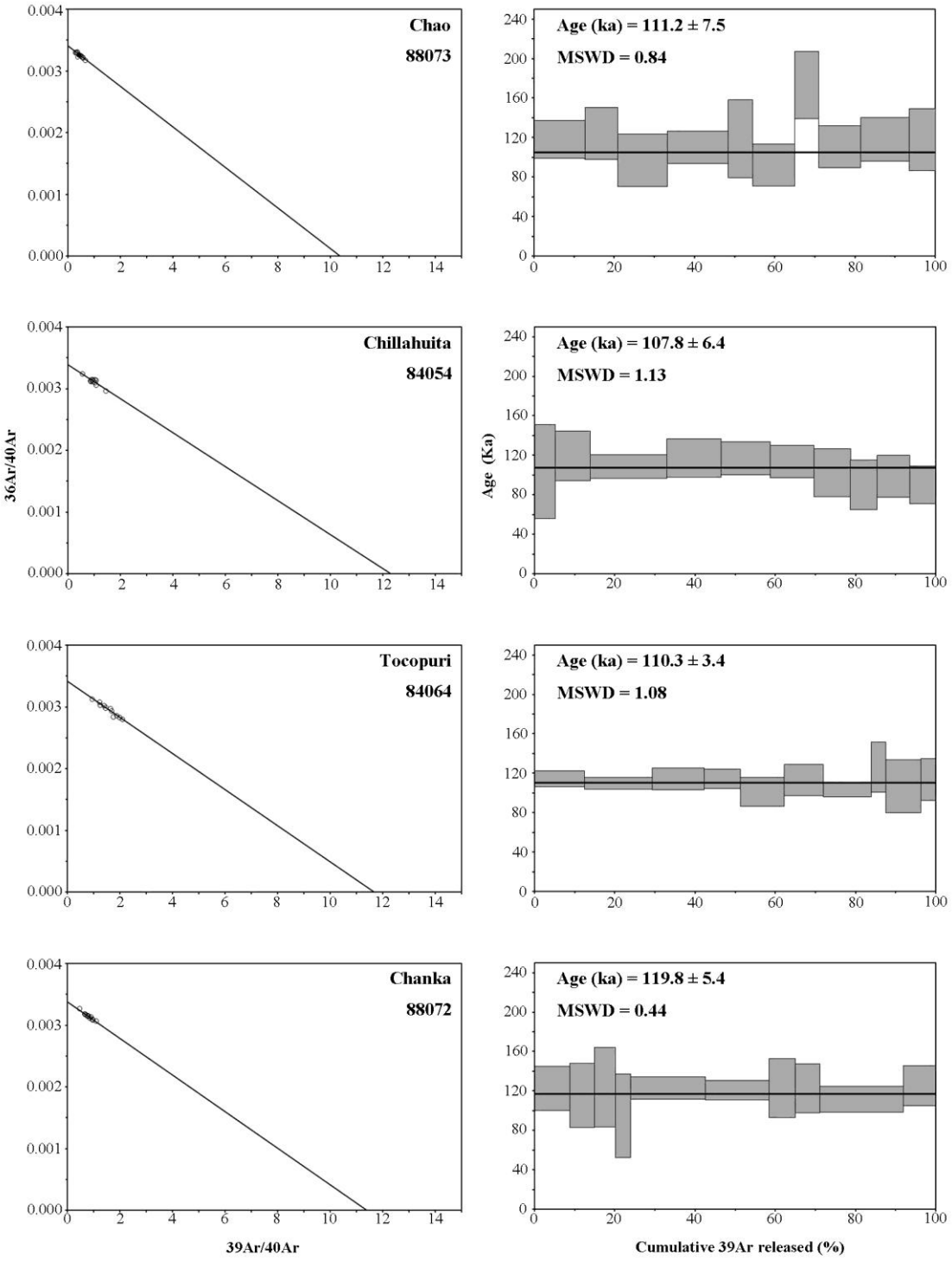

Figure 20. Inverse isochrons and age spectra for age determinations made for this study from four of the five primary domes (excluding Chascon).

Table 19. Eruption ages from this study.

Dome	Sample	$^{40}Ar/^{39}Ar$ (Biotite) Age	(2σ +/-)	MSWD
Chao	88073	111.2	7.5	0.84
Chillahuita	84054	107.8	6.4	1.13
Tocopuri	84064	110.3	3.4	1.08
Chanka	88072	119.8	5.4	0.44

The Mean Square of Weighted Deviates (MSWD) value measures the scatter of the individual step ages with their associated errors and can be used as a statistical goodness-of-fit indicator in which the lower MSWD value, the better the line fits the data. A lower MSWD therefore means a better constrained age for a given isocron or spectra; ages that show MSWDs of <2.5 are commonly accepted values. Inspecting and applying the MSWD calculation to our data shows that the inverse isocrons and age spectra of the samples from this study are both fairly clean visually and well constrained statistically given the relatively low MSWD values (Figure 20). When the domes are treated as a group and the ages and errors are combined, it yields and MSWD of 1.4.

6.2.3 Summary

While no sanidine was available for $^{40}Ar/^{39}Ar$ dating, the use of biotite at least gives some age data to help put these domes in context with one another. Furthermore, while little previous $^{40}Ar/^{39}Ar$ dating has been conducted on these domes, previous dates on Chascon and Chao are in general agreement with dates acquired for this study.

The dates from Dunne (1998) have a wider age range than is seen in newer dates for the four Chilean domes, but the majority fit well with the dates from this study and further support the idea that the five primary domes of this study were erupted within a relatively small window of time, likely a few tens of thousands years. Furthermore, the

Dunne (1998) data helps illustrate the difference between $^{40}Ar/^{39}Ar$ on sanidine vs. biotite, showing that $^{40}Ar/^{39}Ar$ dating on biotite will date erroneously older when compared to $^{40}Ar/^{39}Ar$ dating on sanidine from the same lava (i.e Hora et al., 2010). In comparing the sanidine and biotite ages from a given Chascon-Runtu Jarita dome, the sanidine age ranges from 36 ± 13 kyr to 136 ± 15 kyr younger than the biotite age. Considering the strong similarities between the Chascon-Runtu Jarita lavas and the lavas of the four Chilean domes, it is likely that a similar age discrepancy also exists in the new biotite ages from this study and presumably the sanidine eruption age would date much younger. Thus if the minimum offset seen in the CRJ ages is applied to the biotite ages from the Chilean domes, it places the eruption ages of the domes to <100 ka. Given $^{40}Ar/^{39}Ar$ on biotite ages from the four domes are clustered and in relative agreement with the biotite ages from Chascon, we interpret the sanidine eruption age of Chascon to be roughly the eruption age of all the domes.

Regardless if any offset is applied, or if the sanidine eruption age from Chascon is used for all the domes, these ages place the eruption of the domes as some of the most recent volcanic activity within the APVC. The biotite ages from the four Chilean domes range from 107.8 ± 6.4 ka to 119.8 ± 5.4 ka for a minimum difference of 1.2 ka and a maximum of 23.8 ka when considering errors. If only considering Chao, Chillahuita and Tocopuri, the ages are strongly concordant within error. Thus it is likely that the eruption of these domes occurred within a few tens of thousands years of each other as a distinct temporal pulse of volcanism.

6.3 U-Th disequilibrium in Zircon

6.3.1 Introduction

U-Th dating on zircon provides a window into the evolution of the magmatic system. Through the spectra of zircon crystallization ages and the populations/temporal patterns they reveal, information on the history of the magma system that created the

zircons can be obtained. This information includes magmatic residence times, relative magmatic source, and thermal history (see Chapter 2 – Purpose and Scope).

While U-Th dating on zircon is well established and has been applied to other large scale silicic systems (i.e. Reid et al., 1997; Lowenstern et al., 2000; Vazquez and Reid, 2002), to date, no previous zircon work on younger (<350ka) APVC lavas or ignimbrites has been done. All previous APVC zircon dating has been restricted to dating older deposits via U-Pb (i.e. Schmitt et al., 2002)

6.3.2 Results

U-Th measurements on zircon were conducted via Secondary Ionization Mass Spectrometry (SIMS) at the University of Los Angeles, California on the Cameca IMS-1270. Zircon crystals were separated at Oregon State University and then transported to UCLA. At UCLA 1 inch aluminum disks were prepared with five ~5 mm diameter wells filled with Indium metal. 20 to 30 zircon crystals were then gently pressed into each Indium well. Once all five wells had been filled with zircon, the aluminum mount was then polished, washed with dilute HCL, allowed to dry, and then thinly coated with Au. Mounts were then placed into the SIMS where the zircon was analyzed for U-Series dating.

U-Th Specific Methods

U-Th dating on zircon via SIMS was based on techniques by Reid et al., (1997). A primary $^{16}O^-$ beam intensity of 40-80 nA was focused on a ~30 µm spot. Secondary ions were accelerated to accelerated at 12.5 keV with an energy band-pass of 50 eV and analyzed at mass resolution power of ~5000. Reference zircon AS-3 (Paces and Miller, 1993) was used as a standard to calibrate the relative sensitivities for ^{238}UO and ^{232}ThO by measuring the radiogenic $^{206}Pb/^{208}Pb$. Th isotopic activity ratios

(^{230}Th)/(^{232}Th) of 0.697 to 0.704 (Bourdon et al., 2000, Parinacota dacite, PAR-200-1 and Parinacota rhyolite, PAR-91-014) were used in the age calculations.

Mineral separation of the lavas from the five primary domes yielded a good amount of large (>100um) and euhedral zircon crystals that were able to be analyzed via SIMS for U-Th age dating on zircon. Two trips to the SIMS at UCLA yielded 252 U-Th model ages from the rims of the zircon. Given the quantity of ages and associated errors these ages are most easily viewed as probability density plots (PDP) on a dome by dome basis. Additionally, some of the zircon rim ages fell on or over the equiline (~350ka) and a number of these zircon were later analyzed via U-Pb age dating on zircon and are discussed in the next section. PDPs of the U-Th model ages from these domes are seen in Figure 21, a compiled table of these data can also be found in the appendices. Dome by dome results are discussed below.

Chao

Separations from Chao yielded a good amount of large (up to 200 µm) and euhedral zircons, of these the rims of 52 were analyzed for U-Th age dating on zircon. The yielded model ages range from 79.1 ka to several which fall on the equiline. Probability density plots of the ages and associated errors show an age spectra with multiple peaks at ~80, 100 and ~220 ka with the 100 ka peak being most pronounced. After the 220 ka peak the age spectra falls of markedly as the ages approach the equiline.

Chillahuita

Separations from Chillahuita also yielded a good amount of large and euhedral zircons, of which 57 were analyzed for U-Th age dating on zircon. The yielded model ages range from 79.9 ka to those which fall on the equiline. Probability density plots

show an age spectra with one very pronounced peak at ~90 ka and one lesser pronounced peak at ~220 ka. Again, after the later peak the age spectra falls of markedly as the zircon ages approach the equiline.

Tocopuri

Like Chao and Chillahuita, separations from Tocopuri yielded a good amount of large and euhedral zircons, of which 53 were analyzed for U-Th age dating on zircon. The yielded model ages range from 85.8 ka to some that fall on the equiline. Probability density plots show an age spectra with one very pronounced peak at ~100 ka and perhaps a much lesser peak slightly earlier at ~170 ka, after which the age spectra falls off . There is no ~220 ka peak as seen in some of the other domes.

Chanka

Unlike the other domes, zircons from Chanka were slightly less abundant and slightly smaller, though they were still euhedral. The rims of 45 zircon were analyzed for U-Th age dating on zircon. The yielded model ages range from 76.1 ka to multiple zircon ages which that fall on the equiline (~350 ka). Probability density plots show an age spectra with a very pronounced peak at ~85 ka and one other peak at ~220 ka, after which the age spectra once again falls off.

Chascon

Separations from Chascon yielded a good amount of large and euhedral zircons, of which 54 were successfully analyzed for U-Th age dating on zircon. The yielded model ages range from 103.9 ka to those that fall on the equiline. Probability density plots show an age spectra which is slightly different from the other domes and shows two pronounced peaks, one at ~140 ka and the other at ~200 ka, after which the age spectra falls off.

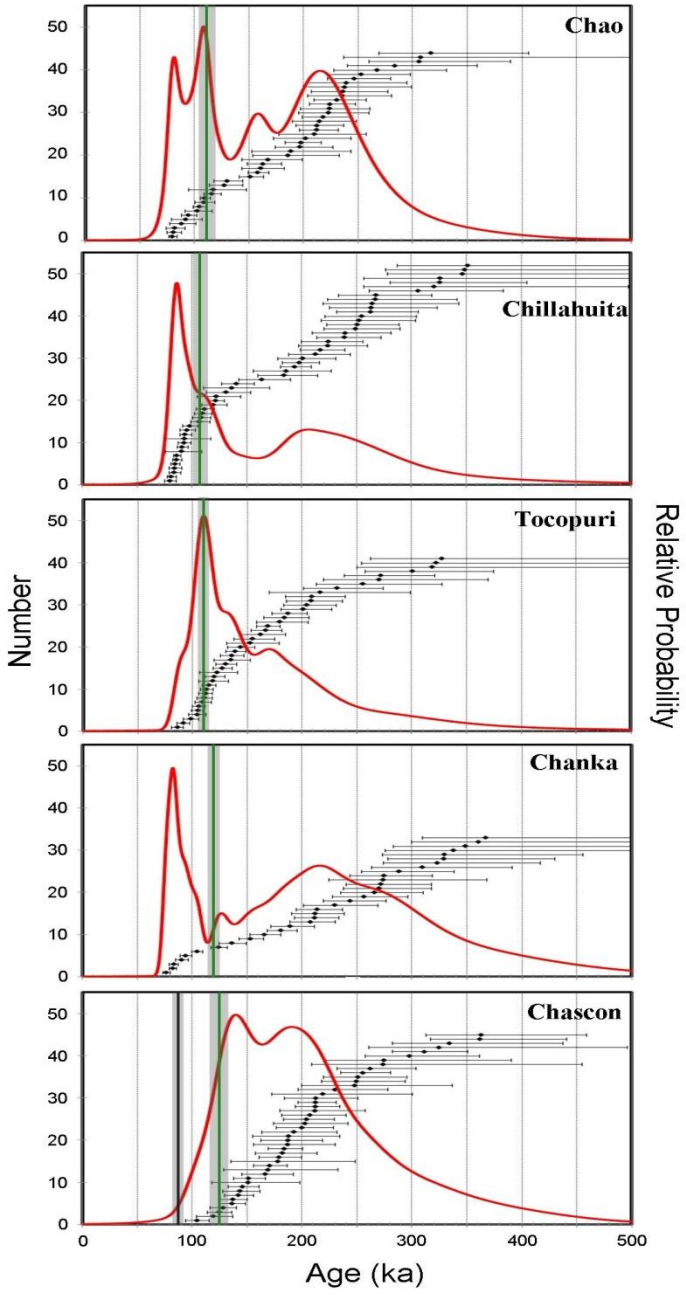

Figure 21. Probability density plot of the U-Th model ages from zircon rims for each dome. The red line illustrates the likely distribution of the zircon population given the zircon model ages and 1σ errors. The actual model ages and 1σ errors are illustrated by the black diamonds and associated error lines. The green vertical line represent the biotite $^{40}Ar/^{39}Ar$ eruption age for each dome, with the shaded region representing the 1σ error. The black vertical line represents sanidine $^{40}Ar/^{39}Ar$ age from Chascon-Runtu Jarita obtained from Dunne, 1998.

6.3.3 Summary

Overall, the PDP spectra of ages given from the zircon from each dome show multiple peaks and a similar spectra from dome to dome. These peaks in the age spectra indicate pulses of zircon crystallization at that time which could be due to a number of factors but is most likely related a thermal event, such as injection of hotter magma, which raised the temperature of the cooling silicic magma sufficiently to reinvigorate crystallization of zircon for a time (i.e. Watson and Harrison, 1983). The spike in zircon crystallization near the time of eruption of each of these domes can potentially be explained by the injection of hot andesitic magma into a larger and cooler body of silicic magma. This injection may have not only caused zircon crystallization, but also potentially the eruption of these domes, as evidenced by the presence of andesitic enclaves hosted in the silicic lava of all the domes. Furthermore, the presence of shared PDP age spectra peaks between domes at 80-100 ka and also 200-220 ka likely indicates that the domes have a similar thermal history and likely shared the same thermal events, attesting to the potential for a shared upper-crustal source between the domes.

Another thing of note is that the individual zircon ages are quasi-continuous until at minimum >275 ka . This is reflected in the PDP spectra, which takes into account the age and uncertainties. These show a continuously elevated spectra until this age or older. A continuously elevated spectra implies that the probability of the zircon population as shown by the PDP spectra stays well above and never drops to or near a value of zero at any point. This continuous duration of zircon crystallization from eruption back to >275 ka indicates that the magma in which the zircon was crystallizing in must have remained above or very near the solidus for that period of time. If it had dropped below the solidus for any extended period of time zircon would not have been crystallized and thus the ages and spectra of ages would not be continuous.

6.4 U-Pb in Zircon

6.4.1 Introduction and Previous Data

Similar to U-Th dating on zircon, U-Pb dating provides window into the evolution of the magmatic system further back in time (>350 ka). U-Pb dating can be used in much the same way as U-Th, which is to develop a zircon age and population spectra, however, in this study it is used to probe the older reaches of the magmatic system. Specifically, it is used to date the zircon crystals which are too old for the U-Th method, and also to date some zircon interiors to gain an idea of the antecrystic and xenocrystic history of the magmatic system.

No previous U-Pb work has been conducted on the domes of this study, however, previous work has been conducted on other APVC lavas and ignimbrites. Schmitt et al. (2002) conducted U-Pb analyses on two La Pacana ignimbrites, the Toconao (4.0±0.2 Ma) and Atana (3.96 ± 0.08) ignimbrites. The study argues for a stratified magma chamber and show that U-Pb ages agree well with the eruption age of both the units. These data supported residence times of less than 1 Ma. In addition, xenocrystic (~13 Ma) zircons provide evidence for earlier onset of magmatism in the APVC than documented previous to this study.

Folkes (2010) also conducted U-Pb dating on zircon, from Cerro Galan. The results from Folkes' study show zircons that crystallized up to 500 ka prior to eruption of the ignimbrite, which is said to be consistent with long residence times of crystal mushes in the upper crust. Also found were several antecrysts which indicate that recycling and incorporation of the magmatic systems of previous eruptions was taking place. Furthermore, a few zircon xenocrysts (540 to 500 Ma), inferred to be from the pre-Galan basement, were found. The study uses these results to argue for protracted magma storage, recycling of non-erupted material from previous magmatic events and assimilation of crustal material.

U-Pb Specific Methods.

Large and euhedral zircon crystals that were separated from the dome lavas were initially selected for U-Th age dating on zircon rims. However, many of the zircon rim ages were found to fall close to or on the U-Th equiline at around ~350 ka. Thus, the exact age could not be confidently determined using the U-Th method. Therefore, these older zircon rims, and a few younger ones, were subsequently analyzed by U-Pb methods. Furthermore, given the age capabilities of the U-Pb method we were able to additionally date the interiors of the zircon crystals. Dating the interior ages of the crystals allowed us to observe the difference between the rim and interior of individual zircon grains, highlighting possible antecrystic cores.

Similar to U-Th, U-Pb measurements on zircon were conducted via Secondary Ionization Mass Spectrometry (SIMS) at the University of Los Angeles, California on the Cameca IMS-1270. Zircon crystals were separated at Oregon State University and then transported to UCLA. At UCLA 1 in aluminum disks were prepared with five ~5mm diameter wells filled with Indium metal. 20 to 30 zircon crystals were then gently pressed into each Indium well. Once all five wells had been filled with zircon, the aluminum mount was then polished, washed with dilute HCL, allowed to dry, and then thinly coated with Au. Mounts were then placed into the SIMS where the zircon was analyzed for U-Pb dating.

U-Pb dating on zircon via SIMS is based on methods and protocols from Schmitt et al. (2002). A primary mass-filtered $^{16}O^-$ beam was focused on a ~30-35µm spot. Secondary ions were accelerated to 10 keV with an energy band-pass of 50 eV and analyzed at mass resolution power of ~5000. Pb^+ yields were increased by flooding the analysis chamber with O_2 at a pressure of ~$4x10^{-3}$ Pa. Reference zircon AS-3 (Paces

and Miller, 1993) was used as a standard to calibrate the relative sensitivities for Pb and U .

6.4.2 Results

All five domes and zircons separated from a granitic xenolith from Chascon (collected during the study by Watts et al., (1999) were dated via this method with the youngest zircon age dated being 0.2 Ma and the oldest age being nearly 3.5 Ma. The largest gap between rim and interior was found to be ~3 Myr. The results from the individual domes are discussed in the next section and the compiled U-Pb data from these domes in shown in Figure 22 and Table 20.

Chao

Eleven rim-interior pairs were measured via U-Pb on zircon. The rims ages ranged from 0.17 ± 0.03 Ma to 1.40 ± 0.07 Ma while the interior ages ranged from 0.25 ± 0.05 Ma to 1.64 ± 1.08 Ma. The largest age gap between rim and interior was measured as 0.83 ± 1.13 Myr, in a crystal with a 0.81 ± 0.05 Ma rim and a 1.64 ± 1.08 Ma interior. The average rim-interior gap found in these 11 crystals was 0.30 Myr, however one grain had no distinguishable difference between rim and interior.

Chillahuita

Six rim-interior pairs were measured via U-Pb on zircon for Chillahuita, however, two of these gave data in which the interior was younger than the rim. The four crystals that had a normal rim-interior relationship showed rim ages ranged from 0.30 ± 0.03 Ma to 0.77 ± 0.04 Ma, with three of the four ages clustered at 0.30 Ma. The interior ages ranged from 0.44 ± 0.04 Ma to 1.27 ± 0.05 Ma, resulting in the largest gap of 0.50 ± 0.09 Myr between a crystal with a 0.77 ± 0.04 Ma rim and a 1.27 ± 0.05 Ma

interior. The average rim-interior gap, similar to that of Chao, was found to be 0.32 Myr.

Tocopuri

Eight rim-interior pairs were measured via U-Pb on zircon for Tocopuri, however, like Chillahuita, three crystals displayed a rim-interior relationship where the interior overlapped the rim. The ages of the four crystals that had a normal rim-interior relationship ranged from 0.64 ± 0.04 Ma to 1.50 ± 0.15 Ma, with all of those but one being at or under 1 Ma. The interior ages ranged from 0.77 ± 0.08 Ma to 1.87 ± 0.14 Ma, resulting in the largest gap of 0.47 ± 0.19 Myr in a crystal with a rim age of 0.80 ± 0.12 Ma and an interior age of 1.27 ± 0.07 Ma. Similar to the two previous domes the average rim-interior gap was found to be 0.30 Myr.

Chanka

Nine rim-interior pairs were measured via U-Pb on zircon for Chanka, however, one of these pairs displayed a rim-interior relationship where the interior overlapped the rim. The ages of the eight crystals that had a normal rim-interior relationship ranged from 0.20 ± 0.02 Ma to 0.62 ± 0.04 Ma. The ages of the interiors ranged from 0.33 ± 0.03 Ma to 0.98 ± 0.06 Ma, with the largest rim-interior gap as 0.50 ± 0.10 Myr on a grain with a 0.48 ± 0.04 Ma rim and a 0.98 ± 0.06 Ma interior. The average rim-interior gap found in the zircon from Chanka was slightly less than that found in the previous domes at 0.23 Myr.

Chascon (Dome)

Three rim-interior pairs were measured via U-Pb on zircon for Chascon, all displaying the normal rim-interior age relationship. The rim ages of these crystals ranged from 0.03 ± 1.78 Ma to 0.51 ± 0.01 Ma. The interior ages of these crystals ranged from 0.50

± 0.12 Ma to one crystal which had a 3.46 ± 0.10 Ma interior. Predictably, the largest rim-interior gap was found in this crystal and given its 0.48 ± 0.02 Ma rim age was found to 2.98 ± 0.12 Ma. The average rim-interior gap was also found to be wide at 1.49 Myr.

Chascon (Granite inclusion)

Additional to the five domes, a granitic block brought to the surface during the initial explosive phase of the eruption of Chascon (Watts et al., 1999) was analyzed via U-Pb on zircon. Ten rim-interior pairs were measured, with rim between 2.34 ± 0.08 Ma to 2.74 ± 0.15 Ma and interiors ages between 2.56 ± 0.11 Ma to 3.18 ± 0.31 Ma, with the largest rim-interior difference being 0.63 ± 0.40 Ma. The average gap between rim and core in these zircons was found to be relatively small at only 0.20 Myr.

In addition to the antecrystic zircon found in the granitic inclusion, one extremely old xenocrystic zircon was analyzed. This zircon showed a rim age of 11.1 ± 0.5 Ma whereas the interior of the zircon was Proterozoic in age at 603 ± 22 Ma.

Table 20. Table of U-Pb zircon rim vs. interior ages.

Dome	Sample	Rim Age (Ma)	2σ error	Interior Age	2σ error	Difference
Chao	1_2	0.72	0.03	1.07	0.06	0.35
	1_6	0.29	0.03	0.58	0.07	0.29
	1_8	1.01	0.06	1.26	0.06	0.25
	1_12	0.81	0.05	1.64	1.08	0.83
	1_13	1.40	0.07	1.47	0.07	0.07
	2_4	0.93	0.04	1.40	0.08	0.46
	2_7	0.63	0.05	0.76	0.04	0.13
	2_9	0.94	0.05	1.18	0.12	0.24
	2_10	0.95	0.09	0.94	0.05	0.00
	2_13	0.17	0.03	0.25	0.05	0.08
	2_15	0.90	0.06	1.54	0.34	0.64
Chillahuita	1_3	0.30	0.03	0.61	0.04	0.32
	1_9	0.30	0.03	0.64	0.03	0.34
	1_10	0.77	0.04	1.27	0.05	0.50
	2_2	1.17	0.07	1.08	0.05	-0.09
	2_23	0.30	0.05	0.44	0.04	0.14
	2_27	1.81	0.08	1.26	0.12	-0.55
Tocopuri	1_1	0.69	0.15	0.77	0.08	0.08
	1_6	1.42	0.08	1.31	0.10	-0.11
	1_11	0.80	0.12	1.27	0.07	0.47
	1_20	1.50	0.15	1.87	0.14	0.38
	2_5	0.70	0.11	0.58	0.05	-0.11
	2_19	1.00	0.08	1.17	0.04	0.18
	2_20	0.75	0.06	0.60	0.45	-0.15
	2_22	0.64	0.04	1.05	0.04	0.41
Chanka	1_1	0.58	0.04	0.52	0.63	-0.07
	1_5	0.62	0.04	0.75	0.03	0.12
	1_6	0.46	0.03	0.81	0.25	0.35
	1_8	0.20	0.02	0.33	0.03	0.12
	1_22	0.56	0.08	0.61	0.04	0.04
	2_1	0.44	0.03	0.62	0.03	0.18
	2_2	0.37	0.05	0.55	0.03	0.18
	2_4	0.48	0.04	0.98	0.06	0.50
	2_5	0.29	0.10	0.61	0.03	0.32
Chascon	1_12	0.51	0.01	1.52	0.04	1.01
	2_1	0.03	1.78	0.50	0.12	0.47
	2_8	0.48	0.02	3.46	0.10	2.98
Chascon (Granite)	1	2.52	0.10	2.56	0.11	0.04
	5	2.34	0.08	2.67	0.12	0.33
	7	2.55	0.09	3.18	0.31	0.63
	8	2.47	0.10	2.72	0.08	0.25
	9	2.63	0.09	2.72	0.08	0.09
	10	2.74	0.15	2.74	0.10	0.00
	11	2.80	0.12	2.77	0.15	-0.02
	12	2.54	1.35	2.79	0.10	0.26
	13	2.58	0.09	2.60	0.10	0.02
	15	2.55	0.09	2.75	0.08	0.20

6.4.3 U-Pb Summary

U-Pb dating on the rims and core of these zircons reveal that incorporation and recycling of older magmatic products was taking place. Furthermore, the antecrysts date to at least 3.5 Ma, and thus magmatic activity in this region of the APVC also dates back to a minimum of 3.5 Ma. The lack of any zircon population past 3.5 Ma suggests that either no zircon crystallization was taking place, no incorporation of these older materials occurred, or that older zircon these older magmas produced were thermally resorbed by younger magmas that were hotter and zircon-undersaturated. Lastly, the presence of the 11 Ma zircon rim (with a 603 Ma core) supports, as suggested by Schmitt et al. (2002), that this part of the APVC magmatic system may also date back to or older than the 11 Ma rim.

6.5 Chapter Summary

When pieced together, the results from the $^{40}Ar/^{39}Ar$ eruption age and U-Th/U-Pb zircon model ages form an interesting story of the magmatic evolution of the system that fed these domes. A complete model will be addressed in the next chapter, however, before that can be achieved a few things bear mentioning.

There is a noticeable and important discrepancy in that the $^{40}Ar/^{39}Ar$ on biotite eruption age is older than the youngest zircon crystallization age given by U-Th dating. $^{40}Ar/^{39}Ar$ on biotite can yield erroneously older ages in the APVC lavas due to the presence of extraneous ^{40}Ar (Hora et al, 2010). The eruption age given by biotite is thus likely old and the eruption age of these domes is closer to the most recent U-Th zircon crystallization age. This interpretation is further supported by dating of Chascon lavas via the more accurate $^{40}Ar/^{39}Ar$ dating on sanidine. The Chascon sanidine ages show the expected relationship in which the eruption age of the domes is younger than the youngest crystallization age. Furthermore, the offset between sanidine eruption age and most recent zircon crystallization age is small at ~7 kyr with overlapping errors, depending on which Chascon sanidine age is used, thus supporting

the use of the most recent U-Th zircon crystallization age as a near eruption age in lieu of accurate $^{40}Ar/^{39}Ar$ on sanidine dating.

The closely spaced eruption ages of the domes suggests that these five domes occurred as a distinct temporal pulse in this region of the APVC and some of the most recent volcanism occurring in the APVC as a whole.

The U-Th and U-Pb indicate a complex magmatic and thermal history with the potential for assimilation of not only previous APVC magmatics, but also older basement rock. The U-Th zircon model age spectra indicate that the magma that fed these domes underwent similar thermal histories to the point that it can be reasonably assumed that they are likely from the same upper-crustal source. The continuity of the model age spectra also suggests that the magma had a protracted residence time of >200 ka.

U-Pb data shows through the presence of older antecrysts (~3.5 Ma) that magmatism in this region was active to at least that age. Furthermore, these antecrysts show that assimilation and recycling of antecrystic zircon from older parts of the magmatic system are occurring. Older zircon of ~11 Ma, first support assimilation but also support previous studies (Schmitt et al., 2002), in that the silicic onset of the APVC system was at least this old and likely older. The core of this zircon dates to 603 Ma and suggests that assimilation/recycling of basement rock also occurred at the earlier phases of the APVC.

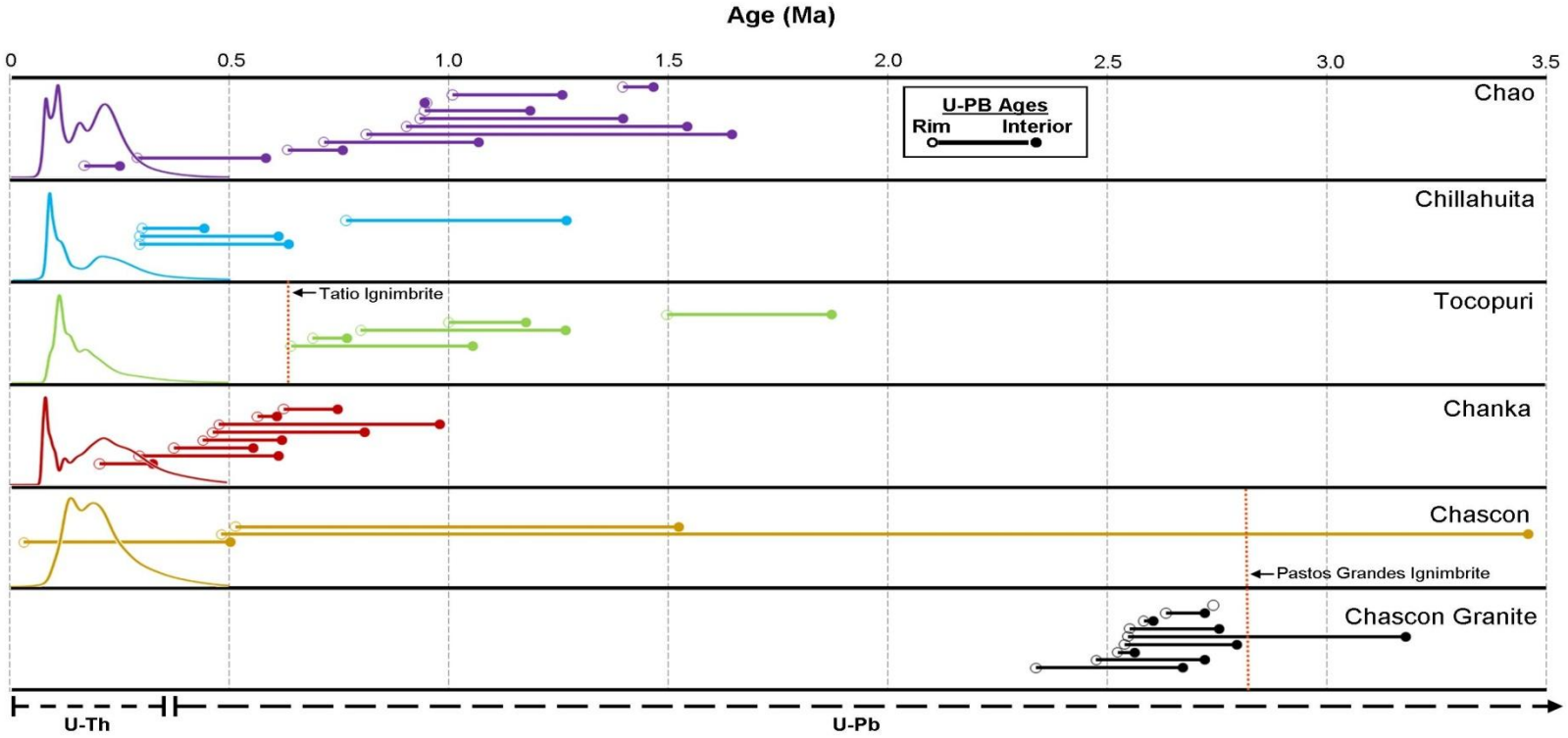

Figure 22. Integrated plot showing the range of zircon U-Th and U-Pb age collected in this study and illustrating differences between rim and interior U-Pb ages on zircon of the five major domes and the granitic inclusion from Chascon. These ages were gathered through U-Pb dating on zircon rims which had been previously analyzed for U-Th but fell on the U-Th equiline. Open circles represent the U-Pb age of the zircon rim while the closed circles represent the U-Pb age of the zircon interior. The line connecting the two represents the difference between the rim and interior ages. The probability density curve of the U-Th rim ages for each dome is shown along the left side of the diagram. The Tatio and Pastos Grandes ignimbrite eruption ages (from Salisbury et. al., 2011) are shown with their geographically relevant dome to give context to events within the magmatic system. The method used from analysis is shown at the bottom of the figure.

7.0 Discussion

7.1 Similarity between the domes

Previous studies involving these domes by de Silva et al. (1994) and Watts et al. (1999) were quick to point out the strong morphological and petrochemical similarities between the domes and suggested that these domes potentially tapped the same magmatic system. Up to now, these similarities have not been geochronologically supported. As a result of this, one of the outlined research objectives of this study was exploring if the magma that fed these domes evacuated from distinct batches of magma or a larger shared source; with the hypothesis being that the magma that fed these domes was evacuated from a larger regional source. However, before the source of the domes could be addressed, it is prudent to examine in more detail the similarity between these domes. Therefore, in attempting to address this objective, this study has expanded on the previous work to demonstrate the striking similarity between these domes goes far beyond what was previously recognized.

The close resemblance of these domes has been demonstrated on multiple scales in the results gathered by this study. On a larger scale, these domes share a morphological similarity with most exhibiting similar volume and the characteristic “torta” shape - roughly circular with flat top and steep sides. Chao is the obvious exception to this rule, however, its anomalously large volume and unusual shape are explained by the fact that it was erupted on a steep topographical scope on the flanks of nearby composite cones Leon and Paniri (de Silva et al., 1994). While the difference in topography may have caused a different morphological character between Chao and the other domes, it had no affect on the nature of the lava which was erupted. The lavas from all of these domes show the same physical characteristics in hand sample including color index, pervasive microvescularity, extremely crystal-rich porphyritic character and the presence of ovoid mafic enclaves. These similarities are also seen in thin section where petrography reveals a high crystallinity of >55% in some cases with a similar phenocryst assemblage (plagioclase > biotite, hornblende, quartz >>

sanidine, sphene, Fe-Ti oxides, apatite) set in a glassy but sometimes microlitic groundmass. Additionally, the mafic enclaves found within all of the domes, to varying degrees, all show similar petrographical characteristics.

Chemically, all of the domes share a narrow range in both major elements and trace elements. All domes plot as high-K dacites to rhyolites ranging from 67 to 72 wt % SiO_2 (Figure 13). The trace elements show similar abundances in multiple distinctive elements, including Sr, Ba, Zr, U, and Th, and all domes are LREE enriched (Figure 14). While variations in composition do exist they are relatively minimal and the range observed is less than shown in the monotonous Atana ignimbrite of Lindsay et al., (2001) or Galan ignimbrite of Folkes (2011). Major and trace element chemistry on the mafic enclaves indicates that while they are different from the primary silicic magmas in the domes, the enclaves from dome to dome are quite similar, with little variation in major and distinctive trace elements (

Figure 15).

A numerical assessment in similarity of sample composition was done using a statistical distance function (D). D is the Euclidean distance between two chemical analyses, where a smaller D value is a better fit, D=0 indicates a perfect match. The value of D which indicates a statistically identical (95% confidence level) composition varies with the degrees of freedom (elements being used) and is calculated using tables of the chi-square distribution (Perkins et al., 1995).

Analyses were divided into three groups defined by SiO_2 concentration, 60-63% SiO_2, 66-69% SiO_2, and 69-72% SiO_2. 10 major oxides were used in the calculations (SiO_2, TiO_2, Al_2O_3, FeO*, MnO, MgO, CaO, Na_2O, K_2O and P_2O_5), resulting in a $D<4.3$ representing the samples being compared are statistically indistinguishable. Calculated values for each sub-set of samples are were placed in Distance Matrices for easy comparison between the domes/samples (Appendix F). Distance values from the three samples which had silica ranges from 60-63% were between 1.29 and 4.00 with an

average of 2.9 and a standard deviation of 1.27. Distance values from the 66-69% SiO_2 group are between 0.27 and 2.54 with an average of 1.18 and a standard deviation of 0.57. Lastly, the distance values from the 69-72% SiO_2 group are between 0.28 and 3.48 with an average of 2.05 and a standard deviation of 0.94. Overall, all of the D values fall below the 95% confidence value of 4.3 and are thus statistically indistinguishable. This distance analyses again demonstrates the strong chemical correlation between the lavas from these domes.

Digging deeper into history and conditions of these lavas prior to eruptions, further similarities exist. Multiple models for assessing temperature were employed, using both Fe-Ti oxides and amphibole, to gather magmatic temperature for the domes. While the models give much different ranges from each other, the domes do show consistent ranges in temperature for a given model. Furthermore, the domes of Chao and Chascon-Runtu Jarita show similar ranges in pressures and depths of equilibrium ranging from 107 to 224 MPa.

Timescales attained through various geochronological methods again illustrate the strong kinship of these domes not only post-eruption but also dating back several hundred thousand years in their magmatic history. $^{40}Ar/^{39}Ar$ on biotite eruption ages of the domes range from 107.8 ± 6.4 ka to 119.8 ± 5.4 ka (Table 19) indicating that these domes occur as a distinct temporal pulse in this region of the APVC. Additionally, zircon, used as a tracer of the magmatic system, shows that these domes experienced a largely similar magmatic history dating back to >350 ka, as indicated by the zircon population spectra seen in Figure 21.

Thus, an overwhelming majority of physical, petrochemical, and geochronological data obtained by this and previous studies suggest that both the silicic and mafic magmas from these domes are incredibly similar in nature and share a history. Furthermore, in agreement with thoughts from previous authors, it is reasonable to suggest that these domes likely originated from the same upper-crustal magma source.

7.2 Evidence for a shared upper-crustal magmatic source

The strong similarities between the domes have lead to the suggestion that these domes were erupted from the same body of magma. In order to better support this claim and fulfill the first research objective of determining the magmatic source, some questions must be addressed.

First, the sheer size of the potential source needs to be addressed. The spatial distribution of the domes can be viewed as roughly elliptical, the largest extents of the ellipse are from Chanka to Tocopuri at ~76 km and from Chao to Chascon at ~32 km. This amounts to an elliptical area of just over 1900 km^2, a very large area for a potential magma body. However, while this area is large, it is not beyond comprehension, as numerous calderas exist both in the world and APVC that rival or surpass this. For example in the APVC, the nearby Pastos Grandes caldera is roughly 60x30 km and to the south La Pacana is 60x35 km (Lindsay et al., 2001). Worldwide, a number of well known calderas surpass this value, as La Garita is 75x35 km (Bachmann et al., 2000) and Toba is 100x30 km (Smith and Bailey, 1968). Therefore, while large, the scale of this magma body is on par with a number of other systems.

The second issue that must be addressed is whether the variations that do exist between the domes invalidate the possibility that these domes could have erupted from the same source. While it is true that variations between the domes exist, they are smaller than the variations that can be observed in single-unit ignimbrite eruptions or caldera systems where no question exist that the eruption originated from the same magma chamber. Thus, the variations found between the domes does not exclude them erupting from the same source; to the contrary, variations would be expected spatially in such a large system.

One variation that does exist and must be addressed is two large differences in Chascon-Runtu Jarita from the other domes. The first difference noted is that Chascon

has slightly different zircon spectra from the other domes. Secondly, that the dome complex it is a part of has a higher proportion of associated mafic lavas. These variations can potentially be explained an older eruption age compared to the other domes. In addition to slightly older $^{40}Ar/^{39}Ar$ eruption ages from biotite, the most recent zircon age is older and the spectra is more truncated than the other domes suggesting that Chascon erupted earlier. This difference in eruption age, however, does not rule out Chascon coming from the same magmatic source as the other domes. A similar ~220 ka peak is shared with Chascon by the other domes (Figure 21) and if Chascon had waited to erupt, the peak it shows just prior to eruption may have moved into a similar position as the ~100 ka peaks seen in other domes. A later eruption age would have lead to further crystallization occurring on zircons, which would have therefore lead to a younger peak. The earlier eruption could also account for the higher percent of mafic magmas as the mafic pulse that likely caused the eruption of the domes may have had less time to mix with the other magmas prior to eruption.

Lastly, the one major question that must be addressed is why these domes have to represent one source, why can they not be distinct pockets of melt that are very similar or simply incorporated older plutons or magma chambers? The best way to address this argument is the large spatial extent of the domes; at the largest extent the domes are roughly 80 km apart. It is thus much more reasonable to explain these domes as one system than it is as separate discrete systems that by coincidence share the same age spectra, lava composition, magmatic history, etc. Distinct chambers could potentially be argued for if only the compositional and thermal history existed, given the overall similarity to the other APVC lavas and products. However, the record of the magmatic evolution as shown by the zircon spectra is hard to argue against. The similarity of the zircon population and spectra, quantitatively and qualitatively, would be hard to achieve unless the source was shared. Two lines of evidence are given and described below supporting this.

Given that analysis of the zircon spectra was largely qualitative, to better support the claim of a shared source, a quantitative method was employed. A Kolmogorov–Smirnov (KS) test is a non-parametric test which can be used as a goodness-of-fit test for two sample sets as it utilizes empirical cumulative distribution functions for each sample and can detect differences in the location and shape of the functions. It can produce a measure of the probability that two populations of ages are identical. A probability value (P) >0.05 indicates that the populations being compared are indistinguishable to the 95% confidence level where as <0.05 indicates that the hypothesis that two populations are identical is rejected (Press et al., 1988). Schmitt et al. (2010) conducted KS analysis on zircon populations of lavas from arc volcanoes and following their methods. When KS statistics are applied to the zircon populations from the domes of this study, all are above a probability of 0.05 indicating that all of the zircon populations, when compared to each other, are indistinguishable to a 95% confidence level. The probability values range from 0.05 to as high as 0.91, with an average of 0.34 (Table 21). Putting this into context, Schmitt et al. (2010) analyzed populations of zircons separated from the same lava and this yielded a P of 0.27. Thus, these KS statistics support more qualitative methods in supporting the hypothesis that the domes of this study originated from the same source.

Table 21. KS Probabilities of comparison between zircon populations from two given domes. KS statistics are a measure of the probability that two populations of ages are identical. A probability value (P) >0.05 indicate that the populations being compared are indistinguishable to the 95% confidence level.

Domes	Probability (P)
Chao-Chillahuita	0.72
Chao-Tocopuri	0.91
Chao-Chanka	0.07
Chao-Chascon	0.42
Chillahuita-Tocopuri	0.45
Chillahuita-Chanka	0.09
Chillahuita-Chascon	0.15
Tocopuri-Chanka	0.05
Tocopuri-Chascon	0.17
Chanka-Chascon	0.33
Average	*0.34*

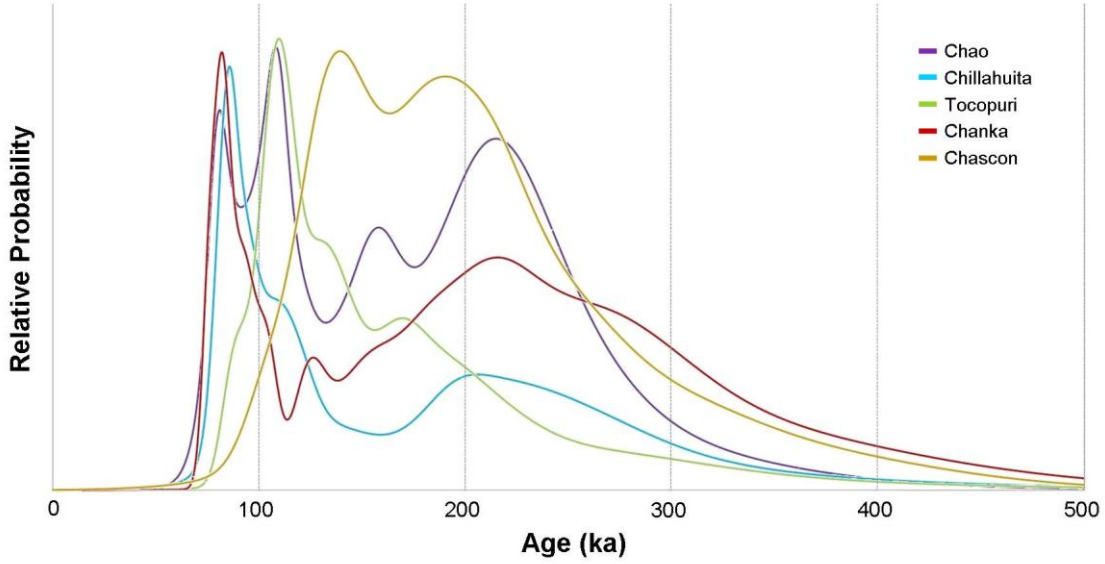

Figure 23. Overlain comparison of PDPs from all five domes. Note the strong resemblance to each other and the presence of shared pulses at ~90, ~110, and ~220 ka.

A more qualitative but less abstract method of comparing the zircon age populations of the domes is utilized by comparing the PDP age spectra of the domes (Figure 23). The spectra from all five of the domes share a series of lesser peaks in the spectra in addition to two larger more dominant peaks. In four of the five domes, with the exception of Chascon, a large peak is shared whose crest ranges from ~80 to 110 ka and another large peak which is broader and less defined, but includes Chascon, has crests ranging from ~175 to 220 ka (190 to 220 ka if Tocopuri is not included). The underlying reasoning that these pulses are similar but not exactly consistent in age and distribution is both a function of the statistical distribution of zircon within a given chamber and also the manner by which they form and what they represent. Simply put, a peak in the PDP zircon age spectra represents a period in time where a higher proportion of zircon was crystallizing. This leads to a discussion of the conditions of the zircon growth and retention within a magma body.

Discussions on the set of criteria determining what a magma "chamber" is exist (i.e. Hildreth, 2004; Bachmann and Bergantz, 2004) , however, the mechanical make-up of the magma system is beyond the scope of this study. If the source is in fact a "chamber" or as suggested by Hildreth (2004) for the Long Valley system, a 'plexus of dikes, pods, and mushy differentiated intrusions, where ductile deformation promotes extraction, aggregation and blending of varied melts' is somewhat irrelevant in this study. What this study will assert is that the upper-crustal zone under these lava domes is strongly connected, relatively homogenous and long-lived body of magma or mush.

7.3 Conditions of zircon grown and retention

Zircon often forms as an accessory phase in magmas. However, in order for zircon to form or remain stable in the magma it must be zircon saturation by meeting the requisite temperature and zirconium concentrations for a given cation ratio (M, defined as (Na+K+2Ca)/(Al*Si)). If it is not stable, it will begin to dissolve. Watson and Harrison (1983) conducted a detailed study of zircon saturation in silicic melts and created a simple model to address conditions of zircon formation based on whole-rock or glass chemistry in addition to temperatures (Figure 24). If the melt is not saturated with respect to Zr, zircon can dissolve in just 1000s of years depending on the size of the zircon crystal and the temperature and diffusivity of the host melt (Reid et al., 1997; Watson and Harrison, 1983). When the model is applied to the lavas of these domes, using XRF and ICP-MS chemistry from this study along with the Ghiorso and Evans (2010) model for magma temperature, the results reveal that the magma which fed these domes was very near the zircon saturation point (Figure 24).

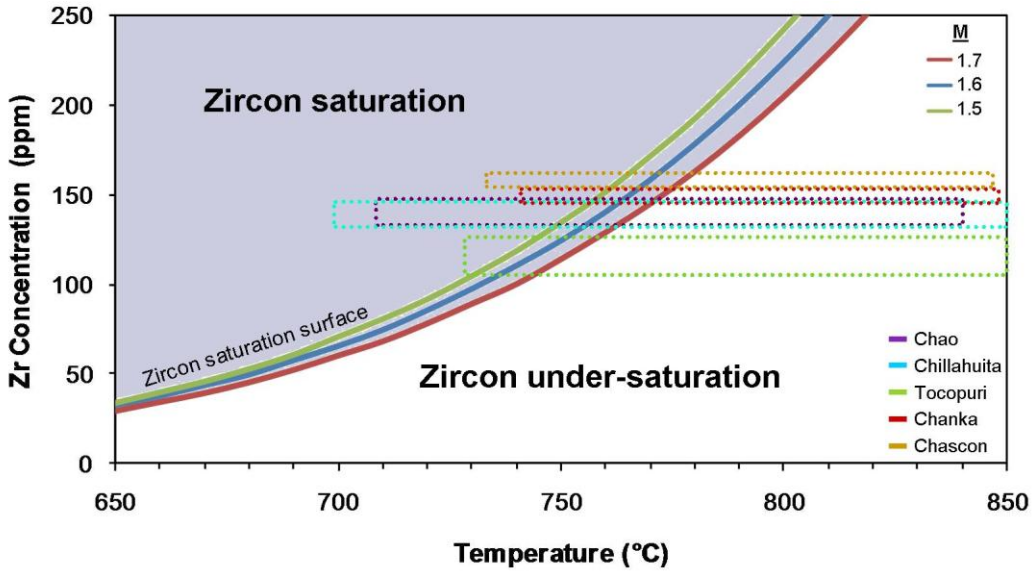

Figure 24. Graph illustrating the conditions of zircon saturation and under-saturation as a function of Zr concentration and temperature. Based in part on the cation ratio of the magmas (M; defined as (Na+K+2Ca)/(Al*Si)). Range of conditions for each dome are shown by the colored boxes.

Additional to the temperature and concentration requirements to crystallize zircon, the diffusivity in the magma must be adequate to transport chemical components for further crystallization of the zircon. This has implications for the formation and preservation of the pulses in zircon crystallization observed in the spectra of these domes.

The magma body that these domes originated from was large and given its extreme crystal-rich nature and textural maturity, it was likely a body of crystal mush in most places -- with perhaps pockets of more fluid magma (i.e. Hildreth, 1981; Bachmann et al., 2004). Given the lower temperatures and diffusivities of crystal-mush, zircon would have a difficult time crystallizing in these areas and these conditions could lead to the preservation of previous periods of zircon crystallization. Additionally, another potential mechanism that could preserve the older zircon crystallization age is the

encapsulation by other mineral phases that overgrew the zircon crystals (i.e. Miller et al., 2007)

Regardless of the mechanism the fact remains that the data demonstrate that older zircons are preserved. A related question that need to be further explored is how there are distinct populations (pulses) of crystallization occurring in the magma chamber. It is known that in large systems such as this, mafic recharge is vital in the longevity and eventual eruption of the magma body (e.g. Hildreth, 1981). Furthermore, it is known from the presence of the mafic enclaves in the domes that mafic injection and recharge is and likely has been occurring in the magma chamber that formed these domes; and also that mixing (convective or otherwise) of these mafic magmas with the host magma and mush has been occurring over a wide area. Data from the mafic enclaves shows that they are hotter than the host body. Therefore, increases or pulses in the amount of mafic magma being added to the chamber would raise the temperature of the cooler silicic magma. This subsequent rise in temperature and thus diffusivity would lead to a reinvigoration in zircon crystallization for a period of time following the pulse.

However, the temperature rise associated with the mafic injection could not have been large enough to sufficiently heat the entire chamber, otherwise older growth on zircon would be overprinted by newer growth and thus older ages would not be preserved.

Therefore, the pulses were only felt by proportion of the magma chamber, leaving older areas of mush unaffected. These periods or pulses in mafic injection and zircon crystallization reinvigoration are represented by the peaks in the zircon age PDP spectra. Multiple peaks are seen in the spectra, indicating that numerous pulses in mafic injection likely occurred and were felt over the entire spatial extent of the chamber. Older pulses were preserved in areas of mush that did not feel the subsequent pulses.

7.4 Magmatic residence time

The nature of magmatic residence time in large silicic systems has been a frequent subject of debate among. While some studies argue for extended residence times in large silicic systems (e.g. Reid et al., 1997; Brown and Fletcher, 1999; Bachmann and Bergantz, 2004), other studies have pushed for much briefer residence times (e.g. Reid and Coath, 2000; Charlier et al., 2005). Furthermore, quite often the evidence used for both conclusions is largely the same (e.g. Brown and Fletcher, 1999 vs Charlier et al., 2005). As a result of this ongoing debate, a primary research objective of this study was to determine how long the magma which fed these domes was present in the crust before eruption (i.e. magmatic residence time); with the hypothesis that the residence time of the magmas was extended and well over 100 kyr.

As suggested in the previous chapter, the distribution of zircon ages is interpreted by this study to suggest that the residence time of the magma body was extended. The PDP and distribution of ages, both of the individual domes and the composite, does not show a gap significant enough to where the PDP relative probability falls near zero or where the age error bars are not strongly overlapping from eruption age until at minimum >275 ka (Figure 25). However, this hypothesis once again brings up some questions and resistances that must be addressed.

A similar zircon spectra to what is seen in this study has been observed for the Taupo system and interpreted in differing ways. Brown and Fletcher (1999) pointed to extended PDP spectra as evidence for extended residence while Charlier et al. (2005) used the same spectra to argue for short residence of the erupted magma with assimilation of older semi-solid mushes being responsible for the older portions of the spectra. To some degree both may be true. However, while debate does exist on how exactly to classify a magma chamber or residence time, what this study will assert is that zircon was continuously being crystallized somewhere in this body since at least 275 ka. Further supporting this idea, this crystallization was felt by five domes that cover a wide spatial area. In order for the same populations to be incorporated over

this wide area there must have been a continuously present magmatic body over a wide spatial extent and not just remobilization of mush or frozen plutons.

A last thing of note, the estimate for residence time serves as a minimum. In reality, the residence time of the magma was likely longer because this estimate is a function of the zircon ages and their temporal continuity. If magma was present, but no zircon was crystallizing due to unfavorable (e.g. under-saturated) conditions, no zircons exist to extend our estimate due to lack of a continuous population. Additionally, if older zircon were overprinted by younger crystallization, this also could cause a lack of temporal continuity in the population. Regardless of the mechanism, zircon population continuity is not seen past ~275 ka and thus from eruption to this time remains the minimum estimate of residence time for this magma body.

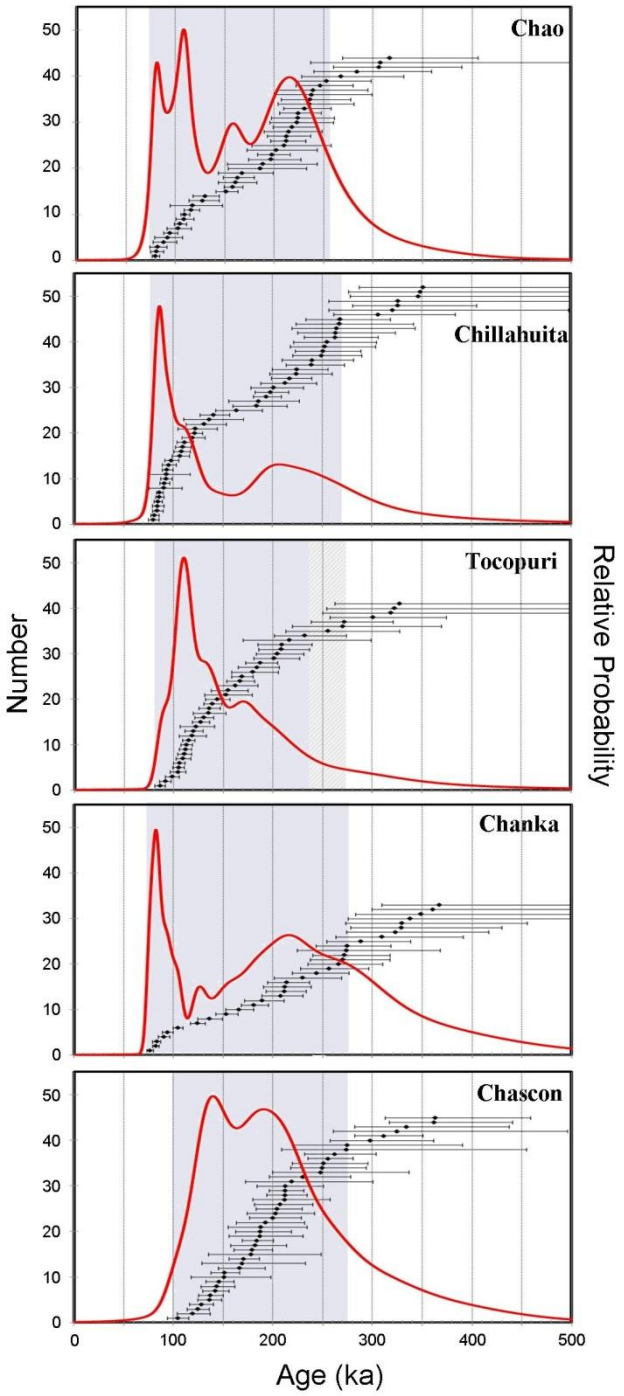

Figure 25. Comparison of the estimated residence time of the magmas for each dome. Based off the continuity of the zircon ages and spectra. Number is number of zircon rim analyses. The red curves are the probability density lines. The gray bar is the extent of the ‘continuous’ zircon population.

7.5 Implications for the APVC

Thus far these domes have been linked to one another through data that suggests a large and long-lived upper-crustal body of mush and magma. However, taking a large step out in scale, the data also leaves little doubt that these domes are a continuation of the APVC. Establishing this point has important implications as these domes are the youngest volcanic manifestation of the system. Their relative youth lends a unique opportunity to probe the evolution and recent state of the overall system.

The first question that must be addressed is what exactly does the eruption of these domes indicate about the state of the magmatic system below? Since the last major pulse in volcanism in the APVC at around 4 to 3 Ma, the system has shown a waning and relative paucity in volcanic products (Figure 3). The natural question is whether these domes represent a rejuvenation of the APVC and perhaps the onset of a new pulse of volcanism or, on the other hand, do they represent the last gasps of a largely dying system. While this question may be impossible to answer conclusively, a few lines of evidence can give some indication. First, the low volume of volcanic products through time since the last major pulse at 4 to 3 Ma represents the largest such temporal gap between pulses since the onset of the APVC; the Pastos Grandes Ignimbrite (2.89 Ma) represents the last major eruption in the vicinity of these domes. Furthermore, this trend parallels that of other large scale silicic systems (e.g. Southern Rocky Mountain Volcanic Field) which shows a similar waning of volcanic products before the system ceased completely (Figure 3). Second, despite the periodic but ongoing injection of mafic magmas, the advanced textural maturity of the magmatic source of these domes suggests that body may be nearing rheological lock-up and approaching the solidus. Lastly, the presence of antecrystic zircon interiors (dating to ~3.5 Ma) indicates that at no point since the formation/incorporation of these interiors did the conditions in the magma reach a point unfavorable to the existence of zircon

for an extended period of time, as zircon will dissolve in >1000 years in zircon undersaturated magmas (Harrison and Watson, 1983). Additionally, the further crystallization, evident from younger rims around antecrystic interiors, indicates that these older zircon where not just simply incorporated on the host magma en route to the surface.

The presence and ages of these zircon antecrystic interiors brings up another important observation that must be addressed. The lack of older ages found in antecrystic zircon interiors indicate that magmatic activity in this area of the APVC dates at minimum back to ~3.5 Ma. However, this is inconsistent with the surface record of volcanism which shows numerous eruptions dating back much further over 10 Ma (de Silva, 1989; Salisbury et al., 2011). In fact, the most volcanically prolific part of the APVC record is older than this 3.5 Ma cut-off. This lack of any zircon population past 3.5 Ma, despite an active volcanic and thus plutonic system, suggests that either no zircon crystallization was taking place or that older zircon were thermally resorbed by younger magmas that were hotter and zircon-undersaturated. However, the presence of zircon in volcanic products predating 3.5 Ma (7.8 Piedras Grandes Domes; zircons from own separations) suggesting that crystallization of zircon was indeed taking place in the older magmas, indicating that thermal resorbtion of older zircons in the likely reason for their absence in these domes. This is further supported by the lack of a xenocrystic zircon population despite zircon-rich regional bedrock (Schmitt et al., 2003). These lines of evidence suggest that only since about 3.5 Ma have favorable conditions existed for an extended period of time, allowing for the survival of the antecrystic interiors. The presence of younger zircon crystallization onto the antecrystic interiors indicates that the interiors were not merely assimilated by ascending magmas.

These lines of evidence combine to suggest that these domes may only be a variation from the overall waning trend of APVC volcanic system since 3-4 Ma and do not necessarily indicate that the system is rejuvenating in this region of the APVC.

However, future large-scale system rejuvenation is certainly within the realm of possibility for the APVC, and even with a waning trend future eruptions in the APVC are possible, if not likely.

The APVC has been active for more than 10 million years with a wide spatial distribution (de Silva 1989; Salisbury et al., 2011) and the crust in this region is likely largely composed of an amalgamation of plutons and batholiths which mark past magmatic and volcanic activity. Given that the overall consolidation of these older bodies is not uniform, local differences are expected over an area as wide as the proposed magmatic body of this study covers. This point is exemplified by the Chascon-Runtu Jarita domes, which formed within the 2.6 Ma Pastos Grandes caldera causing the magma body in this area to undoubtedly record the effects of intrusion into, and likely assimilation, of the Pastos Grandes pluton. Indeed, evidence of this interaction exists as assimilated blocks of granitic pluton were brought to the surface by ascending magmas. Dating on zircon rims and interiors found within these granitic blocks shows crystallization ages clustering slightly younger (2.34 to 2.80 Ma) than the eruption of the Pastos Grandes ignimbrite (2.89 Ma; from Salisbury et al., 2011). One interior age is older than the eruption (3.18 Ma). These zircons likely represent the solidification of the remnant magmas left after the eruption of the primary ignimbrite eruption into a pluton. No plutonic inclusions were found within the other domes. This is likely a reflection of the local differences in crust.

The formation of the Pastos Grandes magmas into a pluton is analogous to what is likely occurring within the magma body that fed the domes. While the magma body may have at one time been on track to erupt as a large ignimbrite similar to Pastos Grandes, for unknown reasons it at some point deviated and the eruption did not occur. Now, the advanced textural maturity of the magmas indicate that this system may as well be approaching solidification and will soon share the same fate as the left over Pastos Grandes magmas and form into a large upper crustal pluton or batholith.

Thus it may also be suggested that these domes may be the last gasps from this magma body and without significant mafic input it may no longer be able to erupt. With that in mind, these domes may represent the mapping of a forming upper-crustal batholith.

7.6 Overall Model

The results and discussion of this study integrated into a model for these domes which attempts to incorporate all of the data and observations from these domes both in context with each other and also the overall APVC system (Figure 26).

Before the magma that eventually formed the domes was emplaced, the upper crust in this part of the APVC was likely an amalgamation of plutonic bodies from previous episodes of magmatism and volcanism over the >10 Ma life of the APVC magmatic system; in addition to pre-APVC crust (Figure 26A). Starting prior to 275 ka, a large body of magma was emplaced into the crust, however, this magma was zircon under-saturated and thus no zircon were crystallized until the temperature decreased and eventually lead to favorable conditions for zircon growth starting around 275 ka (Figure 26B). As the body continued to cool, zones of crystal mush formed within the magma chamber and the edges of the chamber approached the solidus. Pulses of more mafic magma from a lower source were occasionally injected into the chamber. These pulses, felt throughout the chamber, kept the chamber viable and lead to the reinvigoration of zircon grown for a period of time. The pulses were recorded by zircon crystals which experienced growth shortly after the pulse, but failed to experience growth after the effects of the pulse had waned; likely due to entrapment in a crystal mush zone or a host phenocryst of another phase. Multiple pulses of mafic injection occurred and were recorded by the zircon, but in the intermittent time between the pulses zircon continued to crystallized in melt-rich magma, which was present throughout the extent of the magma chamber in variable amounts (Figure 26C). Eventually, an injection of mafic magma occurred causing a short, yet intense, period of zircon growth and then likely causing of the eruption of the lava domes. The

Chascon-Runtu Jarita domes were erupted first as evidenced by the older zircon age spectra and the higher proportion of unmixed mafic magma. Following the eruption of Chascon, the four other domes were erupted in close succession (Figure 26D). After the eruption of these domes (given the textural maturity of the source) the magma source appears to be nearing rheological lock-up and eventual solidification into a large pluton or batholith. However, potential for future eruptions does exist and is likely a function of the continuation and intensity of mafic injection into the chamber to serve as both an eruption trigger and allowing the chamber to stay viable.

Figure 26. Model of the source magma body through time. A) Upper-crust of the APVC region is an amalgamation of older APVC plutonic bodies. B) Injection of magma into the crust. C) Cooling of the magma body to produce significant areas of crystal mush and allowing for the crystallization and entrapment of zircon crystals. Pulses of mafic injection are responsible for the reinvigoration of zircon crystallization and continued viability of the magma body. D) Eventually, the domes are erupted very closely in time. Eruption is likely due to a spike in mafic injection.

Zones within the magma chamber described in the legend are based of Miller et al. (2007). Colors of the zircon are based off age and source.

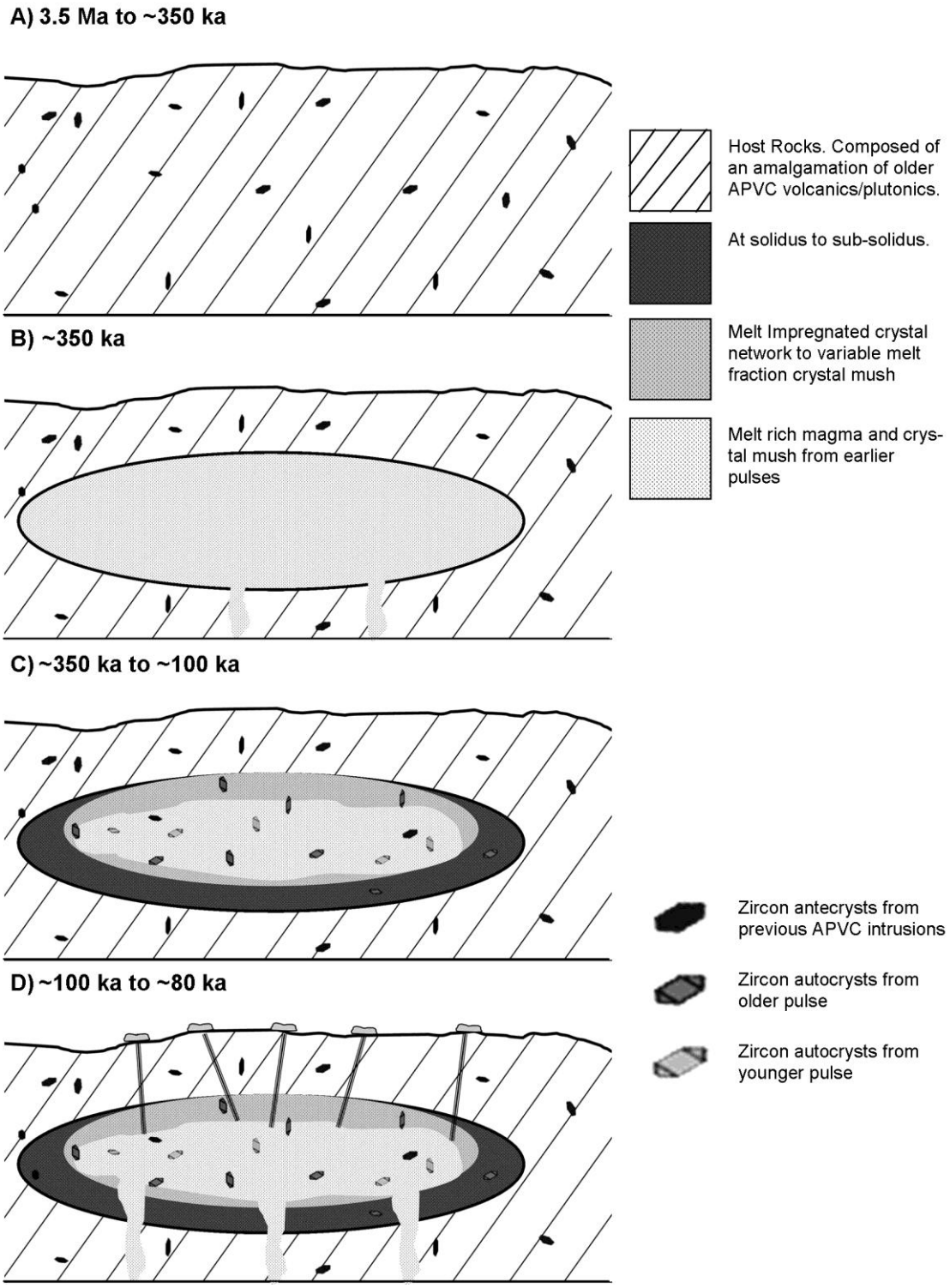
A) 3.5 Ma to ~350 ka
B) ~350 ka
C) ~350 ka to ~100 ka
D) ~100 ka to ~80 ka
Host Rocks. Composed of an amalgamation of older APVC volcanics/plutonics.
At solidus to sub-solidus.
Melt Impregnated crystal network to variable melt fraction crystal mush
Melt rich magma and crystal mush from earlier pulses
Zircon antecrysts from previous APVC intrusions
Zircon autocrysts from older pulse
Zircon autocrysts from younger pulse

8.0 Conclusions

A series of research goals and questions were asked at the beginning of this study. With the overall goal of understanding the evolution and timescales of the magmatic system, these questions included the relative source of the domes, the longevity of magma residence in the crust, and what the eruption of these domes represents for the overall APVC system. Working towards answering those questions through the interpretation and integration of the multiple analytical approaches, this research has produced a number of significant conclusions as to the construction, architecture, and history of the magmatic system that produced these domes.

1) The first objective of the study was to determine if the magma that fed these domes evacuated from distinct batches of magma or a larger shared source. The hypothesis that the domes were evacuated from a large regional shared source was developed in part from previous studies which noted the strong similarities between the domes.

The findings of this study support and build on previous studies that the domes, despite being separated by as much as 80 km, share a large upper-crustal source which, given its size and longevity, is likely in large part a body of crystal mush. Evidence for this conclusion comes from the striking petrochemical similarity of the domes to one another, the presence of a synchronous zircon spectra and crystallization history; seen both in the strength of the KS statistics and the presence of multiple shared peaks in the PDP spectra. Given this evidence, and the domes close proximity in eruption age, it is reasonable that these domes represent a distinct temporal eruptive pulse from a large upper-crustal magma body which was likely triggered by mafic injection into the system.

2) A second objective of this study was to determine how long the magma was present in the crust before eruption (i.e. magmatic residence time). The topic of residence time had been a hotly debated subject, however recent studies hinted at extended (>100 kyr) periods of residence in similar large silicic systems. Therefore, the hypothesis for this study mirrored this in suggesting that the residence time of the magmas was extended and well over 100 kyr.

The findings of this study ultimately supported this hypothesis and indicate that the magmas which fed these domes experienced extended residence in the system from eruption to a minimum of ~275 ka, for a minimum residence of >175 kyr. Primary evidence for this conclusion is the continuity of zircon crystallization age populations of all of the domes dating to this point. After 275 ka, the zircon population can no longer be considered continuous. While magma may very likely have been present prior to this age, we cannot say definitively, causing this age only represent a minimum.

3) The final objective of this study was to identify what the eruption of these domes represents for the overall APVC system. Previous studies have shown that the APVC currently has an overall waning trend since peak flare up at around 3-4 Ma. Thus the hypothesis developed from this study was, despite the eruption of these domes, our data would support previous findings suggesting that the APVC is overall a waning system.

Our findings show given the petrochemical similarity of the domes to the ignimbrites of the APVC, there is little doubt they are a continuation of the APVC system. However, the eruption of the domes, in isolation, does not mean that the system is rejuvenating and priming for potential future pulses or large-scale eruptions in this region of the system. Evidence for this conclusion comes from the overall system waning since 4 Ma, the textural maturity of the lavas, and the presence of zircon

antecrysts dating several Ma. Thus, these domes likely represent a variation from the overall waning trend of the APVC. However, given that mafic injection is inferred throughout the magmatic history of these domes and is likely still ongoing, the APVC magmatic system is still active. Furthermore, despite the waning trend, as long as the system remains active, potential for future eruptions remains and may even be considered likely.

References Cited

Abot, M., 2010. Amphibole-Plagioclase P-T estimates for the Altiplano Puna Volcanic Complex (M.S. Thesis), Oregon State University.

Allmendinger, R.W., Jordan, T.E., Kay, S.M., Isacks, B.L., 1997. The evolution of the Altiplano–Puna plateau of the Central Andes. Annual Reviews of Earth and Planetary Science 25, 139–174.

Andersen J.L., Lindsley D.H., 1988. Internally consistent solution models for the Fe-Mg-Mn-Ti oxides, Fe-Ti oxides. American Mineralogist 73,714-726

Bachmann, O., Dungan, M.A., Lipman, P.W., 2000. Voluminous lava-like precursor to a major ash-flow tuff: low-column pyroclastic eruption of the Pagosa Peak Dacite, San Juan volcanic field, Colorado. Journal of Volcanology and Geothermal Research 98, 153-171.

Bachmann, O., Bergantz, G.W., 2004. On the origin of crystal-poor rhyolites: extracted from batholithic crystal mushes. Journal of Petrology 45, 1565–1582.

Bachmann, O., Miller, C.F., de Silva, S.L., 2007. The volcanic–plutonic connection as a stage for understanding crustal magmatism. Journal of Volcanology and Geothermal Research 167, 1–23.

Bachmann, O., Oberli, F., Dungan, M.A., Meier, M., Mundil, R., Fisher, H., 2007b. 40Ar/39Ar and U–Pb dating of the Fish Canyon magmatic system, San Juan Volcanic field, Colorado: Evidence for an extended crystallization history

Bacon, C.R., Hirschmann, M.M., 1988. Mg/Mn partitioning as a test for equilibrium between coexisting Fe-Ti oxides. American Mineralogist 73, 57-61

Best, M.G., Christiansen, E.H., 1991. Limited extension during peak Tertiary volcanism, Great Basin of Nevada and Utah. Journal of Geophysical Research 96 (B8), 13509-13528.

Bourdon, B., Worner, G., Zindler, 2000. U-series evidence for crustal involvement and residence times in the petrogenesis of Parinocota volcano, Chile. Contributions to Mineralogy and Petrology 139, 458-469.

Brown, S.J.A., Fletcher, I.R., 1999. SHRIMP U–Pb dating of the preeruption growth history of zircons from the 340 ka Whakamaru Ignimbrite, New Zealand: Evidence for N250 k.y. magma residence times. Geology 27 (11), 1035–1038.

Charlier, B.L.A., Wilson, C.J.N, Lowenstern, J.B., Blake, S., Van Calsteren, P.W., Davidson, J.P., 2005. Magma generation at a large, hyperactive silicic volcano (Taupo, New Zealand) revealed by U–Th and U–Pb systematics in zircons. Journal of Petrology 46 (1), 3–32.

Charlier, B.L.A., Bachmann, O., Davidson, J.P., Dungan, M.A., Morgan, D.J., 2007. The upper crustal evolution of a large silicic magma body: evidence from crystal-scale Rb-Sr isotopic heterogeneities in the Fish Canyon Magmatic System, Colorado. Journal of Petrology 48 (10), 1875-1894.

Chmielowski, J., Zandt, G., Haberland, C., 1999. The central Andean Altiplano–Puna magma body. Geophysical Research Letters 26, 783–786.

Christensen, J.N., DePaolo, D.J., 1993. Timescales of large volume silicic magma systems: Sr isotopic systemactics of phenocrysts and glass from the Bishop Tuff, Long Valley, California. Contributions to Mineralogy and Petrology 113, 100-114.

Coira B.L., Davidson J., Mpodozis C., Ramos V.A., 1982. Tectonic and magmatic evolution of the Andes of northern Argentina and Chile. Earth Science Review 18, 303-332

Coira, B., Mahlburg-Kay, S., Viramonte, J., 1993. Upper Cenozoic magmatic evolution of the Argentine Puna—a model for changing subduction geometry. International Geological Review 35, 677–720.

Davies, G.R., Halliday, A.N., Mahood, G.A., Hall, C.M., 1994. Isotopic constraints on the production rates, crystallization histories and residence times of pre-caldera silicic magmas, Long Valley, California. Earth and Planetary Science Letters 125, 17–37.

de Silva, S.L., 1987. Explosive Silicic Volcanism in the Central Andes. Ph.D. dissertation, Open University, Milton Keynes, UK., pp. 465.

de Silva, S.L., 1989. Geochronology and stratigraphy of the ignimbrites from the 21°30′S to 23°30′S portion of the Central Andes of northern Chile. Journal of Volcanology and Geothermal Research 37, 93–131.

de Silva, S.L., Francis, P.W., 1991. Volcanoes of the Central Andes. Springer-Verlag, New York.

de Silva, S.L., Self, S., Francis, P.W., Drake, R.E., Carlos Ramirez, R., 1994. Effusive silicic volcanism in the Central Andes: the Chao dacite and other young lavas of the Altiplano–Puna Volcanic Complex. Journal of Geophysical Research 99 (B9), 17805–17825.

de Silva, S.L., Zandt, G., Trumbull, R., Viramonte, J., 2006a. Large scale silicic volcanism—the result of thermal maturation of the crust. In: Chen, Y.-T. (Ed.), Advances in Geosciences.World Scientific Press, pp. 215–230.

de Silva, S.L., Zandt, G., Trumbull, R., Viramonte, J.G., Salas, G., Jimenez, N., 2006b. Large Ignimbrite Eruptions and Volcanotectonic Depressions in the Central Andes — A Thermomechanical Perspective. In: de Natale, G., Troise, C., Kilburn, C. (Eds.), Mechanisms of activity and unrests at large calderas. Special Publication by Geological Society of London 269, pp. 47–63.

de Silva, S.L., Gosnold,W., 2007. Cordilleran Batholith development: insights from an ignimbrite flare-up. Journal of Volcanology and Geothermal Research 167, 320–335.

Ducea, M.N., 2001. The California Arc; thick granitic batholiths, eclogitic residues, lithospheric-scale thrusting, and magmatic flareups. GSA Today 11 (11), 4–10.

Dietterich, H., de Silva, S., 2010. Sulfur yield of the 1600 eruption of Huaynaputina, Peru: Contributions from magmatic, fluid-phase, and hydrothermal sulfur. Journal of Volcanology and Geothermal Research 197, 303-312.

Dunne, J.A. 1998. Calibration of the method of exposure dating of geomorphic surfaces on the earth using in-situ-Produced cosmogenic radionuclides, and applications in the central Andes. Phd Thesis. Purdue University.

Evans, B.W., Scaillet, B., 1997. The redox state of Pinatubo dacite and the ilmenite–hematite solvus. American Mineralogist 82 (5–6), 625–629.

Folkes, C.B., 2010. The geochemistry, stratigraphy and volcanology of the Cerro Galán caldera system, NW Argentina. PhD Thesis. Monash University

Gansser, A.,1973 Facts and theories on the Andes. Journal of the Geological Society of London 129, 93-131

Ghiorso, M.S., Evans, B.W., 2008. Thermodynamics of rhombohedral oxide solid solutions and a revision of the FE-TI two-oxide geothermometer and oxygenbarometer. American Journal of Science 308 (9), 957–1039.

Gregory-Wodzicki, K.M., 2000. Uplift history of the Central and Northern Andes: A review. Geological Society of America Bulletin 112, 1091-1105

Halliday, A.N., Mahood, G.A., Holden, P., Metz, J.M., Dempster, T.J., Davidson, J.P., 1989. Evidence for long residence times of rhyolitic magma in the Long Valley magmatic system: the isotopic record in precaldera lavas of Glass Mountain. Earath and Planetary Science Letters 94, 274-290

Harrison, T.M., Watson, E.B. 1983. Kinetics of Zircon Dissolution and Zirconium Diffusion in Granitic Melts of Variable Water Content. Contributions to Mineralogy and Petrology 84, 66-72.

Harrison, M.T., Blichert-Toft, J., Muller, W., Alberede, F., Holden, P., Mojzsis, S.J., 2005. Heterogeneous Hadean Hafnium: Evidence of Continental Crust at 4.4 to 4.5 Ga. Science 23, vol. 310 no. 5756, 1947-1950.

Heumann, A., Davies, G.R., Elliott, T., 2002a. Crystallization history of rhyolites at Long Valley, California, inferred from combined U-series and Rb-Sr isotope systematic. Geochimica et Cosmochimica Acta, 66 (10), 1821-1837.

Hildreth, W., 1981. Gradients in silicic magma chambers: Implications for lithospheric magmatism. Journal of Geophysical Research 86 (B11), 10153–10192.

Hildreth, E.W., 2004. Volcanological perspectives on Long Valley, Mammoth Mountain, and Mono Craters: several contiguous but discrete systems. Journal of Volcanological and Geothermal Research 136, 169–198.

Hora, J.M., Singer, B.S., Jicha, B.R., Beard, B.L., Johnson, C.M., de Silva, S.L., Salisbury, M., 2010. Volcanic biotite-sanidine $^{40}Ar/^{39}Ar$ age discordances reflect Ar partitioning and pre-eruption closure in biotite. Geology 38, 923-926.

Hyneck, S.A., Brown, F.H., Fernandez, D.P., 2011. A rapid method for hand picking potassium-rich feldspar from silicic tephra. Quaternary Geochronology 6, 285-288.

Irvine, T.N., Baragar, W.R.A., 1971. A guide to the chemical classification of the common volcanic rocks. Can. Jour. Earth Sc. 8, 523-546.

Isacks, B.L., 1988. Uplift of the central Andean plateau and bending of the Bolivian orocline. Journal of Geophysical Research 93, 3211–3231.

James, D.E., 1971a. Plate tectonic model for the evolution of the Central Andes. Geological Society of America Bulletin 82, 3325-3346.

James, D.E., 1971b. Andean crustal and upper mantle structure. Journal of Geophysical Research 76, 3246-3271.

Johnson, D.M., Hooper P.R., Conrey, R.M.,1999. XRF analysis of rocks and minerals for major and trace elements on a single low dilution Li-tetraborate fused bead**.** Advances in X-ray Analysis 41, 843-867.

Jordan, T.E., Isacks, B.L., Allmendinger, R.W., Brewer, J.A., Ramos, V.A., Ando, C.J., 1983. Andean tectonics related to geometry of the subducted Nazca plate. Geological Society of America Bulletin 94, 341-361.

Kay, S.M., Mpodozis, C., Coira, B., 1999. Magmatism, tectonism and mineral deposits of the Central Andes (22°–33°S latitude). In: Skinner, B.J., Holland, R. (Eds.), Geology or Ore Deposits of the Central Andes. Society of Economic Geologists Special Publication, vol. 7, pp. 27–59.

Knaack, C., Cornelius, S., Hooper, P.R., 1994. Trace element analysis of rocks and minerals by ICP-MS. Open File Report, Department of Geology, Washington State University.

Knesel, K.M., Davidson, J.P., Duffield, W.A., 1999. Evolution of silicic magma through assimilation and subsequent recharge: evidence from Sr isotopes in sanidine phenocrysts, Taylor Creek Rhyolite, NM. Journal of Petrology 40, 773–786.

Kuno, H., 1968. Differentiation of basalt magmas, in Basalts, Hess, H.H. and Poldervaart, A., (Eds.), 2: 623-688, New York, Interscience.

Leidig, M., Zandt, G., 2003. Highly anisotropic crust in the Altiplano– Puna volcanic complex of the central Andes. Journal of Geophysical Research 108 (B1), 2014.

Lindsay, J.M., et al., 2001. Magmatic evolution of the La Pacana caldera system, Central Andes, Chile: Compositional variation of two cogenetic, large-volume felsic ignimbrites. Journal of Petrology 42 (3), 459–486.

Lipman, P.W., Steven, T.A., Mehnert, H.H., 1970. Volcanic history of the San Juan mountains, Colorado, as indicated by potassium-argon dating. Geological Society of America Bulletin 81, 2329–2351.

Lipman, P.W., 1984. The roots of ash-flow calderas in western North America: windows into the tops of granitic batholiths. Journal of Geophysical Research 89 (B10), 8801–8841.

Lipman, P.W., 2007. Incremental assembly and prolonged consolidation of Cordilleran magma chambers: Evidence from the Southern Rocky Mountain volcanic field. Geosphere 3, 42-70.

Lowenstern, J.B., Persing, H.M., Wooden, J.L., Lanphere, M., Donnelly-Nolan, J., Grove, T.L., 2000. U-Th dating of single zircons from young granitoid xenoliths: new tools for understanding volcanic processes. Earth and Planetary Science Letters 183, 291-302.

Mahood, G., Hildreth, W., 1983. Large partition coefficients for trace elements in high silica rhyolites. Geochimica et Cosmochimica Acta 47, 11-30

McDougall, I., Harrison, T.M., 1988. Geochronology and Thermochronology by the $^{40}Ar/^{39}Ar$ Method. Oxford Monographs on Geology and Geophysics No. 9. New York: Oxford University Press

Miller, J.S. Wooden, J.L., 2004. Residence, Resorption and Recycling of Zircons in Devil's Kitchen Rhyolite, Coso Volcanic Field, California. Journal of Petrology, 45, 2155-2170.

Miller J.S., Matzel, J.E.P., Miller, C.F., Burgess, S.D., Miller, R.B., 2007. Journal of Volcanology and Geothermal Research 167, 282-299.

Obradovich J.D ., 1992. Geochronology of the late Cenozoic volcanism of Yellowstone National Park and adjoining areas, Wyoming and Idaho. USGS Open-File Report 92-408

Paces, J.B., Miller, J.D., 1993. Precise U-Pb ages of Duluth Complex and related mafic intrusions, northeastern Minnesota – geochronological insights into physical, petrogenetic, paleomagnetic, and tectonomagnetic processes associated with the 1.1 Ga midcontinent rift system. Journal of Geophysical Research 98(B8), 13997-14013.

Perkins, M.E., Nash, W.P., Brown, F.H., Fleck, R.J., 1995. Fallout tuffs of Trapper Creek, Idaho—A record of Miocene explosive volcanism in the Snake River Plain volcanic province. Geol. Soc. Am. Bull. 107, 1484-1506.

Pouchou, L. J., Pichoir, F., 1984. New model quantitative x-ray microanalysis, Application to the analysis of homogeneous samples. Research in Aerospace 3, 13-38.

Press, W.H., Flannery, B.P., Teukolsky, S.A., Vetterling, W.T., 1988. Numerical Recipes in C: the Art of Scientific Computing. Cambridge University Press, New York. C: the Art of Scientific Computing. Cambridge University Press, New York.

Reid, M.R., Coath, C.D., Harrison, T.M., McKeegan, K.D., 1997. Prolonged residence times for the youngest rhyolites associated with Long Valley Caldera: 230Th–238U microprobe dating of young zircons. Earth and Planetary Science Letters 150, 27–39.

Reid, M., Coath, C., 2000. In-situ U-Pb ages of zircons from the Bishop Tuff; no evidence for long crystal residence times. Geology 28(5), 443-446.

Reid, M. R. 2003. Timescales of magma transfer and storage in the crust, *in Treatise on Geochemistry*, p. 167–193, Elsevier, New York.

Renne, P.R., Swisher, C.C., Deino, A.L., Karner, D.B., Owens, T.L., DePaolo, D.J., 1998. Intercalibration of standards, absolute ages and uncertainties in $^{40}Ar/^{39}Ar$ dating. Chemical Geology 145, 117-152.

Ridolfi, F., Renzulli, A., Puerini, M., 2010. Stability and chemical equilibrium of amphibole in calc-alkaline magmas: an overview, new thermobarometric formulations and application to subduction-related volcanoes. Contributions to Mineralogy and Petrology 160, 45-66.

Roobol, M.J., Francis, P.W, Ridley, W.L. Rhodes, M., Walker, G.P.L., 1974. Physico-chemical characters if the Andean volcanic chain, between latitudes 21° and 22° south. Paper presented at Symposium Internacional de Volcanologia, Int. Assoc. of Volcanol.and Chem, of Earth's Inter., Santiago, Chile, Sept. 9-14th, 1974.

Salisbury, M.J., Jicha, B., de Silva, S., Singer, B., Jiménez C., Ort, M., 2011. $^{40}Ar/^{39}Ar$ chronostratigraphy of Altiplano-Puna Volcanic Complex ignimbrites reveals the development of a major magmatic province. GSA Bulletin 123 (5-6) 821-840.

Schmitt, A.K., de Silva, S.L., Trumbull, R., Emmermann, R., 2001. Magma evolution in the Purico ignimbrite complex, northern Chile: evidence for zoning of a dacitic magma by injection of rhyolitic melts following mafic recharge. Contributions to Mineralogy and Petrology 140, 680–700.

Schmitt, A.K., Lindsay, J.M., de Silva, S.L., Trumbull, R., 2002. U–Pb zircon chronostratigraphy of early-Pliocene ignimbrites from La Pacana, north Chile: implications for the formation of stratified magma chambers. Journal of Volcanology and Geothermal Research 120, 43–53.

Schmitt, A.K, Grove, M., Harrison, T.M., Lovera. O., Hulen, J., Walters, M., 2003a. The Geysers-Cobb Mountain Magma System, California (Part 1): U-Pb zircon ages of volcanic rocks, conditions of zircon crystallization and magma residence times. Geochimica et Cosmochimica Acta 67(18), 3423-3442.

Schmitt, A.K., Grove, M., Harrison, T.M., Lovera, O., Hulen, J., Walters, M., 2003b. The Geysers-Cobb Mountain Magma system, California (Part 2): Timescales

of pluton emplacement and implications for its thermal history. Geochimica et Cosmochimica Acta 67(18), 3443-3458.

Schmitt, A.K., Stockli, D.F., Lindsay, J.M., Robertson, R., Lovera, O.M., Kislitsyn, R., 2010. Episodic growth and homogenization of plutonic roots in arc volcanoes from combined U-Th and (U-Th)/He zircon dating. Earth and Planetary Science Letters 295, 91-103.

Sempere, T., Herail, G., Oller, J., Bonhomme, M.G., 1990. Late Oligocene-Early Miocene major tectonic crisis and related basins in Bolivia. Geology 18(10), 946-949.

Sempere, T., Butler, R.F., Richards, D.R., Marshall, L.G., Sharp, W., Swisher, C.C., III. 1997. Stratigraphy and chronology of Upper Cretaceous-lower Paleogene strata in Bolivia and Northwest Argentina. Geological Society of America Bulletin 109, 709-727.

Smith, R.L., Bailey, R.A., 1968. Stratigraphy, structure, and volcanic evolution of the Jemez Mountains, New Mexico. Special Paper— Geological Society of America 447–448.

Smith, M.E., Singer, B., Carroll, A., 2003. $^{40}Ar/^{39}Ar$ geochronology of the Eocene Green River Formation, Wyoming. Geological Society of America Bulletin 155 (5), 549-565.

Sparks, R.S.J., Folkes, C.B., Humphreys, M.C.S., Barfod, D.N., Sunagua, M.C., McNutt, S.R., Pritchard, M.E., 2008. Uturuncu Volcano, Bolivia: volcanic unrest due to mid-crustal magma intrusion. American Journal of Science 308, 727-769.

Spencer, K.J., Lindsley, D.H., 1981. A solution model for coexisting iron-titanium oxides. American Mineralogist 66, 1189-1201.

Stormer, J.C., 1983. The effects of recalculation on estimates of temperature and oxygen fugacity from analyses of multi-component iron-titanium oxides. American Mineralogist 68, 586-594.

Sun, S.-s., McDonough, W.F. 1989. Chemical and isotopic systematic of oceanaic basalts: implications for mantle compositions and processes. Geological Society, London, Special Publications 1989, 42, 313-345.

Thorpe, R.S., Francis, P.W., 1979, Variations in Andean andesite compositions and their petrogenetic significance. Tectonophysics 57, 53-70.

Vazquez, J.A., Reid, M.R., 2002. Time scales of magma storage and differentiation of voluminous high-silica rhyolites at Yellowstone caldera, Wyoming. Contributions to Mineralogy and Petrology 144 (3), 274–285.

Walker, B.A., Grunder, A.L., Wooden, J.L., 2010. Organization and thermal maturation of long-lived arc systems: Evidence from zircon at the Aucanquilcha volcanic cluster, northern Chile. Geology 38 (11), 1007-1010.

Watson, E.B., Harrison, T.M., 1983. Zircon saturation revisited: temperature and composition effects in a variety of crustal magma types. Earth and Planetary Science Letters 64, 295-304.

Watson, E.B., 1996. Dissolution, growth and survival of zircons during crustal fusion: kinetic principles, geological models, and implications for isotopic inheritance. Special Paper, Geological Society of America 31, 43-56.

Watts, R.B., 1995. Evolution of the Cerro Chascon – Runtu Jarita complex in southwest Bolivia: implications for silicic dome formation. MS Thesis, Indiana State University.

Watts, R.B., de Silva, S.L., Jimenez de Rios, G., Croudace, I., 1999. Effusive eruption of viscous silicic magma triggered and driven by recharge: a case study of the Cerro Chascon–Runtu Jarita Dome Complex in Southwest Bolivia. Bulletin of Volcanology 61 (4), 241–264.

Zandt, G., Leidig, M., Chmielowski, J., Baumont, D., Yuan, X., 2003a. Seismic detection and characterization of the Altiplano–Puna magma body, central Andes. Pure and Applied Geophysics 160, 789–807.

APPENDICES

Appendix A: Petrographic Descriptions

09001CT: Chanka Silicic Lava

Major Minerals

Plagioclase (21%) – Range in size from .5mm to 3mm. Most are large and euhedral to subhedral in form. Complex twinning and zoning in the phenocrysts. Inclusions are common. A few look heavily altered/replaced.

Amphibole (7%) – 0.1 to 1.5mm in size. Euhedral form. Twinning and zoning common. Most have numerous small inclusions and some show minor alteration/replacement around the grain edges.

Biotite (9%) – 0.1 to 1.5mm in size, most in the 0.5mm area with a few much larger. Euhedral form. Inclusions common.

Quartz (5%) – 0.1 to 1mm in size, the majority fall around 0.5mm. Fractures commonly seen in the crystals. Resorption common on the edges of the grains.

Minor Minerals

Fe-Ti Oxides (2%) – Typically around 0.5mm or smaller with a few large grains over 1mm. Most show euhedral form.

Sanidine (Trace) – 0.1 to .5mm in size. Subhedral form. Simple twinning.

Sphene (Trace) – Typically around 0.5 mm in size or smaller. High relief.

Apatite (Trace) – Typically 0.1 to 0.5 mm in size. Subhedral form.

Groundmass (56%) – Groundmass consists of nearly equal parts colorless glass and microlite crystals. Vesicles are common. There is some evidence of flow seen in the alignment of the crystals.

Large glomerocrysts (>1mm) of smaller amphibole crystals (.1mm) are also common in the crystals, perhaps representing replaced pyroxene.

09002CT: Chanka Mafic Enclaves

Major Minerals

Plagioclase (16%) – Range in size from .5mm to 3mm. Most are large and euhedral in form. Complex twinning and zoning in the phenocrysts. Inclusions are common. Not in equilibrium with the matrix as evidenced by the common alteration/replacement seen in the crystals and especially on the edges.

Amphibole (4%) – 0.5 to 1mm in size. Subhedral form. Twinning and zoning common. Most have numerous small inclusions and some show significant alteration/replacement around the grain edges. Some crystals have been completely replaced.

Hypersthene (3%)— 0.5 to 1mm in size. Subhedral form. Often associated with cluster of plagioclase and other crystals.

Minor Minerals

Biotite (2%) – 0.5 to 1mm in size. Euhedral form. Inclusions common. Appear much less altered than the plagioclase or amphibole, but some minor alteration/replacement occurring along the edges of certain grains.

Quartz (2%) – 0.1 to .5mm in size. Fractures seen in the crystals. Resorption common on the edges of the grains. Occur mostly near the boundary of the mafic enclave and the host lava.

Groundmass (73%) – Groundmass consists mostly of microlites of the phenocrysts with minor amounts of glass and relatively very few vesicles.

09003CT: Chao Silicic Lava

Major Minerals

Plagioclase (24%) – Range in size from .5mm to 3mm. Euhedral to subhedral form. Complex twinning and zoning in the phenocrysts. Sieve, embayment, and replacement textures are common. Inclusions within the phenocrysts are also common.

Biotite (10%) – 0.1 to 1mm in size. Euhedral form. Much less alteration and replacement than seen in both the plagioclase and amphibole. Inclusions common.

Amphibole (7%) – 0.1 to 1mm in size. Euhedral to subhedral form. Twinning and zoning common. Alteration and replacement textures are prevalent, as are inclusions.

Quartz (5%) – 0.1 to 1mm in size, but most are on the larger end. Fractures commonly seen in the crystals. Resorption common on the edges of the grains.

Minor Minerals

Sanidine (1%) – 0.1 to .5mm in size. Subhedral form. Simple twinning. Alteration/Replacement common.

Fe-Ti Oxides (1%) – Typically around 0.5mm or smaller. Opaque in appearance. Often euhedral to subhedral in form.

Sphene (Trace) – Typically around 0.5 mm in size or smaller. High relief.

Apatite (Trace) – 0.1 to 0.5mm in size. Subhedral form. Occurs as inclusions.

Groundmass (52%) – Consists of mostly colorless glass. Microlites of the phenocrysts crystals are common. Vesicles are also common.

Glomerocrysts of smaller amphibole crystals (.1mm) are also seen.

09004CT: Chao Mafic Enclave

Major Minerals

Plagioclase (15%) – Range in size from .5mm to 2mm. Euhedral form. Complex twinning and zoning in the phenocrysts. Sieve, embayment, and replacement textures are common. Inclusions within the phenocrysts are also common. Some crystals look completely replaced.

Amphibole (4%) – 0.5 to 2mm in size. Euhedral to subhedral form. Twinning and zoning common. Alteration and replacement textures are very prevalent, as are inclusions.

Hypersthene (4%) – 0.5 to 1mm in size. Subhedral form. Often associated with cluster of plagioclase and other crystals.

Miner Minerals

Quartz (2%) – 0.1 to 0.5mm in size. Very few seen, heavily altered when seen and usually near boundary of mafic/host.

Biotite (1%) – 0.1 to 1mm in size. Euhedral form. Altered, but much less so than plagioclase or amphibole.

Fe-Ti Oxides (Trace) – Typically around 0.5mm or smaller. Most show euhedral form.

Groundmass (74%) – Made of mostly of small lathes of biotite and plagioclase. Glass and vesicles are also common.

Glomerocrysts of high biref minerals are also seen, perhaps pyroxene. Glomerocrysts are typically .5 to 1mm in size and are perhaps replaced plagioclase.

09005CT: Chao Crystal Rich Lava

Major Minerals

Plagioclase (25%) – Range in size from .1mm to 3mm. Euhedral form. Complex twinning and zoning in the phenocrysts. Sieve, embayment, and replacement textures are common around the edges of the crystals and sometimes in the cores. Inclusions are also common.

Biotite (10%) – 0.1 to 1mm in size. Tabular (rectangular) and Euhedral form. Inclusions common.

Quartz (7%) – 0.1 to 0.5mm in size, but most are on the larger end. Fractures commonly seen in the crystals. Resorption common on the edges of the grains.

Amphibole (6%) – 0.1 to 1mm in size. Euhedral to subhedral form. Alteration and replacement textures are prevalent, as are inclusions. In better shape than the plagioclase.

Minor Minerals

Sanidine (1%) – 0.1 to .5mm in size. Euhedral to subhedral form. Simple twinning.

Sphene (1%) – Typically around 0.5 mm in size or smaller. High relief.

Fe-Ti Oxides (1%) – Typically around 0.5mm or smaller. Opaque in appearance. Often euhedral to subhedral in form.

Apatite (Trace) – Seen as inclusions in the biotite. 0.1mm in size.

Groundmass (50%) – Consists of mostly colorless glass. Microlites of the phenocrysts crystals are common. Vesicles are also common.

Glomerocrysts of smaller amphibole crystals (.1mm) are also seen.

09006CT: Chao Pyroclastics

Major Minerals

Plagioclase (19%) – Range in size from .1mm to 2.5mm. Euhedral form. Complex twinning and zoning in the phenocrysts. Sieve, embayment, and replacement textures are common. Inclusions within the phenocrysts are also common.

Biotite (7%) – 0.1 to 1mm in size. Euhedral form. Inclusions common. Some look broken/fractured.

Amphibole (5%) – 0.1 to 1mm in size. With a few huge crystals over 2mm. Euhedral to subhedral form. Twinning and zoning common. Alteration and replacement textures are prevalent, as are inclusions.

Quartz (5%) – 0.1 to 1mm in size, but most are on the larger end. Fractures commonly seen in the crystals. Resorption very common on the edges of the grains.

Minor Minerals

Sanidine (1%) – 0.1 to .5mm in size. Subhedral form. Simple twinning. Alteration/Replacement common.

Sphene (1%) – Typically around 0.5 mm in size or smaller. High relief.

Fe-Ti Oxides (1%) – Typically around 0.5mm or smaller. Opaque in appearance. Often euhedral to subhedral in form.

Apatite (Trace) – Typically about 0.1mm in size. Subhedral form. Occurs as inclusions in biotite.

Groundmass (51%) – Consists of mostly colorless glass. Vesicles are also common.

09009CT: Chillahuita Silicic Lava

Major Minerals

Plagioclase (23%) – Range in size from .1mm to some very large 4mm+ crystals. Euhedral form. Complex twinning and zoning in the phenocrysts. Some show Sieve, embayment, and replacement textures. Inclusions are very common.

Biotite (10%) – 0.1 to 1mm in size. Euhedral form. Inclusions common very common. Some show reaction rims and what looks to be embayments.

Amphibole (6%) – 0.1 to 3mm in size. Euhedral to subhedral form. Inclusions very common. In better shape than most amphibole in these domes.

Quartz (6%) – 0.1 to 1mm in size. Fractures commonly seen in the crystals. Resorption common on the edges of the grains.

Minor Minerals

Sanidine (1%) – 0.1 to .5mm in size. Euhedral to subhedral form. Simple twinning.

Sphene (1%) – Typically around 0.5 mm in size or smaller. High relief.

Fe-Ti Oxides (1%) – Typically around 0.5mm or smaller. Opaque in appearance. Often euhedral to subhedral in form.

Apatite (Trace) – Typically about 0.1mm in size. Subhedral form. Occurs as inclusions in biotite.

Groundmass (53%) – Consists of mostly colorless glass with some vesicles and minor microlites.

Glomerocrysts of smaller plagioclase and amphibole crystals (.1 - .5mm) are also seen.

090011CT: Tocopuri Silicic Lava

Major Minerals

Plagioclase (25%) – Range in size from .1mm to some very large 5mm+ crystals. Euhedral form. Complex twinning and zoning in the phenocrysts. Some show Sieve, embayment, and replacement textures.

Biotite (9%) – 0.1 to 1mm in size. Euhedral form. Inclusions common very common. Some show reaction rims and disequilibrium textures but it really varies from crystal to crystal.

Quartz (7%) – 0.1 to 3mm in size. Fractures commonly seen in the crystals. Resorption common on the edges of the grains.

Amphibole (5%) – 0.1 to 3mm in size. Euhedral to subhedral form. Inclusions very common. In better shape than most amphibole in these domes.

Minor Minerals

Sanidine (1%) – 0.1 to .5mm in size. Euhedral to subhedral form. Simple twinning.

Sphene (1%) – Typically around 0.5 mm in size or smaller. High relief.

Fe-Ti Oxides (1%) – Typically around 0.5mm or smaller. Opaque in appearance. Often euhedral to subhedral in form.

Apatite (Trace) – Typically about 0.1mm to 0.2mm in size. Subhedral form. Occurs as inclusions in biotite.

Groundmass (52%) – Consists of mostly colorless glass with some vesicles.

09012CT: Tocopuri Darker Silicic Lava

Major Minerals

Plagioclase (24%) – Range in size from .1mm to some very large 5mm+ crystals. Euhedral form. Complex twinning and zoning in the phenocrysts. Some show Sieve, embayment, and replacement textures. Very broken-up appearance.

Biotite (10%) – 0.1 to 2mm in size. Euhedral form. Inclusions common very common. Reaction rims and disequilibrium textures common.

Quartz (7%) – 0.1 to 5mm in size. Fractures commonly seen in the crystals. Resorption common.

Amphibole (4%) – 0.1 to 2mm in size. Euhedral. Inclusions very common. In better shape than the biotite.

Minor Minerals

Sanidine (1%) – 0.1 to .5mm in size. Euhedral to subhedral form. Simple twinning.

Fe-Ti Oxides (1%) – Typically around 0.5mm or smaller. Opaque in appearance. Often euhedral to subhedral in form.

Sphene (Trace) – Typically around 0.5 mm in size or smaller. High relief.

Apatite (Trace) – Typically about 0.1mm to 0.2mm in size. Subhedral form. Occurs as inclusions in biotite.

Groundmass (53%) – Consists of mostly colorless glass (however slightly darker than seen in other Tocopuri samples) with some vesicles and crystal fragments.

Appendix B: Fe-Ti Oxide Data

Chanka Sample 09001CT Thin Section

Point	Na2O	SiO2	MgO	Al2O3	Cr2O3	TiO2	CaO	FeO	MnO	V2O3	NiO	Total
1	-0.0045	0.0149	1.2925	1.6708	0.1400	5.5542	-0.0042	83.7738	0.4809	0.4886	-0.0170	93.4158
2	-0.0055	0.0436	1.3136	1.6555	0.1298	5.4916	0.0091	83.4852	0.4631	0.5008	-0.0047	93.0924
3	0.0085	0.0281	1.2626	1.5319	0.0826	5.1495	0.0427	83.0687	0.5266	0.4661	0.0330	92.2002
4	-0.0080	0.0707	1.2158	1.7369	0.0915	5.2240	0.0937	82.8855	0.4561	0.4910	0.0339	92.2990
5	0.0100	0.0367	1.2738	1.6515	0.1454	5.7801	0.0217	82.9624	0.4956	0.4429	0.0321	92.8522
6	0.0346	0.0488	1.1313	1.5593	0.1176	5.1410	0.0057	82.7138	0.5817	0.4854	-0.0500	91.8192
7	-0.0020	0.0373	1.0712	1.5007	0.1530	5.1401	0.0032	82.6188	0.5798	0.4731	0.0113	91.5886
8	-0.0220	0.0930	1.3551	1.8815	0.1549	6.0440	0.0011	82.1074	0.4798	0.4853	0.0340	92.6361
9	-0.0009	0.0653	1.8125	0.2642	0.0444	37.3843	0.0115	57.3300	0.5903	0.2518	0.0219	97.7762
10	-0.0050	0.0302	1.7906	0.2321	0.0512	37.8755	-0.0030	56.5054	0.6061	0.3520	0.0190	97.4620
11	0.0119	0.0411	2.0894	0.2800	0.0091	38.1772	0.0304	55.5242	0.5498	0.3131	-0.0086	97.0262
12	-0.0229	0.1405	1.0731	1.9541	0.0344	6.6856	0.0438	81.1453	0.5816	0.4004	0.0189	92.0776
13	-0.0090	0.0551	1.3629	1.8194	0.2421	5.9520	0.0021	81.7699	0.5189	0.4851	-0.0094	92.2074
14	0.0135	0.0195	1.3251	1.7212	0.3517	5.4842	0.0076	82.6827	0.4694	0.4234	0.0490	92.5474
15	0.0140	0.0333	1.3648	1.6869	0.2389	5.8446	-0.0088	81.4690	0.5004	0.4971	0.0236	91.6725
16	-0.0170	0.0390	1.3497	1.7970	0.1855	5.8848	0.0055	82.8757	0.5177	0.4823	0.0387	93.1759
17	0.0130	1.4492	2.3461	0.3651	0.0514	41.8588	0.0476	49.6766	0.6475	0.3224	0.0535	96.8311
18	0.2007	4.0451	1.1916	2.6822	0.1706	8.3204	0.0550	75.1665	0.5317	0.7642	0.0484	93.1765
19	0.0032	0.0236	1.6888	0.2171	0.0252	36.9164	0.0023	57.3220	0.5675	0.3014	0.0713	97.1387

Chanka Sample 09001CT Sample Mount

Point	Na2O	SiO2	MgO	Al2O3	Cr2O3	TiO2	CaO	FeO	MnO	V2O3	NiO	Total
1	0.0601	1.0746	1.6787	0.3239	0.0335	37.1279	-0.0064	56.7017	0.6614	0.2374	-0.0430	97.8990
2	-0.0171	0.0150	1.0814	1.5895	0.1500	4.9878	0.0099	83.9727	0.5928	0.4232	0.0312	92.8535
3	-0.0161	0.0392	1.4146	1.5364	0.0726	5.1509	0.0006	82.2460	0.4889	0.4850	0.0511	91.4851
4	0.0060	0.0224	1.2878	1.7863	0.1685	7.0991	0.0008	80.7865	0.6114	0.6209	0.0227	92.4124
5	0.0071	0.0531	0.9812	1.7005	0.1479	4.7246	0.0006	83.1010	0.4263	0.1579	0.0719	91.3719
6	-0.0010	0.0859	1.1840	2.0308	0.2040	5.1630	0.0128	80.8132	0.5151	0.4761	0.0539	90.5387
7	-0.0086	0.0093	2.1873	0.2138	0.0347	40.6224	0.0030	53.2556	0.6800	0.3660	0.0449	97.4171

Chanka Sample Mount (Continued)

Point	Na2O	SiO2	MgO	Al2O3	Cr2O3	TiO2	CaO	FeO	MnO	V2O3	NiO	Total
8	0.0025	0.0886	1.2682	1.9595	0.1604	6.4331	0.0090	81.5361	0.5740	0.5685	0.0170	92.6170
9	0.0292	0.0692	1.1184	1.6529	0.1976	4.9844	-0.0138	82.8091	0.5360	0.4554	0.0690	91.9212
10	-0.0037	0.0248	1.6127	0.2435	0.0364	36.9086	0.0057	56.7523	0.6880	0.3893	-0.0468	96.6613

Chao Sample 09003CT Thin Section

Point	Na2O	SiO2	MgO	Al2O3	Cr2O3	TiO2	CaO	FeO	MnO	V2O3	NiO	Total
1	0.0130	0.0238	1.4110	0.1857	0.0413	35.3728	0.0455	58.9540	0.5786	0.3908	0.0496	97.0661
2	-0.0268	0.0877	0.9952	1.4563	0.1825	4.5082	0.0109	84.7567	0.5503	0.4520	0.0237	93.0234
3	0.0056	-0.0006	1.3609	0.2007	0.0525	35.6929	0.0108	58.9561	0.5805	0.3804	-0.0229	97.2402
4	0.0040	0.0692	0.9559	1.5477	0.2165	4.5315	0.0203	84.0209	0.4715	0.4498	0.0123	92.2995
5	0.0075	0.0138	1.3061	0.1937	0.0369	34.4574	0.0464	58.6401	0.4890	0.3301	0.0391	95.5601
6	0.0028	0.0028	1.2665	0.2030	0.0602	35.1249	0.0594	58.4655	0.4503	0.3750	-0.0038	96.0104
7	-0.0074	0.0177	1.4711	0.2003	0.0615	35.5287	0.0176	58.5934	0.5741	0.3752	-0.0162	96.8395
8	0.0187	0.0444	0.8645	1.4684	0.2060	4.7641	0.0000	83.0076	0.4932	0.5645	0.0369	91.4682
9	-0.0005	0.0455	0.9020	1.5161	0.1954	4.8231	0.0199	83.4722	0.5063	0.5816	0.0341	92.0961
10	0.0009	0.0155	1.4028	0.1892	0.0420	34.7777	0.0551	59.3518	0.5808	0.4585	0.0706	96.9450
11	0.0149	0.0762	1.1943	0.2248	0.0634	34.2435	0.0617	58.2566	0.5711	0.3537	0.0477	95.1080
12	0.0176	0.0789	0.9948	1.4481	0.2142	5.6365	0.0478	81.7872	0.5259	0.5226	0.0246	91.2982
13	0.0028	0.0276	1.3981	0.1921	0.0656	35.2394	0.0666	58.5004	0.5583	0.3856	-0.0210	96.4364
14	-0.0126	0.0721	0.9210	1.5306	0.2038	4.8223	0.0151	83.3656	0.5704	0.5160	0.0795	92.0962
15	0.0070	0.0315	1.5062	0.2004	0.0501	35.6111	0.0066	58.2061	0.5247	0.3623	-0.0067	96.5059
16	0.0010	0.0317	0.8484	1.5087	0.2086	4.4831	0.0233	84.1669	0.4474	0.5298	-0.0095	92.2490
17	0.0252	0.0495	0.8847	1.5265	0.1891	5.5463	0.0044	83.3380	0.5350	0.5120	0.0009	92.6118
18	-0.0255	0.0574	1.5227	0.2082	0.0546	35.5130	0.0200	58.7653	0.5746	0.3909	0.0410	97.1478
19	0.0101	0.0283	0.9526	1.5045	0.1868	4.6610	0.0333	84.1381	0.4573	0.5838	0.0407	92.5963
20	-0.0121	0.0226	1.4101	0.2169	0.0612	34.8618	0.0234	58.3517	0.5729	0.3854	0.0181	95.9242
21	0.0010	2.0402	0.4910	0.2206	0.0149	11.4715	0.1072	77.8734	0.4148	0.1790	0.0541	92.8677
22	-0.0163	0.0226	1.3640	0.1791	0.0607	35.2567	0.0349	59.1979	0.5167	0.3408	0.0076	96.9810
23	0.0152	0.0605	0.9424	1.4802	0.2241	4.7972	0.0036	84.0836	0.5337	0.5693	-0.0066	92.7097
24	-0.0051	0.0986	0.8699	1.5536	0.2007	4.8015	0.0019	84.0136	0.4710	0.6377	-0.0255	92.6485

Chao Sample 09003CT Sample Mount

Point	Na2O	SiO2	MgO	Al2O3	Cr2O3	TiO2	CaO	FeO	MnO	V2O3	NiO	Total
1	-0.0061	0.0161	0.8742	1.5256	0.2166	4.7863	0.0008	84.3838	0.5181	0.7003	-0.0198	93.0219
2	0.0195	-0.0022	1.3948	0.1960	0.0228	35.0860	-0.0057	59.2599	0.4639	0.2985	0.0124	96.7539
3	-0.0149	0.1490	1.2355	0.2159	0.0590	33.7774	0.0104	56.9163	0.5044	0.2986	0.0057	93.1722
4	-0.0107	0.1295	0.9518	0.2662	0.0455	35.1633	0.0075	58.0906	0.5991	0.2986	0.0305	95.5827
5	-0.0082	0.0416	2.1546	0.1779	0.0215	39.8666	0.0521	49.9253	0.7809	0.3748	0.0363	93.4317
6	0.0070	0.0188	1.4508	0.1775	0.0474	35.2622	0.0098	59.0858	0.5081	0.2567	0.0572	96.8812
7	0.0112	0.0345	0.8750	0.8219	0.2109	4.5929	0.0334	83.8209	0.3894	0.6065	0.0435	91.4400
8	0.0121	-0.0075	0.9524	1.7656	0.1487	4.4923	0.0061	84.7448	0.4934	0.5661	0.0350	93.2165
9	-0.0009	0.0723	2.0388	0.2474	0.0423	34.4587	0.0200	54.2566	0.6898	0.3288	0.0095	92.1643
10	-0.0025	0.0162	1.2737	1.3252	0.2085	1.3741	0.0212	86.0697	0.9547	0.5092	-0.0151	91.7525
11	-0.0014	0.0221	1.2126	0.1978	0.0623	34.4371	-0.0036	59.4361	0.5294	0.2588	0.0896	96.2458
12	-0.0292	-0.0320	1.4742	0.1937	0.0498	35.4461	0.0121	58.9239	0.5432	0.4193	0.0277	97.0899
13	0.0005	0.0552	1.2941	0.2396	0.0502	35.1230	0.0089	58.2877	0.5372	0.3171	0.0238	95.9372
14	0.0168	0.0215	0.9124	0.1355	0.0462	35.4612	0.0136	59.5208	0.5683	0.3035	0.0000	96.9997
15	0.0194	0.0488	1.0800	1.4853	0.0000	0.0000	0.0002	82.6969	0.5230	0.5018	0.0500	86.4053
16	-0.0072	0.0782	0.9286	0.9116	0.1816	0.0024	-0.0052	81.7767	0.4923	0.5011	-0.0245	84.8726
17	0.0056	0.0507	0.9673	1.5178	0.2190	4.6472	0.0021	84.8524	0.5234	0.5102	0.0085	93.3042
18	0.0197	0.0426	0.9677	1.6047	0.2479	4.8813	-0.0019	84.1656	0.4933	0.4913	0.0208	92.9349
19	0.0025	0.0375	0.6494	1.3964	0.2289	4.1242	0.0116	82.9263	0.4413	0.5989	0.0614	90.4784
20	0.0023	0.1181	1.5181	0.2159	0.1025	33.7736	0.0043	56.1156	0.4915	0.3488	0.0467	92.7376
21	-0.0020	0.0310	0.3585	1.6431	0.2233	6.0429	0.0069	78.1003	0.1995	0.6451	0.0076	87.2583
22	0.0000	0.0734	1.4974	0.1950	0.0549	34.9063	0.0149	58.4057	0.5367	0.2646	0.0439	95.9928
23	-0.0066	0.0525	0.3758	1.5157	0.0881	3.2104	0.0147	78.0577	0.1526	0.5587	-0.0293	84.0261
24	-0.0041	0.0058	1.1645	1.2698	0.1838	0.4945	0.0227	87.7741	0.7926	0.6032	-0.0066	92.3110
25	-0.0176	0.0270	1.3903	0.2050	0.0559	34.9964	0.0113	57.5881	0.4942	0.3041	-0.0048	95.0724

Chillahuita Sample 09009CT Thin Section

Point	Na2O	SiO2	MgO	Al2O3	Cr2O3	TiO2	CaO	FeO	MnO	V2O3	NiO	Total
1	0.0181	0.0745	1.2591	1.9431	0.3317	4.2316	-0.0050	80.7236	0.6668	0.5141	0.0133	89.7759
2	0.0066	0.0282	0.5641	0.0863	0.0690	71.9667	-0.0020	23.8985	0.2002	0.7226	0.0000	97.5422
3	0.0237	0.0417	1.4497	2.0535	0.2285	2.5325	0.0090	84.5467	0.7918	0.5182	-0.0208	92.1952
4	-0.0060	0.0479	1.8538	0.1968	0.0010	38.1743	0.0549	56.0677	0.6476	0.0976	-0.0096	97.1417
5	-0.0409	0.0323	0.9377	1.5043	0.1793	4.6528	-0.0054	84.1447	0.5229	0.4959	-0.0199	92.4699

Chillahuita Sample 09009CT Thin Section (Continued)

Point	Na2O	SiO2	MgO	Al2O3	Cr2O3	TiO2	CaO	FeO	MnO	V2O3	NiO	Total
6	-0.0088	0.0182	1.5480	0.2108	0.0518	35.7818	0.0042	58.7308	0.5926	0.4330	0.0076	97.3788
7	-0.0035	0.0496	0.9658	1.4944	0.2039	4.8555	0.0120	84.0570	0.5454	0.5207	-0.0407	92.7043
8	0.0050	0.0175	1.1549	0.2305	0.0593	40.1344	0.0021	54.0488	0.4275	0.4580	0.0124	96.5505
9	0.0120	0.0856	0.2240	0.8601	0.2206	10.1376	0.0480	78.1178	0.0378	0.6052	0.0161	90.3650
10	-0.0215	0.0000	1.2731	0.2685	0.0263	25.1564	0.0027	65.5725	0.2992	0.2029	-0.0266	92.8015
11	-0.0111	0.0309	1.5324	0.1913	0.0466	35.6833	0.0172	57.9021	0.4728	0.3624	0.0143	96.2533
12	0.0014	0.0386	1.3001	0.3232	0.0553	25.7114	0.0027	65.1479	0.3525	0.3087	0.0257	93.2676
13	0.0000	0.3778	0.5943	1.1815	0.2157	5.4223	0.0315	79.7273	0.2464	0.4561	0.0643	88.3172
14	0.0203	0.2545	0.5402	1.4083	0.2196	3.2853	0.0038	82.6378	0.2238	0.5349	0.0539	89.1825
15	0.0181	0.0011	1.5168	0.1911	0.0557	35.8164	0.0321	57.9216	0.5423	0.3125	0.0181	96.4258
16	0.0066	-0.0029	0.9332	1.4745	0.2154	4.8886	0.0055	83.3652	0.5513	0.6134	0.0624	92.1161
17	0.0009	-0.0177	1.4235	0.1852	0.0463	36.0522	0.0070	58.2571	0.5748	0.3413	0.0029	96.8913
18	0.0298	0.0559	0.9347	1.4542	0.2120	4.4264	0.0288	83.8840	0.4800	0.5906	-0.0189	92.0965
19	0.0000	0.0365	1.5884	0.1786	0.0470	35.3053	0.0247	58.3670	0.6209	0.3726	0.0716	96.6125
20	0.0055	0.0477	0.8145	1.4641	0.2024	6.7657	0.0036	83.5969	0.4643	0.5039	0.0123	93.8810
21	0.0015	0.0238	0.8102	0.6654	0.0477	14.4280	0.0110	73.2989	0.1110	0.2976	-0.0028	89.6953
22	0.0146	0.0386	0.7989	1.4186	0.2125	5.4901	0.0153	80.6160	0.3460	0.5733	0.0463	89.5700
23	0.0028	0.0324	1.2756	0.1644	0.0487	37.9094	0.0021	54.8787	0.4301	0.4275	-0.0143	95.1717
24	-0.0107	0.0232	1.5775	0.1894	0.0490	35.3082	0.0175	57.9562	0.5295	0.2939	-0.0029	95.9446
25	0.0056	0.0450	0.9411	1.4634	0.1926	3.7674	0.0023	84.4240	0.5205	0.5211	0.0161	91.8991

Chillahuita Sample 09009CT Sample Mount

Point	Na2O	SiO2	MgO	Al2O3	Cr2O3	TiO2	CaO	FeO	MnO	V2O3	NiO	Total
1	0.0111	0.0340	0.8811	1.4706	0.1671	4.5936	0.0006	83.6546	0.4763	0.5562	0.1276	91.9728
2	-0.0076	0.0513	0.8808	1.4540	0.2353	4.7400	-0.0105	84.2354	0.4425	0.5128	0.0350	92.5871
3	0.0111	0.0167	0.8693	1.4736	0.1978	4.7491	-0.0013	84.0032	0.4913	0.5686	0.0350	92.4157
4	0.0153	0.0022	1.4221	0.1769	0.0583	35.8503	0.0613	58.5614	0.5793	0.3436	-0.0067	97.0707
5	-0.0086	0.1511	1.0417	1.5162	0.1410	4.4027	0.0046	83.6510	0.5030	0.4736	-0.0019	91.8849
6	0.0096	-0.0038	1.1380	0.2171	0.0591	39.5807	0.0062	50.5690	0.5530	0.3155	-0.0096	92.4482
7	0.0126	0.0342	1.1110	0.1866	0.0460	45.2049	0.0182	46.9000	0.3746	0.4230	-0.0517	94.3110
8	0.0061	0.0530	0.9622	1.4856	0.1888	4.8141	0.0223	83.9583	0.5446	0.4910	-0.0019	92.5260
9	0.0097	0.0050	1.4776	0.1924	0.0250	35.0619	0.0151	57.6423	0.5577	0.4117	0.0153	95.4136
10	0.0000	0.0279	1.0813	0.1736	0.0348	39.7481	-0.0021	53.7146	0.3689	0.4787	0.0344	95.6623

Chillahuita Sample 09009CT Sample Mount (Continued)

Point	Na2O	SiO2	MgO	Al2O3	Cr2O3	TiO2	CaO	FeO	MnO	V2O3	NiO	Total
11	0.0186	-0.0055	1.4944	0.1917	0.0407	35.5276	0.0294	58.7249	0.5630	0.2962	-0.0057	96.8865
12	0.0045	0.0429	0.4099	0.9254	0.2265	8.3193	0.0128	78.7879	0.2085	0.5720	0.0009	89.5107
13	-0.0182	0.0519	0.9999	1.5096	0.1843	4.4771	0.0204	83.5649	0.5783	0.5198	0.0057	91.9119
14	0.0111	-0.0182	1.4485	0.1898	0.0474	36.0882	0.0307	58.1789	0.5929	0.3438	0.0114	96.9427
15	0.0046	0.0480	1.4403	0.1841	0.0570	35.1773	0.0283	58.6586	0.5662	0.2699	0.0238	96.4581
16	-0.0015	0.0351	0.8832	1.4739	0.2001	4.6730	-0.0040	83.9092	0.5268	0.4907	0.0586	92.2506
17	0.0182	0.0830	0.9860	1.4596	0.1885	4.6902	0.0113	83.9047	0.5184	0.5177	0.0066	92.3841
18	0.0106	0.0392	0.9047	1.4787	0.1824	4.7533	0.0015	83.2576	0.4723	0.5859	0.0274	91.7136
19	0.0204	0.0348	1.4662	0.1980	0.0517	35.6874	0.0070	58.6358	0.5756	0.3802	-0.0086	97.0569
20	-0.0045	0.0294	1.0026	1.4997	0.1790	4.8197	-0.0053	83.9489	0.4675	0.4716	0.0425	92.4610
21	-0.0139	0.0408	1.4742	0.2022	0.0424	35.3386	0.0160	58.4178	0.5469	0.3355	0.0343	96.4487
22	0.0075	0.5808	1.3213	1.4962	0.2271	4.7168	0.0117	83.8996	0.4849	0.5729	0.0284	93.3472
23	0.0063	-0.0135	0.9228	0.1674	0.0583	47.3856	0.0007	46.3404	0.3687	0.3568	-0.0096	95.6069

Tocopuri Sample 09011CT Thin Section

Point	Na2O	SiO2	MgO	Al2O3	Cr2O3	TiO2	CaO	FeO	MnO	V2O3	NiO	Total
1	-0.0018	0.0649	1.3111	0.2181	0.0354	36.6372	0.1597	55.1796	1.0358	0.3028	-0.0458	94.9447
2	0.0030	0.0599	0.7464	1.1444	0.1593	4.2392	0.0275	84.3971	0.7850	0.4822	-0.0321	92.0442
3	-0.0005	-0.0111	1.0383	0.2268	0.0383	28.3654	0.0935	63.6531	0.4124	0.3465	-0.0124	94.1744
4	0.0066	0.0219	0.6424	1.1138	0.1951	4.5489	0.0191	83.5113	0.7041	0.5555	0.0170	91.3356
5	0.0046	0.0888	0.7616	1.1754	0.2574	4.2456	0.0187	85.2914	0.6341	0.4994	0.0690	93.0460
6	0.0253	0.0663	0.7689	1.1619	0.1733	4.3755	0.0090	84.3743	0.7050	0.4509	0.0180	92.1284
7	0.0010	0.0196	0.6804	1.1747	0.1735	4.5640	0.0076	83.6472	0.6398	0.5483	0.0378	91.4939
8	0.0238	0.0582	0.7447	1.1470	0.1542	4.3015	0.0004	84.8832	0.7155	0.5866	-0.0132	92.6150
9	0.0020	0.0398	0.7546	1.1673	0.1487	4.3082	0.0069	85.3026	0.7305	0.5330	0.0180	93.0115
10	-0.0193	0.0207	0.7175	1.1473	0.1384	4.3520	0.0029	85.2816	0.6122	0.5331	0.0151	92.8209
11	-0.0249	0.0305	0.7465	1.1474	0.1435	4.2726	0.0233	84.8718	0.6327	0.5550	0.0539	92.4772
12	-0.0123	0.0445	0.6500	0.4140	0.1952	1.4595	0.0091	87.7420	0.6565	0.5697	0.0104	91.7508
13	0.0111	0.0328	0.7991	1.1069	0.1891	5.3907	0.0261	83.6032	0.6514	0.4768	-0.0388	92.2873
14	0.0101	0.0386	0.7648	1.1680	0.1642	4.1623	0.0137	84.5581	0.6847	0.4723	0.0132	92.0502
15	-0.0025	0.0616	0.7485	1.1744	0.1724	4.3219	0.0221	85.6227	0.6617	0.4676	0.0094	93.2623
16	-0.0304	0.0139	1.0155	0.2285	0.0246	28.6687	0.0335	64.1943	0.3587	0.3231	0.0581	94.9188
17	0.0541	0.1582	0.9672	0.3174	0.0205	28.1743	0.1874	64.2275	0.3660	0.3051	0.0124	94.7900

Tocopuri Sample 09011CT Thin Section (Continued)

Point	Na2O	SiO2	MgO	Al2O3	Cr2O3	TiO2	CaO	FeO	MnO	V2O3	NiO	Total
18	0.0148	0.0616	1.3723	0.1388	0.0255	36.4736	0.2050	55.8235	1.0850	0.2815	0.0439	95.5255
19	0.0086	0.0789	0.8173	1.1721	0.1898	4.3766	0.0157	83.6817	0.6392	0.5483	0.0671	91.5953
20	-0.0015	0.0720	0.7717	1.1855	0.1738	4.2816	0.0468	84.6921	0.7578	0.5795	0.0028	92.5637

Tocopuri Sample 09011CT Sample Mount

Point	Na2O	SiO2	MgO	Al2O3	Cr2O3	TiO2	CaO	FeO	MnO	V2O3	NiO	Total
1	0.0041	1.2888	0.0572	0.3695	-0.0017	0.0842	0.0220	85.9070	0.1033	0.0286	0.3632	88.2278
2	0.0223	0.1054	0.7527	1.2454	0.1937	3.9923	0.0445	83.7416	0.6419	0.4990	0.0510	91.2897
3	0.0000	-0.0029	1.1757	3.4880	0.2144	7.1561	0.0324	78.5760	0.7654	0.5921	-0.0104	91.9999
4	-0.0066	0.1463	0.6545	0.1845	0.0295	29.4572	0.0408	58.4066	0.5738	0.2363	0.0428	89.7722
5	0.0082	0.0179	0.6923	0.4780	0.1755	2.0131	-0.0088	87.2752	0.7301	0.5561	0.0000	91.9464
6	0.0157	0.0340	0.7794	1.1738	0.1821	4.3104	0.0017	85.2461	0.7520	0.5378	-0.0416	93.0330
7	0.0111	1.1505	0.5308	1.6350	0.1801	4.5975	0.0210	80.1977	0.6225	0.4705	0.0009	89.4176
8	-0.0101	0.0213	0.7723	1.1475	0.1588	4.2346	0.0376	85.5387	0.6573	0.4309	0.0907	93.0896
9	0.0219	0.0702	0.1202	1.0424	0.1579	3.7647	0.0212	82.0302	0.1360	0.5025	0.0208	87.8880
10	0.0218	0.0564	0.8567	1.1453	0.1680	4.2994	0.0181	84.4621	0.7310	0.5841	-0.0227	92.3429

Chascon Sample Mount

Point	Na2O	SiO2	MgO	Al2O3	Cr2O3	TiO2	CaO	FeO	MnO	V2O3	NiO	Total
1	0.0000	0.0357	0.5399	1.0981	0.1085	4.8651	0.0044	84.0845	0.5871	0.4339	0.0463	91.8035
2	0.0000	0.0369	0.5377	1.1803	0.0959	3.6308	0.0088	85.9328	0.4918	0.5167	0.0340	92.4656
3	0.0173	0.0040	0.6564	1.1944	0.1115	3.7529	0.0149	85.7944	0.6274	0.5268	0.0179	92.7178
4	0.0157	0.1712	0.7307	1.2144	0.3451	3.9557	0.0174	80.4946	0.6180	0.5000	0.4270	88.4898
5	-0.0020	0.0213	0.6384	1.1776	0.1423	3.9794	0.0175	85.0292	0.6209	0.5128	-0.0227	92.1394
6	0.0020	0.0548	0.6365	1.1866	0.0800	3.6783	0.0074	85.1857	0.7253	0.4758	0.0529	92.0853
7	0.0131	0.0229	0.5056	1.0322	0.1277	6.7828	0.0004	75.5783	0.4871	0.5137	0.1030	85.1669
8	0.0237	0.0517	0.3961	1.2073	0.1051	6.1885	-0.0063	83.1629	0.6042	0.4041	0.0283	92.1719
9	0.0096	0.0334	0.5719	1.2488	0.1013	3.9571	-0.0038	85.0982	0.6462	0.6435	0.0652	92.3753
10	0.0260	0.1295	0.9654	0.1463	0.0368	34.6219	0.0134	55.9952	0.7373	0.2385	0.0658	92.9759
11	0.0107	0.2690	0.8212	0.1413	0.0404	34.5316	0.0190	55.0584	0.8140	0.3462	0.0038	92.0557
12	0.0325	0.0390	0.6225	0.2376	0.0382	35.6947	0.0184	55.9149	0.4643	0.4384	0.0029	93.5033

Appendix C: Ar/Ar Data

Chao

Incremental Heating			36Ar(a)	37Ar(ca)	38Ar(cl)	39Ar(k)	40Ar(r)	Age ± 2s (Ka)	40Ar(r) (%)	39Ar (k) (%)	K/Ca ± 2s
BG4697	35.0 %	4	0.003500	0.009032	0.000681	0.612777	0.053554	118.3 ± 18.9	4.92	12.60	29.173 ± 1.039
BG4698	35.0 %	4	0.001880	0.003210	0.000463	0.394284	0.036260	124.5 ± 26.1	6.13	8.11	52.810 ± 3.853
BG4700	35.0 %	4	0.005872	0.006368	0.000712	0.609561	0.043711	97.1 ± 26.7	2.46	12.54	41.159 ± 1.704
BG4701	35.0 %	4	0.005066	0.012280	0.000796	0.744252	0.060567	110.2 ± 16.1	3.89	15.31	26.061 ± 0.979
BG4703	35.0 %	4	0.003166	0.001983	0.000343	0.287670	0.025276	118.9 ± 39.4	2.63	5.92	62.385 ± 4.425
BG4704	35.0 %	4	0.004759	0.011309	0.000674	0.512381	0.034921	92.3 ± 21.1	2.42	10.54	19.482 ± 0.724
BG4706	35.0 %		0.002528	0.002420	0.000258	0.287260	0.036603	172.5 ± 33.9	4.67	5.91	51.034 ± 3.822
BG4707	35.0 %	4	0.003228	0.009422	0.000916	0.509483	0.041864	111.2 ± 21.4	4.20	10.48	23.251 ± 1.017
BG4709	35.0 %	4	0.003327	0.006517	0.000983	0.597059	0.052190	118.3 ± 22.0	5.04	12.28	39.393 ± 1.647
BG4710	35.0 %	4	0.003563	0.003091	0.000470	0.308072	0.026857	118.0 ± 31.4	2.49	6.34	42.850 ± 2.411
		Σ	0.036889	0.065635	0.006297	4.862799	0.411803				

Information on Analysis		Results	40(r)/39(k) ± 2s		Age ± 2s (Ka)		MSWD	39Ar (k) (%,n)	K/Ca ± 2s
88073		Weighted Plateau	0.0821	± 0.0056	111.2	± 7.5	0.84	94.09	26.789 ± 5.879
Biotite				± 6.77%		± 6.77%		9	
H1					External Error	± 8.7	2.31	Statistical T Ratio	
LAS					Analytical Error	± 7.5	1.0000	Error Magnification	
Project = UW85E		**Total Fusion Age**	0.0847	± 0.0056	114.6	± 7.6		10	0.894 ± 0.013
Irradiation = UW85				± 6.65%		± 6.65%			
J = 0.0007395 ± 0.0000004					External Error	± 8.8			
FCs = 28.201 ± 0.003 Ma					Analytical Error	± 7.6			

Chillahuita

Incremental Heating			36Ar(a)	37Ar(ca)	38Ar(cl)	39Ar(k)	40Ar(r)	Age ± 2s (Ka)	40Ar(r) (%)	39Ar (k) (%)	K/Ca ± 2s
BG4712	35.0 %	4	0.001652	0.005206	0.000389	0.287032	0.022444	103.4 ± 47.6	4.40	5.08	23.710 ± 1.009
BG4713	35.0 %	4	0.001416	0.007688	0.000563	0.502315	0.045371	119.5 ± 25.0	9.78	8.88	28.096 ± 1.178
BG4715	35.0 %	4	0.003224	0.032052	0.001340	1.076933	0.088256	108.4 ± 11.8	8.48	19.05	14.448 ± 0.472
BG4716	35.0 %	4	0.002793	0.020332	0.001026	0.762786	0.067605	117.2 ± 19.4	7.57	13.49	16.132 ± 0.571
BG4718	35.0 %	4	0.002444	0.018732	0.000835	0.692579	0.061530	117.5 ± 16.3	7.85	12.25	15.898 ± 0.563
BG4719	35.0 %	4	0.001259	0.021296	0.000743	0.617455	0.053009	113.6 ± 16.2	12.47	10.92	12.467 ± 0.425
BG4721	35.0 %	4	0.001787	0.013997	0.000555	0.516728	0.039998	102.4 ± 24.1	7.04	9.14	15.875 ± 0.649
BG4722	35.0 %	4	0.001090	0.013661	0.000599	0.370580	0.025181	89.9 ± 25.2	7.25	6.55	11.665 ± 0.410
BG4724	35.0 %	4	0.001516	0.015227	0.000652	0.460059	0.034398	98.9 ± 20.7	7.13	8.14	12.991 ± 0.449
BG4725	35.0 %	4	0.001110	0.010351	0.000329	0.367119	0.025001	90.1 ± 19.3	7.08	6.49	15.250 ± 0.529
		Σ	0.018290	0.158542	0.007030	5.653585	0.462794				

Information on Analysis		Results	40(r)/39(k) ± 2s	Age ± 2s (Ka)	MSWD	39Ar (k) (%,n)	K/Ca ± 2s
84054		Weighted Plateau	0.0815 ± 0.0048 ± 5.91%	107.8 ± 6.4 ± 5.91%	1.13	100.00 10	14.452 ± 2.019
Biotite				External Error ± 7.6	2.26	Statistical T Ratio	
I11				Analytical Error ± 6.4	1.0611	Error Magnification	
LAS							
Project = UW85F		Total Fusion Age	0.0819 ± 0.0049 ± 5.97%	108.3 ± 6.5 ± 5.97%		10	0.430 ± 0.005
Irradiation = UW85							
J = 0.0007227 ±				External Error ± 7.7			
FCs = 28.201 ± 0.003 Ma				Analytical Error ± 6.5			

Tocopuri

Incremental Heating			36Ar(a)	37Ar(ca)	38Ar(cl)	39Ar(k)	40Ar(r)	Age ± 2σ (Ka)	40Ar(r) (%)	39Ar (k) (%)	K/Ca ± 2σ
BG4682	35.0 %	4	0.001261	0.030990	0.001061	0.890666	0.073988	114.6 ± 7.8	16.57	12.39	12.358 ± 0.410
BG4683	35.0 %	4	0.002111	0.031351	0.001235	1.213918	0.096710	109.9 ± 6.1	13.42	16.89	16.650 ± 0.560
BG4685	35.0 %	4	0.002281	0.036119	0.001053	0.938789	0.077947	114.5 ± 11.0	10.37	13.06	11.176 ± 0.367
BG4686	35.0 %	4	0.000978	0.012496	0.000676	0.646173	0.053639	114.5 ± 9.9	15.66	8.99	22.236 ± 0.978
BG4688	35.0 %	4	0.001408	0.031871	0.001149	0.779549	0.057212	101.2 ± 14.4	12.09	10.84	10.518 ± 0.351
BG4689	35.0 %	4	0.002363	0.013796	0.001008	0.707034	0.057775	112.7 ± 15.7	7.64	9.84	22.037 ± 0.923
BG4691	35.0 %	4	0.002138	0.024896	0.000945	0.856909	0.064144	103.2 ± 7.4	9.22	11.92	14.800 ± 0.474
BG4692	35.0 %	4	0.000422	0.010245	0.000321	0.261564	0.023980	126.4 ± 25.3	16.12	3.64	10.978 ± 0.539
BG4694	35.0 %	4	0.001357	0.174858	0.001177	0.627441	0.048582	106.8 ± 27.0	10.81	8.73	1.543 ± 0.049
BG4695	35.0 %	4	0.000356	0.170223	0.000582	0.266077	0.021948	113.8 ± 21.1	17.25	3.70	0.672 ± 0.023
		Σ	0.014675	0.536846	0.009207	7.188119	0.575925				

Information on Analysis		Results	40(r)/39(k) ± 2σ	Age ± 2σ (Ka)	MSWD	39Ar (k) (%,n)	K/Ca ± 2σ
84064		Weighted Plateau	0.0800 ± 0.0025 ± 3.07%	110.3 ± 3.4 ± 3.07%	1.08	100.00 10	0.999 ± 1.010
Biotite				External Error ± 5.5	2.26	Statistical T Ratio	
G11				Analytical Error ± 3.4	1.0374	Error Magnification	
LAS							
Project = UW85D		Total Fusion Age	0.0801 ± 0.0030 ± 3.78%	110.5 ± 4.2 ± 3.78%		10	0.161 ± 0.002
Irradiation = UW85							
J = 0.0007535 ± 0.0000005				External Error ± 6.0			
FCs = 28.201 ± 0.003 Ma				Analytical Error ± 4.2			

Chanka

Incremental Heating			36Ar(a)	37Ar(ca)	38Ar(cl)	39Ar(k)	40Ar(r)	Age ± 2s (Ka)	40Ar(r) (%)	39Ar (%)	K/Ca ± 2s
BG4727	35.0 %	4	0.001962	0.019087	0.000760	0.452849	0.041181	123.1 ± 22.2	6.63	8.80	10.202 ± 0.380
BG4728	35.0 %	4	0.000877	0.010298	0.000403	0.313698	0.026809	115.7 ± 32.3	9.38	6.10	13.099 ± 0.507
BG4730	35.0 %	4	0.001307	0.015741	0.000232	0.272042	0.024876	123.8 ± 40.3	6.05	5.29	7.432 ± 0.254
BG4731	35.0 %	4	0.001291	0.004804	0.000276	0.187908	0.013171	94.9 ± 42.4	3.34	3.65	16.821 ± 0.789
BG4733	35.0 %	4	0.004544	0.045344	0.001503	0.967859	0.087860	122.9 ± 11.3	6.14	18.81	9.178 ± 0.296
BG4734	35.0 %	4	0.003372	0.041262	0.001156	0.820222	0.073326	121.0 ± 9.5	6.85	15.94	8.548 ± 0.295
BG4736	35.0 %	4	0.001043	0.009680	0.000400	0.327921	0.029754	122.8 ± 29.8	8.81	6.37	14.566 ± 0.576
BG4737	35.0 %	4	0.001026	0.011979	0.000375	0.313696	0.028405	122.6 ± 24.6	8.57	6.10	11.261 ± 0.401
BG4739	35.0 %	4	0.003751	0.040083	0.001505	1.074398	0.088438	111.4 ± 13.1	7.39	20.88	11.526 ± 0.385
BG4740	35.0 %	4	0.001520	0.036605	0.000535	0.415012	0.038416	125.3 ± 20.1	7.88	8.07	4.875 ± 0.160
		Σ	0.020693	0.234883	0.007145	5.145605	0.452237				

Information on Analysis	Results	40(r)/39(k) ± 2s	Age ± 2s (Ka)	MSWD	39Ar (%,n)	K/Ca ± 2s
88072	Weighted Plateau	0.0885 ± 0.0040 ± 4.52%	119.8 ± 5.4 ± 4.53%	0.44	100.00 10	8.013 ± 1.993
Biotite			External Error ± 7.2	2.26	Statistical T Ratio	
K2			Analytical Error ± 5.4	1.0000	Error Magnification	
LAS						
Project = UW85E	Total Fusion Age	0.0879 ± 0.0045 ± 5.14%	119.0 ± 6.1 ± 5.14%		10	0.264 ± 0.003
Irradiation = UW85			External Error ± 7.7			
J = 0.0007395 ± 0.0000004			Analytical Error ± 6.1			
FCs = 28.201 ± 0.003 Ma						

Appendix D: Zircon U-Th Data

* = U-Pb analysis preformed #NUM! = Unable to calculate age (on the equiline)

Chao

Set	Pt.	($^{238}U/^{232}Th$)	1s	($^{230}Th/^{232}Th$)	1s	Delta Y	1s	Delta X	1s	m	1s	Age (Ka)	1s -	1s +	U
1	1	5.9271	0.0876	5.3571	0.1608	4.6331	0.1608	5.2011	0.0876	0.8908	0.0344	241.8	41.2	-29.9	621
1	2*	5.2068	0.0681	5.2408	0.1697	4.5168	0.1697	4.4808	0.0681	1.0080	0.0409	#NUM	#NUM!	#NUM!	539
1	3	4.8149	0.1047	4.3824	0.1394	3.6584	0.1394	4.0889	0.1047	0.8947	0.0411	245.8	54.0	-36.0	531
1	4	5.8666	0.1536	3.5729	0.1520	2.8489	0.1520	5.1406	0.1536	0.5542	0.0339	88.2	8.6	-8.0	822
1	5	4.5210	0.0801	4.1275	0.1224	3.4035	0.1224	3.7950	0.0801	0.8968	0.0374	248.0	49.2	-33.8	1543
1	6*	5.4805	0.0806	5.0936	0.1362	4.3696	0.1362	4.7545	0.0806	0.9190	0.0326	274.5	56.3	-37.0	881
1	7	7.2123	0.2735	5.2798	0.1564	4.5558	0.1564	6.4863	0.2735	0.7024	0.0382	132.3	15.0	-13.2	687
1	8*	5.4920	0.0946	5.7686	0.2083	5.0446	0.2083	4.7660	0.0946	1.0584	0.0485	#NUM	#NUM!	#NUM!	889
1	9	8.8518	0.3434	5.4774	0.3621	4.7534	0.3621	8.1258	0.3434	0.5850	0.0510	96.0	14.3	-12.6	502
1	10	9.1112	0.4053	7.6336	0.3387	6.9096	0.3387	8.3852	0.4053	0.8240	0.0567	189.7	42.5	-30.5	1197
1	12*	5.7773	0.0718	5.5155	0.2500	4.7915	0.2500	5.0513	0.0718	0.9486	0.0513	324.0	643.1	-75.5	941
1	13*	3.6249	0.0532	3.5817	0.1356	2.8577	0.1356	2.8989	0.0532	0.9858	0.0502	464.5	#NUM!	-165.0	684
1	15	7.7655	0.2006	6.2154	0.1910	5.4914	0.1910	7.0395	0.2006	0.7801	0.0351	165.4	19.0	-16.2	2183
2	1	4.3971	0.0366	4.0621	0.1033	3.3381	0.1033	3.6711	0.0366	0.9093	0.0296	262.1	43.1	-30.8	805
2	2	10.7882	0.1393	6.6717	0.2528	5.9477	0.2528	10.0622	0.1393	0.5911	0.0264	97.7	7.3	-6.8	635
2	3	6.1433	0.1317	5.3351	0.2080	4.6111	0.2080	5.4173	0.1317	0.8512	0.0436	208.0	37.9	-28.1	1994
2	4*	3.4260	0.0458	3.2808	0.1180	2.5568	0.1180	2.7000	0.0458	0.9470	0.0466	320.7	229.7	-68.8	818
2	5	9.5463	0.2617	6.9525	0.2066	6.2285	0.2066	8.8203	0.2617	0.7062	0.0314	133.7	12.4	-11.1	1358
2	6	4.7919	0.0919	4.2613	0.0918	3.5373	0.0918	4.0659	0.0919	0.8700	0.0299	222.8	28.6	-22.6	1617
2	7*	5.1664	0.0682	5.0060	0.1353	4.2820	0.1353	4.4404	0.0682	0.9643	0.0339	363.9	324.9	-72.9	1708
2	8	7.9816	0.1798	4.8725	0.3089	4.1485	0.3089	7.2556	0.1798	0.5718	0.0449	92.6	12.1	-10.9	499
2	9*	4.5239	0.0517	4.4805	0.1797	3.7565	0.1797	3.7979	0.0517	0.9891	0.0492	493.4	#NUM!	-186.4	997
2	10*	4.7083	0.0516	4.5046	0.0899	3.7806	0.0899	3.9823	0.0516	0.9494	0.0257	325.7	77.3	-44.8	1092
2	11	5.2356	0.2119	4.3224	0.1168	3.5984	0.1168	4.5096	0.2119	0.7979	0.0456	174.6	27.9	-22.2	3527
2	12	4.6708	0.0505	4.1726	0.0758	3.4486	0.0758	3.9448	0.0505	0.8742	0.0222	226.4	21.2	-17.8	2180
2	13	5.0483	0.0842	4.1378	0.0942	3.4138	0.0942	4.3223	0.0842	0.7898	0.0267	170.3	14.8	-13.1	1068
2	15*	5.8090	0.0844	5.7939	0.2298	5.0699	0.2298	5.0830	0.0844	0.9974	0.0481	651.1	#NUM!	-325.5	987
3	1	7.4251	0.1879	5.1089	0.1094	4.3849	0.1094	6.6991	0.1879	0.6546	0.0246	116.1	8.1	-7.5	2729
3	2	4.2028	0.0469	3.7030	0.0681	2.9790	0.0681	3.4768	0.0469	0.8568	0.0228	212.3	18.9	-16.1	828
3	3	8.0179	0.3193	6.7192	0.4337	5.9952	0.4337	7.2919	0.3193	0.8222	0.0695	188.6	54.2	-36.0	968

Chao (Continued)

Set	Pt.	($^{238}U/^{232}Th$)	1s	($^{230}Th/^{232}Th$)	1s	Delta Y	1s	Delta X	1s	m	1s	Age (Ka)	1s -	1s +	U
3	4	4.7113	0.0867	4.1964	0.1251	3.4724	0.1251	3.9853	0.0867	0.8713	0.0367	223.9	36.6	-27.4	468
3	5	8.1387	0.1938	6.2828	0.1263	5.5588	0.1263	7.4127	0.1938	0.7499	0.0260	151.3	12.0	-10.8	2730
3	6	4.9585	0.0658	2.9398	0.1208	2.2158	0.1208	4.2325	0.0658	0.5235	0.0297	81.0	7.0	-6.6	219
3	7	4.4921	0.0484	3.9520	0.0962	3.2280	0.0962	3.7661	0.0484	0.8571	0.0278	212.5	23.6	-19.4	634
3	8	7.3998	0.2033	6.2971	0.1963	5.5731	0.1963	6.6738	0.2033	0.8351	0.0389	196.8	29.4	-23.1	360
3	9	7.1779	0.1673	4.7931	0.1731	4.0691	0.1731	6.4519	0.1673	0.6307	0.0314	108.8	9.7	-8.9	1331
3	10	8.0488	0.1847	7.0963	0.2203	6.3723	0.2203	7.3228	0.1847	0.8702	0.0372	223.0	36.9	-27.5	990
3	11	5.1074	0.0748	4.5751	0.0954	3.8511	0.0954	4.3814	0.0748	0.8790	0.0264	230.6	26.9	-21.6	520
3	12	5.2394	0.0693	4.7655	0.1065	4.0415	0.1065	4.5134	0.0693	0.8954	0.0273	246.6	33.1	-25.3	462
3	13*	5.1327	0.1189	5.0118	0.1338	4.2878	0.1338	4.4067	0.1189	0.9730	0.0401	394.5	#NUM!	-99.5	298
3	14	5.7170	0.2101	4.9865	0.1813	4.2625	0.1813	4.9910	0.2101	0.8540	0.0511	210.1	47.1	-32.8	922
3	15	7.1835	0.2702	4.6645	0.2354	3.9405	0.2354	6.4575	0.2702	0.6102	0.0445	102.9	13.2	-11.8	2546
3	16	5.5541	0.1003	5.2591	0.1247	4.5351	0.1247	4.8281	0.1003	0.9393	0.0324	306.0	83.2	-46.7	655
3	17	4.7478	0.0836	4.2833	0.1243	3.5593	0.1243	4.0218	0.0836	0.8850	0.0360	236.2	41.0	-29.7	501
3	18	4.5118	0.0626	4.0243	0.0747	3.3003	0.0747	3.7858	0.0626	0.8717	0.0244	224.3	23.1	-19.0	621
3	19	9.3045	0.1693	6.1519	0.0708	5.4279	0.0708	8.5785	0.1693	0.6327	0.0150	109.4	4.5	-4.4	2553
3	20	14.4709	1.0983	9.7806	0.8473	9.0566	0.8473	13.7449	1.0983	0.6589	0.0811	117.4	29.6	-23.3	406
3	21	4.3741	0.0727	2.9731	0.0596	2.2491	0.0596	3.6481	0.0727	0.6165	0.0204	104.7	6.0	-5.7	1398
3	22	8.2033	0.1580	6.4426	0.0913	5.7186	0.0913	7.4773	0.1580	0.7648	0.0203	158.0	9.8	-9.0	1327
3	23	4.5399	0.0695	4.2543	0.1255	3.5303	0.1255	3.8139	0.0695	0.9256	0.0370	283.8	75.1	-44.1	257
3	24	5.4557	0.1082	4.6802	0.0728	3.9562	0.0728	4.7297	0.1082	0.8365	0.0246	197.7	17.8	-15.3	1439
3	25	22.1769	0.5176	11.8564	0.2611	11.1324	0.2611	21.4509	0.5176	0.5190	0.0175	79.9	4.0	-3.9	1537

Chillahuita

Set	Pt.	($^{238}U/^{232}Th$)	1s	($^{230}Th/^{232}Th$)	1s	Delta Y	1s	Delta X	1s	m	1s	Age (Ka)	1s -	1s +	U
1	1*	4.4173	0.0707	4.3665	0.1443	3.6425	0.1443	3.6913	0.0707	0.9868	0.0434	472.6	#NUM!	-159.0	981
1	2	8.3303	0.1181	4.8057	0.1515	4.0817	0.1515	7.6043	0.1181	0.5368	0.0216	84.0	5.2	-5.0	505
1	3*	4.3366	0.0546	4.1991	0.1059	3.4751	0.1059	3.6106	0.0546	0.9625	0.0327	358.4	224.8	-68.5	2315
1	4	6.9299	0.3567	4.3427	0.3149	3.6187	0.3149	6.2039	0.3567	0.5833	0.0608	95.6	17.2	-14.9	1032
1	5	4.5095	0.0443	4.1685	0.1102	3.4445	0.1102	3.7835	0.0443	0.9104	0.0310	263.4	46.4	-32.5	1071
1	6	4.5815	0.0411	4.2149	0.1009	3.4909	0.1009	3.8555	0.0411	0.9054	0.0279	257.5	38.2	-28.2	817
1	7	4.5873	0.0444	4.2252	0.0899	3.5012	0.0899	3.8613	0.0444	0.9068	0.0255	259.1	34.9	-26.4	1063

Chillahuita (Continued)

Set	Pt.	($^{238}U/^{232}Th$)	1s	($^{230}Th/^{232}Th$)	1s	Delta Y	1s	Delta X	1s	m	1s	Age (Ka)	1s -	1s +	U
1	8	4.7746	0.0525	4.2898	0.1034	3.5658	0.1034	4.0486	0.0525	0.8808	0.0280	232.2	29.2	-23.0	1013
1	9*	4.8120	0.0562	4.5805	0.0911	3.8565	0.0911	4.0860	0.0562	0.9438	0.0258	314.4	67.1	-41.3	1274
1	10*	4.3078	0.0431	4.0207	0.1304	3.2967	0.1304	3.5818	0.0431	0.9204	0.0381	276.4	71.0	-42.7	462
1	11	4.4807	0.0462	3.9829	0.1118	3.2589	0.1118	3.7547	0.0462	0.8680	0.0316	221.1	29.9	-23.5	610
1	12	4.7256	0.0718	3.0034	0.0741	2.2794	0.0741	3.9996	0.0718	0.5699	0.0212	92.1	5.5	-5.2	598
2	1	5.2619	0.1196	3.6268	0.0926	2.9028	0.0926	4.5359	0.1196	0.6400	0.0265	111.5	8.3	-7.8	4107
2	2	4.3180	0.0677	4.0058	0.0967	3.2818	0.0967	3.5920	0.0677	0.9137	0.0320	267.5	50.5	-34.4	478
2	3	4.7590	0.0628	4.3944	0.1419	3.6704	0.1419	4.0330	0.0628	0.9101	0.0379	263.0	59.9	-38.4	472
2	4	10.8160	0.7104	7.5199	0.3457	6.7959	0.3457	10.0900	0.7104	0.6735	0.0585	122.2	21.6	-18.0	1006
2	5	8.2566	0.2267	5.4640	0.1483	4.7400	0.1483	7.5306	0.2267	0.6294	0.0273	108.4	8.4	-7.8	1321
2	6	4.6551	0.0517	4.2984	0.1061	3.5744	0.1061	3.9291	0.0517	0.9097	0.0295	262.6	43.3	-30.9	515
2	7	5.5203	0.0838	6.0127	0.2378	5.2887	0.2378	4.7943	0.0838	1.1031	0.0532	#NUM!	#NUM!	#NUM!	173
2	8	5.0062	0.1074	3.1889	0.0628	2.4649	0.0628	4.2802	0.1074	0.5759	0.0206	93.7	5.4	-5.2	973
2	9	5.9698	0.1896	4.9937	0.1807	4.2697	0.1807	5.2438	0.1896	0.8142	0.0453	183.8	30.5	-23.8	471
2	10	4.3123	0.0514	3.8183	0.0774	3.0943	0.0774	3.5863	0.0514	0.8628	0.0249	216.9	21.8	-18.2	729
2	11	4.6326	0.0511	4.4324	0.0898	3.7084	0.0898	3.9066	0.0511	0.9493	0.0261	325.5	79.0	-45.3	672
2	12	5.3546	0.1305	4.6172	0.1360	3.8932	0.1360	4.6286	0.1305	0.8411	0.0378	200.9	29.6	-23.3	394
2	13	7.4897	0.1643	6.8160	0.2016	6.0920	0.2016	6.7637	0.1643	0.9007	0.0370	252.2	50.9	-34.6	299
2	14	5.8097	0.1029	5.5505	0.2054	4.8265	0.2054	5.0837	0.1029	0.9494	0.0447	325.8	235.7	-69.2	212
2	16	7.4391	0.2393	5.1895	0.1833	4.4655	0.1833	6.7131	0.2393	0.6652	0.0362	119.5	12.5	-11.2	1276
2	17	5.5147	0.0730	4.6987	0.0820	3.9747	0.0820	4.7887	0.0730	0.8300	0.0213	193.5	14.6	-12.9	957
2	18	5.9080	0.1110	5.6302	0.1948	4.9062	0.1948	5.1820	0.1110	0.9468	0.0427	320.3	177.1	-64.3	266
2	19	9.6136	0.5400	6.9351	0.3109	6.2111	0.3109	8.8876	0.5400	0.6989	0.0550	131.1	22.0	-18.3	1691
2	20	4.5820	0.0620	4.0830	0.1272	3.3590	0.1272	3.8560	0.0620	0.8711	0.0358	223.7	35.6	-26.8	330
2	21	5.9755	0.0636	4.2509	0.1024	3.5269	0.1024	5.2495	0.0636	0.6719	0.0211	121.7	7.3	-6.8	706
3	1	7.0739	0.1559	4.3158	0.1007	3.5918	0.1007	6.3479	0.1559	0.5658	0.0211	91.1	5.4	-5.2	1673
3	2*	6.1974	0.0914	6.3774	0.1844	5.6534	0.1844	5.4714	0.0914	1.0333	0.0379	#NUM!	#NUM!	#NUM!	407
3	3	4.8208	0.0558	4.6470	0.1401	3.9230	0.1401	4.0948	0.0558	0.9580	0.0366	346.2	224.9	-68.5	386
3	4	5.0765	0.0942	3.0944	0.0587	2.3704	0.0587	4.3505	0.0942	0.5449	0.0179	86.0	4.4	-4.2	1779
3	5	6.5092	0.5380	4.8471	0.2295	4.1231	0.2295	5.7832	0.5380	0.7129	0.0773	136.3	34.3	-26.0	645
3	6	6.1412	0.0668	5.5311	0.1469	4.8071	0.1469	5.4152	0.0668	0.8877	0.0293	238.8	33.0	-25.3	517
3	7	4.9697	0.0932	2.9976	0.0845	2.2736	0.0845	4.2437	0.0932	0.5357	0.0231	83.8	5.6	-5.3	931
3	8	10.2737	0.2258	6.6821	0.2474	5.9581	0.2474	9.5477	0.2258	0.6240	0.0298	106.8	9.0	-8.3	646
3	9	4.3573	0.0702	3.7617	0.0691	3.0377	0.0691	3.6313	0.0702	0.8365	0.0250	197.8	18.1	-15.5	1326

Chillahuita (Continued)

Set	Pt.	($^{238}U/^{232}Th$)	1s	($^{230}Th/^{232}Th$)	1s	Delta Y	1s	Delta X	1s	m	1s	Age (Ka)	1s -	1s +	U
3	10	7.7959	0.2412	6.2139	0.2749	5.4899	0.2749	7.0699	0.2412	0.7765	0.0470	163.6	25.8	-20.9	812
3	11	6.4221	0.1508	4.1003	0.1181	3.3763	0.1181	5.6961	0.1508	0.5927	0.0260	98.1	7.2	-6.8	1419
3	12	9.2989	0.8320	5.6438	0.5245	4.9198	0.5245	8.5729	0.8320	0.5739	0.0827	93.1	23.6	-19.4	1126
3	13	4.9753	0.0766	3.0169	0.0566	2.2929	0.0566	4.2493	0.0766	0.5396	0.0165	84.7	4.0	-3.8	962
3	14	7.7173	0.2280	5.1525	0.1175	4.4285	0.1175	6.9913	0.2280	0.6334	0.0266	109.6	8.2	-7.7	1541
3	16	5.3715	0.1713	4.0865	0.1236	3.3625	0.1236	4.6455	0.1713	0.7238	0.0377	140.5	16.0	-14.0	518
3	17	6.1468	0.0818	3.6849	0.0640	2.9609	0.0640	5.4208	0.0818	0.5462	0.0144	86.3	3.5	-3.4	958
3	18	5.8266	0.0949	3.3970	0.0721	2.6730	0.0721	5.1006	0.0949	0.5241	0.0172	81.1	4.0	-3.9	853
3	19	5.8434	0.0733	5.6359	0.1477	4.9119	0.1477	5.1174	0.0733	0.9598	0.0320	351.0	173.6	-63.9	360
3	20	7.3801	0.1837	4.5378	0.1079	3.8138	0.1079	6.6541	0.1837	0.5731	0.0227	93.0	6.0	-5.6	2272
3	22	6.5626	0.2888	5.4949	0.2376	4.7709	0.2376	5.8366	0.2888	0.8174	0.0574	185.7	41.2	-29.8	1735
3	23*	5.0259	0.1101	5.0684	0.1585	4.3444	0.1585	4.2999	0.1101	1.0104	0.0450	#NUM!	#NUM!	#NUM!	342
3	24	5.5288	0.1229	3.5242	0.0993	2.8002	0.0993	4.8028	0.1229	0.5830	0.0255	95.5	6.9	-6.5	1371
3	25	4.3067	0.1172	3.9857	0.1246	3.2617	0.1246	3.5807	0.1172	0.9109	0.0458	264.0	78.8	-45.3	830
3	26	4.6691	0.0922	4.2272	0.1115	3.5032	0.1115	3.9431	0.0922	0.8884	0.0351	239.5	41.2	-29.9	439
3	27*	6.0654	0.1061	5.9014	0.1564	5.1774	0.1564	5.3394	0.1061	0.9697	0.0351	381.7	#NUM!	-83.9	296

Tocopuri

Set	Pt.	($^{238}U/^{232}Th$)	1s	($^{230}Th/^{232}Th$)	1s	Delta Y	1s	Delta X	1s	m	1s	Age (Ka)	1s -	1s +	U
1	1	4.6247	0.0669	4.4356	0.1395	3.7116	0.1395	3.8987	0.0669	0.9520	0.0393	331.6	186.8	-65.3	1537
1	2	3.9389	0.0336	2.6627	0.0598	1.9387	0.0598	3.2129	0.0336	0.6034	0.0196	101.0	5.5	-5.3	829
1	3	4.1320	0.0392	3.9632	0.1414	3.2392	0.1414	3.4060	0.0392	0.9510	0.0429	329.4	228.4	-68.7	626
1	4	4.3308	0.0846	3.2401	0.1549	2.5161	0.1549	3.6048	0.0846	0.6980	0.0460	130.7	18.0	-15.5	1557
1	5	4.9993	0.0704	3.9246	0.0968	3.2006	0.0968	4.2733	0.0704	0.7490	0.0258	150.9	11.8	-10.7	1068
1	6	4.3539	0.1168	3.8913	0.2105	3.1673	0.2105	3.6279	0.1168	0.8731	0.0645	225.4	77.4	-44.8	840
1	7	5.1866	0.0739	3.4793	0.0939	2.7553	0.0939	4.4606	0.0739	0.6177	0.0234	105.0	6.9	-6.5	588
1	8	5.6015	0.0537	3.5051	0.0925	2.7811	0.0925	4.8755	0.0537	0.5704	0.0200	92.3	5.2	-5.0	386
1	9	4.4547	0.0499	3.8118	0.1056	3.0878	0.1056	3.7287	0.0499	0.8281	0.0304	192.3	21.3	-17.8	1153
1	10	4.5239	0.0610	4.8259	0.2134	4.1019	0.2134	3.7979	0.0610	1.0801	0.0588	#NUM!	#NUM!	#NUM!	861
2	1*	4.3039	0.0573	4.1541	0.1275	3.4301	0.1275	3.5779	0.0573	0.9587	0.0388	348.0	305.7	-72.3	428
2	2	4.2758	0.0502	2.9798	0.0741	2.2558	0.0741	3.5498	0.0502	0.6355	0.0227	110.2	7.0	-6.6	678
2	3	3.6493	0.0396	2.6239	0.0531	1.8999	0.0531	2.9233	0.0396	0.6499	0.0202	114.6	6.5	-6.1	969

Tocopuri (Continued)

Set	Pt.	($^{238}U/^{232}Th$)	1s	($^{230}Th/^{232}Th$)	1s	Delta Y	1s	Delta X	1s	m	1s	Age (Ka)	1s -	1s +	U
2	4	4.3994	0.0595	4.0926	0.0959	3.3686	0.0959	3.6734	0.0595	0.9170	0.0300	271.8	49.1	-33.7	615
2	5	4.1410	0.0727	3.4776	0.1277	2.7536	0.1277	3.4150	0.0727	0.8063	0.0412	179.3	26.1	-21.0	653
2	6*	5.4473	0.1985	5.2762	0.2292	4.5522	0.2292	4.7213	0.1985	0.9642	0.0632	363.5	#NUM!	-111.1	451
2	7	4.8293	0.0707	4.6231	0.1551	3.8991	0.1551	4.1033	0.0707	0.9502	0.0412	327.7	192.3	-65.9	440
2	8	4.0005	0.0487	3.0007	0.0802	2.2767	0.0802	3.2745	0.0487	0.6953	0.0266	129.8	10.0	-9.1	714
2	9	4.6354	0.0684	4.0118	0.1159	3.2878	0.1159	3.9094	0.0684	0.8410	0.0331	200.8	25.5	-20.6	490
2	10	8.2398	0.3351	6.0464	0.2168	5.3224	0.2168	7.5138	0.3351	0.7084	0.0428	134.6	17.3	-14.9	3445
2	11*	6.1777	0.0858	5.9743	0.2492	5.2503	0.2492	5.4517	0.0858	0.9631	0.0482	360.2	#NUM!	-91.1	303
2	12	3.9190	0.0509	3.4420	0.0990	2.7180	0.0990	3.1930	0.0509	0.8512	0.0338	208.0	28.2	-22.4	529
2	13	3.8432	0.0444	3.1619	0.0781	2.4379	0.0781	3.1172	0.0444	0.7821	0.0274	166.4	14.7	-12.9	658
2	14	4.0735	0.0460	2.8744	0.0575	2.1504	0.0575	3.3475	0.0460	0.6424	0.0193	112.3	6.1	-5.7	1043
2	15	6.0513	0.0876	5.2274	0.1594	4.5034	0.1594	5.3253	0.0876	0.8457	0.0330	204.0	26.3	-21.2	368
2	16*	5.7788	0.0929	5.7958	0.1890	5.0718	0.1890	5.0528	0.0929	1.0038	0.0417	#NUM!	#NUM!	#NUM!	295
2	17	3.9921	0.0438	2.8130	0.0605	2.0890	0.0605	3.2661	0.0438	0.6396	0.0204	111.4	6.4	-6.0	913
2	18	4.5118	0.0834	3.9492	0.1176	3.2252	0.1176	3.7858	0.0834	0.8519	0.0363	208.6	30.7	-23.9	469
2	19	4.2842	0.0618	3.0893	0.0899	2.3653	0.0899	3.5582	0.0618	0.6647	0.0278	119.3	9.4	-8.7	486
2	20*	6.8885	0.1827	6.8038	0.2456	6.0798	0.2456	6.1625	0.1827	0.9866	0.0494	470.7	#NUM!	-168.6	321
3	1	4.4893	0.0506	3.3974	0.1008	2.6734	0.1008	3.7633	0.0506	0.7104	0.0284	135.3	11.3	-10.2	647
3	2	4.0988	0.0594	3.0401	0.0712	2.3161	0.0712	3.3728	0.0594	0.6867	0.0243	126.7	8.8	-8.2	746
3	4	4.8798	0.0795	3.3428	0.0915	2.6188	0.0915	4.1538	0.0795	0.6305	0.0251	108.7	7.7	-7.2	892
3	5*	6.3547	0.0742	6.3493	0.1935	5.6253	0.1935	5.6287	0.0742	0.9994	0.0368	809.7	#NUM!	-450.9	332
3	6	5.2956	0.1045	4.2544	0.1749	3.5304	0.1749	4.5696	0.1045	0.7726	0.0422	161.7	22.4	-18.6	358
3	7	4.3123	0.0914	2.9242	0.0807	2.2002	0.0807	3.5863	0.0914	0.6135	0.0274	103.8	8.0	-7.5	1481
3	8	3.8600	0.0672	3.0959	0.1176	2.3719	0.1176	3.1340	0.0672	0.7568	0.0409	154.4	20.1	-17.0	661
3	9	3.9555	0.1073	2.8574	0.1194	2.1334	0.1194	3.2295	0.1073	0.6606	0.0430	118.0	14.8	-13.0	785
3	10	4.4809	0.0694	4.0292	0.1307	3.3052	0.1307	3.7549	0.0694	0.8802	0.0384	231.7	42.2	-30.4	325
3	11	4.3460	0.1342	3.4458	0.1634	2.7218	0.1634	3.6200	0.1342	0.7519	0.0530	152.2	26.3	-21.2	411
3	12	4.5483	0.1012	4.2245	0.1679	3.5005	0.1679	3.8223	0.1012	0.9158	0.0502	270.2	98.9	-51.0	314
3	13	4.2505	0.0570	3.6117	0.0806	2.8877	0.0806	3.5245	0.0570	0.8193	0.0264	186.8	17.3	-14.9	543
3	14	5.2816	0.1307	4.8400	0.1762	4.1160	0.1762	4.5556	0.1307	0.9035	0.0466	255.3	72.0	-43.0	368
3	15	3.8376	0.0452	2.6494	0.0547	1.9254	0.0547	3.1116	0.0452	0.6188	0.0198	105.3	5.8	-5.5	762
3	16	4.6747	0.0830	4.4214	0.0955	3.6974	0.0955	3.9487	0.0830	0.9364	0.0312	300.8	73.5	-43.5	427
3	17	7.9645	0.5739	7.3619	0.5171	6.6379	0.5171	7.2385	0.5739	0.9170	0.1019	271.8	#NUM!	-87.5	492
3	18	4.5034	0.0532	3.6935	0.0674	2.9695	0.0674	3.7774	0.0532	0.7861	0.0210	168.4	11.3	-10.2	763

Tocopuri (Continued)

Set	Pt.	($^{238}U/^{232}Th$)	1s	($^{230}Th/^{232}Th$)	1s	Delta Y	1s	Delta X	1s	m	1s	Age (Ka)	1s -	1s +	U
3	19*	4.5989	0.1140	4.7049	0.1791	3.9809	0.1791	3.8729	0.1140	1.0279	0.0553	#NUM!	#NUM!	#NUM!	297
3	20*	4.9641	0.0912	5.0740	0.1223	4.3500	0.1223	4.2381	0.0912	1.0264	0.0364	#NUM!	#NUM!	#NUM!	376
3	21*	5.4614	0.1482	5.4505	0.2164	4.7265	0.2164	4.7354	0.1482	0.9981	0.0553	685.8	#NUM!	-373.4	446
3	22*	4.9669	0.0947	5.0013	0.0983	4.2773	0.0983	4.2409	0.0947	1.0086	0.0323	#NUM!	#NUM!	#NUM!	947
3	23	4.1297	0.0597	3.1698	0.0671	2.4458	0.0671	3.4037	0.0597	0.7186	0.0234	138.4	9.5	-8.7	761
3	24	4.0539	0.0452	2.7741	0.0622	2.0501	0.0622	3.3279	0.0452	0.6160	0.0205	104.5	6.0	-5.7	621

Chanka

Set	Pt.	($^{238}U/^{232}Th$)	1s	($^{230}Th/^{232}Th$)	1s	Delta Y	1s	Delta X	1s	m	1s	Age (Ka)	1s -	1s +	U
1*	1	6.0963	0.1018	6.1453	0.1405	5.4213	0.1405	5.3703	0.1018	1.0095	0.0324	#NUM!	#NUM!	#NUM!	571
1	2	6.2058	0.1159	5.9555	0.1579	5.2315	0.1579	5.4798	0.1159	0.9547	0.0352	337.8	163.5	-62.7	600
1	3	3.8235	0.0481	3.5707	0.0699	2.8467	0.0699	3.0975	0.0481	0.9190	0.0267	274.5	43.7	-31.1	969
1	4	4.1831	0.0561	4.0113	0.0872	3.2873	0.0872	3.4571	0.0561	0.9509	0.0296	329.1	100.7	-51.5	614
1	5*	5.6833	0.1870	5.6868	0.1866	4.9628	0.1866	4.9573	0.1870	1.0011	0.0533	#NUM!	#NUM!	#NUM!	879
1	6*	4.5539	0.1054	4.5790	0.1329	3.8550	0.1329	3.8279	0.1054	1.0071	0.0444	#NUM!	#NUM!	#NUM!	579
1	7	4.7534	0.0586	3.8663	0.1055	3.1423	0.1055	4.0274	0.0586	0.7802	0.0286	165.4	15.2	-13.3	497
1	8*	5.3855	0.0773	5.3021	0.1312	4.5781	0.1312	4.6595	0.0773	0.9825	0.0325	442.0	#NUM!	-114.8	467
1	9	4.2196	0.0512	3.3549	0.0804	2.6309	0.0804	3.4936	0.0512	0.7530	0.0255	152.7	11.9	-10.7	1037
1	10	4.2561	0.0490	3.8750	0.0865	3.1510	0.0865	3.5301	0.0490	0.8926	0.0274	243.6	32.2	-24.9	673
1	11	4.2196	0.0521	3.0936	0.0682	2.3696	0.0682	3.4936	0.0521	0.6783	0.0220	123.8	7.7	-7.2	747
1	12	5.9502	0.0744	3.3455	0.0700	2.6215	0.0700	5.2242	0.0744	0.5018	0.0152	76.1	3.4	-3.3	1597
1	13	4.8686	0.0554	4.6517	0.1115	3.9277	0.1115	4.1426	0.0554	0.9481	0.0298	323.1	93.1	-49.5	525
1	14	5.1018	0.1146	4.5658	0.1263	3.8418	0.1263	4.3758	0.1146	0.8780	0.0369	229.7	39.3	-28.9	834
1	15	4.7983	0.0662	4.0747	0.1177	3.3507	0.1177	4.0723	0.0662	0.8228	0.0319	189.0	21.6	-18.1	493
1	16	6.7565	0.1095	6.2260	0.1446	5.5020	0.1446	6.0305	0.1095	0.9124	0.0291	265.8	44.1	-31.3	600
1	18	4.8096	0.1115	3.0186	0.0766	2.2946	0.0766	4.0836	0.1115	0.5619	0.0242	90.1	6.2	-5.9	855
1	19	4.2618	0.0541	3.9660	0.0871	3.2420	0.0871	3.5358	0.0541	0.9169	0.0284	271.7	45.6	-32.1	623
1	20	6.1496	0.1273	3.6131	0.0721	2.8891	0.0721	5.4236	0.1273	0.5327	0.0183	83.1	4.4	-4.2	1493
1	21	6.3716	0.0996	3.9762	0.1035	3.2522	0.1035	5.6456	0.0996	0.5761	0.0210	93.7	5.5	-5.3	1536
1	22*	3.8432	0.0532	3.8120	0.0746	3.0880	0.0746	3.1172	0.0532	0.9906	0.0293	510.1	#NUM!	-154.9	730
1	23	4.2786	0.0476	4.0231	0.0820	3.2991	0.0820	3.5526	0.0476	0.9286	0.0262	288.3	50.0	-34.2	658
2	1*	8.2117	0.1178	8.3201	0.2889	7.5961	0.2889	7.4857	0.1178	1.0148	0.0418	#NUM!	#NUM!	#NUM!	238

Chanka (Continued)

Set	Pt.	($^{238}U/^{232}Th$)	1s	($^{230}Th/^{232}Th$)	1s	Delta Y	1s	Delta X	1s	m	1s	Age (Ka)	1s -	1s +	U
2	2*	4.8517	0.1014	4.7728	0.1409	4.0488	0.1409	4.1257	0.1014	0.9814	0.0418	434.9	#NUM!	-128.4	366
2	3	4.9079	0.0709	4.7015	0.1222	3.9775	0.1222	4.1819	0.0709	0.9511	0.0334	329.6	125.4	-56.8	467
2	4*	4.6635	0.0557	4.7423	0.1199	4.0183	0.1199	3.9375	0.0557	1.0205	0.0337	#NUM!	#NUM!	#NUM!	512
2	5*	5.0062	0.1221	4.6551	0.1669	3.9311	0.1669	4.2802	0.1221	0.9184	0.0470	273.7	93.7	-49.7	456
2	6	4.2000	0.0593	3.9051	0.0880	3.1811	0.0880	3.4740	0.0593	0.9157	0.0298	270.1	47.6	-33.0	646
2	7	4.1157	0.0439	4.1826	0.0817	3.4586	0.0817	3.3897	0.0439	1.0203	0.0275	#NUM!	#NUM!	#NUM!	848
2	8	4.5848	0.0544	4.0375	0.0935	3.3135	0.0935	3.8588	0.0544	0.8587	0.0271	213.7	23.2	-19.1	624
2	9	4.2786	0.0677	3.7657	0.0933	3.0417	0.0933	3.5526	0.0677	0.8562	0.0309	211.8	26.4	-21.3	588
2	10	6.3716	0.0969	5.8296	0.1395	5.1056	0.1395	5.6456	0.0969	0.9044	0.0292	256.3	39.8	-29.1	595
3	1*	5.2029	0.1186	5.1850	0.1731	4.4610	0.1731	4.4769	0.1186	0.9964	0.0468	615.7	#NUM!	-289.4	291
3	3	4.1606	0.0467	4.0396	0.0698	3.3156	0.0698	3.4346	0.0467	0.9654	0.0242	367.2	130.8	-57.8	844
3	4	4.0932	0.0983	3.1214	0.0800	2.3974	0.0800	3.3672	0.0983	0.7120	0.0316	135.9	12.7	-11.4	933
3	5	5.1102	0.0693	3.4193	0.0652	2.6953	0.0652	4.3842	0.0693	0.6148	0.0178	104.2	5.2	-4.9	834
3	6	6.2901	0.0721	6.4950	0.1711	5.7710	0.1711	5.5641	0.0721	1.0372	0.0336	#NUM!	#NUM!	#NUM!	359
3	7	4.6579	0.0825	4.4946	0.1081	3.7706	0.1081	3.9319	0.0825	0.9590	0.0341	348.7	193.6	-66.0	673
3	8	4.2983	0.0757	3.7620	0.0767	3.0380	0.0767	3.5723	0.0757	0.8504	0.0280	207.5	22.6	-18.7	642
3	9	6.6413	0.1256	6.2917	0.1399	5.5677	0.1399	5.9153	0.1256	0.9412	0.0310	309.5	81.7	-46.2	468
3	11*	4.9697	0.1017	4.9370	0.1335	4.2130	0.1335	4.2437	0.1017	0.9928	0.0394	538.3	#NUM!	-203.6	489
3	12	5.3827	0.0872	3.1827	0.0508	2.4587	0.0508	4.6567	0.0872	0.5280	0.0147	82.0	3.5	-3.4	1900
3	13	4.4697	0.0524	3.9268	0.0880	3.2028	0.0880	3.7437	0.0524	0.8555	0.0264	211.3	22.0	-18.3	640
3	14	6.1665	0.0987	5.1231	0.1046	4.3991	0.1046	5.4405	0.0987	0.8086	0.0242	180.5	14.7	-13.0	600
3	15	4.6860	0.0607	4.5384	0.0925	3.8144	0.0925	3.9600	0.0607	0.9633	0.0276	360.7	152.3	-61.2	555

Chascon

Set	Pt.	($^{238}U/^{232}Th$)	1s	($^{230}Th/^{232}Th$)	1s	Delta Y	1s	Delta X	1s	m	1s	Age (Ka)	1s -	1s +	U
1	1	13.9952	0.4935	12.6483	0.5300	11.9243	0.5300	13.2692	0.4935	0.8986	0.0521	250.0	78.8	-45.3	673
1	2	10.6844	0.3493	6.9475	0.2521	6.2235	0.2521	9.9584	0.3493	0.6249	0.0335	107.1	10.2	-9.3	271
1	4	10.5375	0.1856	8.6780	0.2580	7.9540	0.2580	9.8115	0.1856	0.8107	0.0304	181.7	19.1	-16.3	1202
1	5	8.6127	0.2162	7.4672	0.1919	6.7432	0.1919	7.8867	0.2162	0.8550	0.0338	210.9	29.0	-22.9	1420
1	6	9.6471	0.5020	10.5717	0.6934	9.8477	0.6934	8.9211	0.5020	1.1039	0.0995	#NUM!	#NUM!	#NUM!	1565
1	7	13.9145	1.0630	10.6605	0.7446	9.9365	0.7446	13.1885	1.0630	0.7534	0.0829	152.9	44.8	-31.7	2201
1	9	13.1538	0.3795	10.4959	0.4327	9.7719	0.4327	12.4278	0.3795	0.7863	0.0423	168.5	24.1	-19.7	707

Chascon (Continued)

Set	Pt.	($^{238}U/^{232}Th$)	1s	($^{230}Th/^{232}Th$)	1s	Delta Y	1s	Delta X	1s	m	1s	Age (Ka)	1s -	1s +	U
1	10	10.6441	0.2887	9.2610	0.2725	8.5370	0.2725	9.9181	0.2887	0.8608	0.0372	215.3	33.9	-25.8	1565
1	11	9.8113	0.2653	10.2895	0.3957	9.5655	0.3957	9.0853	0.2653	1.0529	0.0533	#NUM!	#NUM!	#NUM!	1460
1	12	6.8665	0.2783	6.3870	0.2463	5.6630	0.2463	6.1405	0.2783	0.9222	0.0579	278.9	149.2	-60.8	1785
1	13	7.6531	0.2220	6.6097	0.2104	5.8857	0.2104	6.9271	0.2220	0.8497	0.0408	206.9	34.6	-26.2	171
1	14	8.6761	0.1310	6.4627	0.2058	5.7387	0.2058	7.9501	0.1310	0.7218	0.0285	139.7	11.8	-10.6	581
1	15	5.6217	0.3488	4.7124	0.2961	3.9884	0.2961	4.8957	0.3488	0.8147	0.0838	184.1	65.7	-40.7	995
1	16	7.6589	0.0789	6.4161	0.1517	5.6921	0.1517	6.9329	0.0789	0.8210	0.0238	187.9	15.6	-13.6	856
1	17	5.9444	0.4029	4.8881	0.3097	4.1641	0.3097	5.2184	0.4029	0.7980	0.0855	174.6	60.1	-38.5	1747
1	18	8.1804	0.2486	6.2417	0.1982	5.5177	0.1982	7.4544	0.2486	0.7402	0.0363	147.2	16.4	-14.3	1302
1	19	15.7788	0.2105	16.1767	0.4564	15.4527	0.4564	15.0528	0.2105	1.0266	0.0335	#NUM!	#NUM!	#NUM!	816
2	1	11.0576	0.3448	9.3914	0.2616	8.6674	0.2616	10.3316	0.3448	0.8389	0.0378	199.4	29.2	-23.0	1713
2	2	13.9399	0.3237	12.5881	0.3410	11.8641	0.3410	13.2139	0.3237	0.8979	0.0339	249.1	44.0	-31.3	850
2	3*	12.2515	0.4368	12.2355	0.3700	11.5115	0.3700	11.5255	0.4368	0.9988	0.0496	732.5	#NUM!	-407.3	1943
2	4	9.7905	0.4038	9.0529	0.3075	8.3289	0.3075	9.0645	0.4038	0.9188	0.0532	274.2	116.2	-55.0	809
2	5	13.7320	0.3448	10.9901	0.2657	10.2661	0.2657	13.0060	0.3448	0.7893	0.0292	170.1	16.3	-14.2	1735
2	6	11.2542	0.4957	9.2579	0.2991	8.5339	0.2991	10.5282	0.4957	0.8106	0.0476	181.7	31.6	-24.5	991
2	7	14.4625	0.5986	11.9782	0.3878	11.2542	0.3878	13.7365	0.5986	0.8193	0.0455	186.8	31.7	-24.5	1283
2	8	13.9821	0.1727	13.2116	0.1671	12.4876	0.1671	13.2561	0.1727	0.9420	0.0176	311.0	39.5	-28.9	1701
2	9	6.8576	0.1891	6.5411	0.1730	5.8171	0.1730	6.1316	0.1891	0.9487	0.0406	324.3	171.6	-63.7	727
2	10	11.5829	0.1451	10.5294	0.1704	9.8054	0.1704	10.8569	0.1451	0.9032	0.0198	254.9	25.0	-20.3	1131
2	11	8.5292	0.1379	7.4054	0.1711	6.6814	0.1711	7.8032	0.1379	0.8562	0.0266	211.8	22.4	-18.6	1129
2	12*	7.8746	0.5810	7.6877	0.5143	6.9637	0.5143	7.1486	0.5810	0.9741	0.1070	399.1	#NUM!	-178.7	784
2	13	10.8047	0.2208	10.1409	0.2079	9.4169	0.2079	10.0787	0.2208	0.9343	0.0291	297.4	63.8	-40.0	1463
2	14	12.1054	0.4640	10.4607	0.3949	9.7367	0.3949	11.3794	0.4640	0.8556	0.0492	211.3	45.5	-32.0	928
2	15	12.3274	0.1551	11.9024	0.1580	11.1784	0.1580	11.6014	0.1551	0.9635	0.0187	361.6	78.8	-45.3	1458
2	16	15.9908	0.6467	13.3611	0.5897	12.6371	0.5897	15.2648	0.6467	0.8279	0.0522	192.1	39.4	-28.9	1406
2	17	4.5596	0.0748	4.0896	0.1543	3.3656	0.1543	3.8336	0.0748	0.8779	0.0437	229.7	48.4	-33.4	310
2	18	9.7372	0.1811	8.4404	0.1284	7.7164	0.1284	9.0112	0.1811	0.8563	0.0223	211.9	18.5	-15.8	1360
3	1	10.2681	0.2749	9.3036	0.2061	8.5796	0.2061	9.5421	0.2749	0.8991	0.0337	250.5	44.5	-31.5	1297
3	2	12.5072	0.3711	8.8434	0.3046	8.1194	0.3046	11.7812	0.3711	0.6892	0.0338	127.6	12.6	-11.3	1306
3	3	3.1830	0.0610	2.5094	0.0675	1.7854	0.0675	2.4570	0.0610	0.7267	0.0329	141.6	14.0	-12.4	570
3	4	10.3075	0.1464	9.4328	0.2436	8.7088	0.2436	9.5815	0.1464	0.9089	0.0290	261.6	41.8	-30.2	466
3	5	7.1245	0.3468	4.9659	0.2328	4.2419	0.2328	6.3985	0.3468	0.6630	0.0511	118.8	18.0	-15.4	470
3	6	15.0215	0.3612	11.2432	0.3975	10.5192	0.3975	14.2955	0.3612	0.7358	0.0334	145.4	14.8	-13.0	863

Chascon (Continued)

Set	Pt.	($^{238}U/^{232}Th$)	1s	($^{230}Th/^{232}Th$)	1s	Delta Y	1s	Delta X	1s	m	1s	Age (Ka)	1s -	1s +	U
3	7	8.9253	0.1729	6.2913	0.2344	5.5673	0.2344	8.1993	0.1729	0.6790	0.0320	124.1	11.5	-10.4	511
3	8*	17.3224	0.4430	16.7900	0.4728	16.0660	0.4728	16.5964	0.4430	0.9680	0.0385	376.0	#NUM!	-86.3	946
3	9	10.6671	0.2574	9.1270	0.2375	8.4030	0.2375	9.9411	0.2574	0.8453	0.0324	203.8	25.7	-20.8	892
3	10	9.4113	0.2557	7.2282	0.2100	6.5042	0.2100	8.6853	0.2557	0.7489	0.0327	150.9	15.2	-13.4	2122
3	11*	9.2118	0.2763	9.2813	0.2396	8.5573	0.2396	8.4858	0.2763	1.0084	0.0433	#NUM!	#NUM!	#NUM!	1492
3	12	5.6215	0.2645	4.7320	0.1951	4.0080	0.1951	4.8955	0.2645	0.8187	0.0595	186.5	43.5	-31.0	1768
3	13	6.1665	0.1847	4.6070	0.1172	3.8830	0.1172	5.4405	0.1847	0.7137	0.0324	136.6	13.1	-11.7	686
3	14	8.4280	0.4392	7.0405	0.3251	6.3165	0.3251	7.7020	0.4392	0.8201	0.0630	187.3	47.1	-32.8	984
3	15	8.7342	0.1077	8.4431	0.1328	7.7191	0.1328	8.0082	0.1077	0.9639	0.0210	362.7	95.5	-50.2	985
3	16*	8.3690	0.2264	8.2856	0.2180	7.5616	0.2180	7.6430	0.2264	0.9893	0.0409	495.9	#NUM!	-172.2	787
3	17*	5.6412	0.1842	5.5016	0.1989	4.7776	0.1989	4.9152	0.1842	0.9720	0.0544	390.5	#NUM!	-118.0	625
3	19	8.0038	0.1385	7.6597	0.1628	6.9357	0.1628	7.2778	0.1385	0.9530	0.0288	333.9	103.6	-52.2	1800
3	20	6.5654	0.2971	5.7737	0.3252	5.0497	0.3252	5.8394	0.2971	0.8648	0.0710	218.5	81.2	-46.1	773

Appendix E: Zircon U-Pb Data

Chao

Set	Pt.	Core/Rim	*238U/ 206Pb*	*238U/ 206Pb*	*207Pb*/ 206Pb**	*207Pb*/ 206Pb**	Correlation of TW Concordia Ellipses	*206/238 age (Ma)*	±1s (Ma)	*U ppm*	*UO/U*	*% 206Pb**
1	2	Rim	8888.9	373.7	0.1543	0.0141	0.09	0.72	0.03	1145	8.1	86.2
1	2	Core	5830.9	274.4	0.1289	0.0176	-0.05	1.07	0.06	492	8.3	89.4
1	6	Rim	24260.1	2071.7	0.2300	0.0350	0.04	0.29	0.03	916	8.2	76.5
1	6	Core	9157.5	681.8	0.2755	0.0333	-0.37	0.58	0.07	743	8.0	70.7
1	8	Rim	6297.2	362.1	0.1243	0.0196	0.10	1.01	0.06	299	8.3	90.0
1	8	Core	5216.5	228.9	0.0947	0.0137	-0.08	1.26	0.06	832	7.9	93.8
1	12	Rim	8032.1	402.6	0.1256	0.0276	0.02	0.81	0.05	607	8.1	89.8
1	12	Core	293.9	10.5	0.7726	0.0075	0.01	1.64	1.08	1715	7.9	7.1
1	13	Rim	4659.8	225.8	0.0897	0.0098	-0.18	1.40	0.07	833	8.2	94.4
1	13	Core	4442.5	201.3	0.0791	0.0086	0.27	1.47	0.07	828	8.0	95.8
2	4	Rim	6858.7	297.8	0.1265	0.0123	0.04	0.93	0.04	928	7.8	89.7
2	4	Core	4198.2	204.4	0.1549	0.0101	-0.10	1.40	0.08	1099	7.8	86.1
2	7	Rim	8210.2	401.1	0.2854	0.0280	0.28	0.63	0.05	644	8.1	69.4
2	7	Core	8741.3	400.4	0.1126	0.0143	-0.03	0.76	0.04	766	7.9	91.5
2	9	Rim	3471.0	179.5	0.3672	0.0305	0.30	1.18	0.12	466	7.5	58.9
2	10	Rim	3766.5	146.1	0.4354	0.0224	-0.06	0.95	0.09	715	8.3	50.2
2	10	Core	5948.8	234.3	0.2095	0.0159	-0.07	0.94	0.05	847	8.2	79.1
2	15	Rim	6493.5	322.1	0.1883	0.0190	-0.11	0.90	0.06	674	8.2	81.8
2	15	Core	3013.9	368.8	0.2873	0.0538	-0.53	1.54	0.34	896	8.0	69.1
3	13	Rim	28677.9	2426.2	0.5494	0.0765	0.26	0.17	0.03	1527	8.0	35.7
3	13	Core	16005.1	1019.5	0.5179	0.0875	0.27	0.25	0.05	715	8.4	39.7

Chillahuita

Set	Pt.	Core/Rim	*238U/ 206Pb*	*238U/ 206Pb*	*207Pb*/ 206Pb**	*207Pb*/ 206Pb**	Correlation of TW Concordia Ellipses	*206/238 age (Ma)*	±1s (Ma)	*U ppm*	*UO/U*	*% 206Pb**
1	1	Rim	299.8	18.6	0.8320	0.0175	-0.04	-0.01	1.99	696	7.5	-0.5
1	1	Core	6544.5	591.1	0.4452	0.0298	-0.12	0.56	0.11	513	7.7	49.0
1	3	Rim	23293.7	1568.1	0.2426	0.0536	0.05	0.30	0.03	697	8.0	74.9
1	3	Core	10515.2	508.6	0.1436	0.0256	0.02	0.61	0.04	739	8.1	87.5
1	9	Rim	19908.4	1347.6	0.3319	0.0407	-0.24	0.30	0.03	647	7.9	63.5
1	9	Core	10296.5	504.6	0.1362	0.0167	-0.19	0.64	0.03	701	8.0	88.5
1	10	Rim	8865.2	427.5	0.1029	0.0130	-0.01	0.77	0.04	688	8.2	92.7
1	10	Core	5221.9	222.8	0.0776	0.0089	-0.04	1.27	0.05	720	8.1	96.0
3	2	Rim	5099.4	240.3	0.1599	0.0212	-0.13	1.17	0.07	845	8.1	85.4
3	2	Core	5834.3	233.2	0.1236	0.0181	0.16	1.08	0.05	1113	8.4	90.1
3	23	Rim	16207.5	1352.8	0.4113	0.0739	0.11	0.30	0.05	941	8.1	53.3
3	23	Core	13094.1	632.7	0.2479	0.0495	0.12	0.44	0.04	1294	8.4	74.2
3	27	Rim	3360.2	120.8	0.1245	0.0147	0.12	1.81	0.08	736	8.2	90.0
3	27	Core	2651.1	81.5	0.4482	0.0236	-0.17	1.26	0.12	1082	8.2	48.6

Tocopuri

Set	Pt.	Core/Rim	*238U/ 206Pb*	*238U/ 206Pb*	*207Pb*/ 206Pb**	*207Pb*/ 206Pb**	Correlation of TW Concordia Ellipses	*206/238 age (Ma)*	±1s (Ma)	*U ppm*	*UO/U*	*% 206Pb**
2	1	Rim	5861.7	618.5	0.4003	0.0809	0.51	0.69	0.15	486	7.4	54.7
2	1	Core	6514.7	414.6	0.2853	0.0384	0.00	0.77	0.08	453	8.2	69.4
2	6	Rim	4189.4	210.6	0.1561	0.0198	0.32	1.42	0.08	1487	7.2	85.9
2	6	Core	4185.9	158.6	0.2137	0.0389	-0.14	1.31	0.10	718	8.5	78.6
2	11	Rim	6064.3	434.0	0.3084	0.0638	-0.34	0.80	0.12	434	7.6	66.5
2	11	Core	4887.6	222.9	0.1273	0.0202	-0.04	1.27	0.07	597	8.2	89.6
2	16	Rim	4807.7	284.3	0.2455	0.0449	0.00	1.10	0.11	638	7.5	74.5
2	20	Rim	3410.6	216.4	0.2482	0.0412	0.31	1.50	0.15	447	7.4	74.2
2	20	Core	2911.2	147.5	0.1986	0.0322	0.31	1.87	0.14	252	8.5	80.5
3	5	Rim	7657.0	791.5	0.2691	0.0829	0.72	0.70	0.11	682	7.5	71.5
3	5	Core	9354.5	520.7	0.2574	0.0454	0.49	0.58	0.05	618	8.6	73.0
3	19	Rim	5672.1	305.0	0.2017	0.0306	-0.13	1.00	0.08	822	7.4	80.1
3	19	Core	5467.5	171.6	0.0877	0.0130	0.10	1.17	0.04	1371	8.3	94.7
3	20	Rim	7304.6	437.0	0.2457	0.0335	0.12	0.75	0.06	787	7.7	74.5
3	20	Core	1870.6	161.7	0.7135	0.0457	-0.06	0.60	0.45	469	8.3	14.7

Tocopuri (Continued)

Set	Pt.	Core/Rim	*238U/ 206Pb*	*238U/ 206Pb*	*207Pb*/ 206Pb**	*207Pb*/ 206Pb**	Correlation of TW Concordia Ellipses	*206/238 age (Ma)*	±1s (Ma)	*U ppm*	*UO/U*	*% 206Pb**
3	21	Rim	12998.8	1101.7	0.4540	0.0514	-0.24	0.33	0.06	830	7.3	47.9
3	22	Rim	9017.1	404.1	0.2291	0.0323	-0.10	0.64	0.04	1323	8.1	76.6
3	22	Core	6068.0	213.2	0.1217	0.0192	0.00	1.05	0.04	1072	8.3	90.3

Chanka

Set	Pt.	Core/Rim	*238U/ 206Pb*	*238U/ 206Pb*	*207Pb*/ 206Pb**	*207Pb*/ 206Pb**	Correlation of TW Concordia Ellipses	*206/238 age (Ma)*	±1s (Ma)	*U ppm*	*UO/U*	*% 206Pb**
1	1	Rim	9901.0	458.8	0.2265	0.0290	-0.07	0.58	0.04	994	8.3	76.9
1	1	Core	656.2	24.9	0.7937	0.0430	0.29	0.52	0.63	254	8.4	4.5
1	5	Rim	9337.1	427.2	0.2158	0.0306	0.36	0.62	0.04	897	8.3	78.3
1	5	Core	8673.0	302.4	0.1354	0.0165	-0.08	0.75	0.03	2038	8.3	88.6
1	6	Rim	12789.4	611.7	0.2303	0.0283	-0.03	0.46	0.03	1434	8.4	76.4
1	6	Core	2868.6	243.6	0.5755	0.0181	-0.09	0.81	0.25	3000	8.3	32.3
1	8	Rim	29797.4	2175.3	0.3851	0.0469	-0.03	0.20	0.02	1640	8.4	56.7
1	8	Core	17015.5	990.2	0.3233	0.0470	-0.29	0.33	0.03	1359	8.4	64.6
1	22	Rim	6540.2	329.4	0.4508	0.0340	-0.26	0.56	0.08	837	8.5	48.3
1	22	Core	9871.7	510.6	0.2032	0.0359	0.08	0.61	0.04	965	8.1	79.9
2	1	Rim	13328.0	627.1	0.2493	0.0290	-0.13	0.44	0.03	1456	8.4	74.0
2	1	Core	10064.4	369.7	0.1580	0.0215	-0.41	0.62	0.03	1600	8.3	85.7
2	2	Rim	13025.9	765.2	0.3813	0.0589	-0.08	0.37	0.05	771	8.2	57.1
2	2	Core	11495.6	491.6	0.1574	0.0269	-0.31	0.55	0.03	1765	8.6	85.8
2	4	Rim	11841.3	717.9	0.2713	0.0374	0.00	0.48	0.04	739	8.1	71.2
2	4	Core	5707.8	208.5	0.2090	0.0236	-0.39	0.98	0.06	1324	8.3	79.2
2	5	Rim	7558.6	529.0	0.6463	0.1060	0.87	0.29	0.10	367	8.0	23.3
2	5	Core	10622.5	453.6	0.1282	0.0285	-0.26	0.61	0.03	1492	8.3	89.5
3	1	Rim	9025.3	584.0	0.3444	0.0513	0.39	0.53	0.06	890	8.0	61.9
3	11	Rim	12566.0	1217.4	0.3447	0.0336	-0.12	0.41	0.06	769	8.0	61.8

Chascon

Set	Pt.	Core/Rim	*238U/ 206Pb*	*238U/ 206Pb*	*207Pb*/ 206Pb**	*207Pb*/ 206Pb**	Correlation of TW Concordia Ellipses	*206/238 age (Ma)*	±1s (Ma)	*U ppm*	*UO/U*	*% 206Pb**
2	3	Rim	14072.6	354.5	0.1069	0.0109	0.08	0.51	0.01	7405	8.4	92.2
2	3	Rim	14619.9	256.5	0.0903	0.0058	-0.08	0.51	0.01	15652	9.0	94.3
2	12	Core	4353.5	98.4	0.0704	0.0084	0.25	1.52	0.04	2672	8.6	96.9
3	8	Rim	14349.3	700.1	0.1536	0.0142	-0.15	0.48	0.02	2927	8.4	86.3
3	8	Core	1781.6	45.4	0.1015	0.0061	-0.11	3.46	0.10	1811	8.6	92.9
3	11	Rim	136.4	3.3	0.8285	0.0104	-0.05	0.03	1.78	905	8.0	0.0
3	11	Core	7132.7	702.1	0.4555	0.0639	0.04	0.50	0.12	333	8.2	47.7
3	16	Rim	15398.8	436.3	0.1610	0.0170	0.11	0.44	0.01	4342	8.4	85.3
3	17	Rim	19984.0	690.9	0.1963	0.0221	-0.34	0.36	0.01	4357	8.4	80.8

Chascon Granite

Set	Pt.	Core/Rim	*238U/ 206Pb*	*238U/ 206Pb*	*207Pb*/ 206Pb**	*207Pb*/ 206Pb**	Correlation of TW Concordia Ellipses	*206/238 age (Ma)*	±1s (Ma)	*U ppm*	*UO/U*	*% 206Pb**
1	1	Rim	2537.4	112.7	0.0675	0.0066	0.05	2.56	0.11	1042	8.1	97.3
1	1	Core	2529.7	96.6	0.0768	0.0053	0.01	2.52	0.10	1225	8.0	96.1
1	2	Core	3110.4	141.3	0.0674	0.0056	-0.24	2.11	0.10	1312	7.9	97.3
1	4	Core	2591.3	97.4	0.0636	0.0046	0.09	2.53	0.09	1079	8.2	97.8
1	5	Rim	2852.3	104.9	0.0511	0.0042	0.14	2.34	0.08	1545	8.1	99.4
1	5	Core	2427.8	112.0	0.0666	0.0051	0.01	2.67	0.12	826	8.1	97.4
1	6	Core	2649.0	94.7	0.0502	0.0040	0.10	2.51	0.09	1292	8.1	99.5
1	7	Rim	2549.7	92.3	0.0664	0.0059	0.02	2.55	0.09	974	8.2	97.4
1	7	Core	1681.5	108.9	0.1986	0.0347	-0.31	3.18	0.31	214	7.9	80.5
1	8	Rim	2657.5	108.8	0.0611	0.0059	0.04	2.47	0.10	875	8.3	98.1
1	8	Core	2386.6	67.2	0.0617	0.0029	0.00	2.72	0.08	2201	8.6	98.0
1	9	Rim	2490.0	86.2	0.0602	0.0051	-0.12	2.63	0.09	1363	8.3	98.2
1	9	Core	2395.2	71.1	0.0639	0.0049	-0.07	2.72	0.08	1523	8.5	97.7
1	10	Rim	1872.0	76.0	0.2225	0.0094	-0.11	2.74	0.15	1056	8.2	77.4
1	10	Core	2358.5	88.4	0.0671	0.0060	0.03	2.74	0.10	528	8.2	97.3
1	11	Rim	2321.3	93.8	0.0668	0.0095	-0.04	2.80	0.12	492	8.3	97.4
1	11	Core	2284.1	114.3	0.0820	0.0082	-0.30	2.77	0.15	295	8.5	95.4
1	12	Rim	560.5	45.6	0.6614	0.0200	-0.18	2.54	1.35	645	8.6	21.4
1	12	Core	2339.2	85.4	0.0557	0.0061	-0.32	2.79	0.10	854	8.4	98.8
1	13	Core	2488.8	90.4	0.0665	0.0091	-0.12	2.60	0.10	600	8.4	97.4

Chascon Granite (Continued)

Set	Pt.	Core/Rim	*238U/ 206Pb*	*238U/ 206Pb*	*207Pb*/ 206Pb**	*207Pb*/ 206Pb**	Correlation of TW Concordia Ellipses	*206/238 age (Ma)*	±1s (Ma)	*U ppm*	*UO/U*	*% 206Pb**
1	13	Rim	2533.6	91.8	0.0579	0.0039	-0.06	2.58	0.09	2558	8.6	98.5
1	14	Rim	577.0	24.3	0.0589	0.0023	-0.04	11.08	0.47	1133	8.1	98.4
1	14	Core	10.2	0.4	0.0617	0.0022	-0.06	602.75	21.91	36	8.4	99.8
1	15	Rim	2511.9	85.8	0.0768	0.0059	-0.21	2.55	0.09	1020	8.5	96.1
1	15	Core	2368.0	70.1	0.0517	0.0027	0.00	2.75	0.08	2226	8.6	99.3

Appendix F: Statistical Distance Matrices

60-63% SiO2 Subset of Samples

Distance Matrix (Euclidean Distance)

	Chao	Chanka	Chascon
Chao		1.290	4.000
Chanka	1.290		3.384
Chascon	4.000	3.384	

66-69% SiO2 Subset of Samples

Distance Matrix (Euclidean Distance)

	Chanka	Chao	Chao	Chao	Chao	Chao	Chao	Chascon	Chao	Chao	Chascon	Chillahuita	Chillahuita
Chanka		0.675	1.078	1.318	1.531	1.656	1.716	2.543	1.879	2.271	2.494	2.413	2.504
Chao	0.675		0.825	0.952	1.135	1.263	1.369	2.215	1.531	1.950	2.043	2.089	2.180
Chao	1.078	0.825		0.546	0.878	0.673	0.817	1.821	0.854	1.299	1.611	1.393	1.501
Chao	1.318	0.952	0.546		0.351	0.438	0.436	1.546	0.817	1.075	1.370	1.276	1.311
Chao	1.531	1.135	0.878	0.351		0.608	0.471	1.528	0.989	1.094	1.368	1.340	1.331
Chao	1.656	1.263	0.673	0.438	0.608		0.291	1.380	0.427	0.739	1.039	0.885	0.949
Chao	1.716	1.369	0.817	0.436	0.471	0.291		1.330	0.587	0.665	1.092	0.897	0.901
Chascon	2.543	2.215	1.821	1.546	1.528	1.380	1.330		1.332	1.135	1.213	1.347	1.208
Chao	1.879	1.531	0.854	0.817	0.989	0.427	0.587	1.332		0.572	0.907	0.586	0.730
Chao	2.271	1.950	1.299	1.075	1.094	0.739	0.665	1.135	0.572		0.832	0.353	0.265
Chascon	2.494	2.043	1.611	1.370	1.368	1.039	1.092	1.213	0.907	0.832		0.887	0.890
Chillahuita	2.413	2.089	1.393	1.276	1.340	0.885	0.897	1.347	0.586	0.353	0.887		0.283
Chillahuita	2.504	2.180	1.501	1.311	1.331	0.949	0.901	1.208	0.730	0.265	0.890	0.283	

69-72% SiO2 Subset of Samples

Distance Matrix (Euclidean Distance)

	Chao	Chascon	Chao	Chascon	Tocopuri	Tocopuri	Tocopuri	Chascon
Chao		0.709	1.512	1.686	2.752	3.012	3.262	3.476
Chascon	0.709		1.793	1.529	2.801	3.073	3.317	3.444
Chao	1.512	1.793		1.845	2.658	2.683	2.866	2.727
Chascon	1.686	1.529	1.845		1.432	1.667	1.887	2.085
Tocopuri	2.752	2.801	2.658	1.432		0.477	0.704	1.570
Tocopuri	3.012	3.073	2.683	1.667	0.477		0.277	1.171
Tocopuri	3.262	3.317	2.866	1.887	0.704	0.277		1.067
Chascon	3.476	3.444	2.727	2.085	1.570	1.171	1.067	